# UNIVERSITÀ DEGLI STUDI DI TRIESTE

## XXX CICLO DEL DOTTORATO DI RICERCA IN

### INGEGNERIA E ARCHITETTURA

**Ente Finanziatore:** ELETTRA SINCROTRONE TRIESTE S.C.P.A.

# PHASE-CONTRAST BREAST TOMOGRAPHY WITH SYNCHROTRON RADIATION: STUDY AND OPTIMIZATION OF EXPERIMENTAL AND RECONSTRUCTION PARAMETERS

Settore scientifico-disciplinare: **ING/INF 06**

DOTTORANDO / A
**SERENA PACILÈ**

COORDINATORE
**PROF. DIEGO MICHELI**

SUPERVISORE DI TESI
**PROF. AGOSTINO ACCARDO**

**ANNO ACCADEMICO 2016/2017**

*"Sono fra coloro che pensano che la scienza abbia una grande bellezza. Uno studioso nel suo laboratorio non è solo un tecnico, è anche un bambino messo di fronte a fenomeni naturali che lo impressionano come una fiaba. Non dobbiamo lasciar credere che ogni progresso scientifico si riduca a dei meccanismi, a delle macchine, degli ingranaggi, che pure hanno anch'essi una loro bellezza. Io non credo che nel nostro mondo lo spirito d'avventurarischi di scomparire. Se vedo attorno a me qualcosa di vitale, è proprio questo spirito d'avventura che mi sembra impossibile da sradicare, e che ha molto in comune con la curiosità."*

Marie Curie

# Acknowledgements

È doveroso ed è un piacere per me ringraziare tutti coloro che hanno contribuito in diversi modi al completamento di questo percorso, dal momento che senza il loro sostegno e incoraggiamento questo lavoro non sarebbe stato possibile.

Desidero innanzitutto esprimere la mia piena gratitudine alla Dr. Giuliana Tromba, questo lavoro è stato realizzato grazie ai suoi insegnamenti e alla passione per la ricerca che mi ha trasmesso lavorando insieme. La sua non è stata soltanto una guida professionale ma anche una presenza molto importante a livello personale.

Ringrazio il mio supervisore di tesi, il prof. Agostino Accardo per i suoi costanti consigli ed incoraggiamenti.

Ringrazio tutto lo staff di SYRMEP: il Dr. Nicola Sodini, il Dr. Franco Zanini, la Dr. Lucia Mancini e sopratutto il Dr. Diego Dreossi per i suoi preziosi insegnamenti durante i beamtime.

Vorrei inoltre ringraziare il Dr. Francesco De Carlo e il prof.Mario Cesarelli per aver accettato di essere revisori di questo lavoro di tesi.

I am also thankful to our Australian collaborators and in particular to Dr.Tim Gureyev for having shared his precious expertise, and Patrycja Baran for being a great teammate even with a 10 hours time-zone offset. The work in this thesis would not have been possible without their support.

I owe my gratitude to Dr. Christian Dullin, as well, for his continuous teachings

and suggestions and for his patience and carefulness in supervising all my works.

I would like to thank Dr. Alberto Bravin for letting me spend an interesting time at ESRF, and Dr. Daniel Hausermann for giving me the possibility to do an amazing experience at Australian Synchrotron.

Vorrei ringraziare, inoltre i colleghi, o meglio gli amici, che ho incontrato durante questo percorso e lo hanno arricchito con la loro presenza. Da un lato Luisa, Sandro, Gabriele e Fabio per le innumerevoli serate "insalata e BarH", dall'altro Milos e Gigi per gli innumerevoli Spritz.

Je ne peux que remercier aussi JB pour avoir été à mes côtés pendant les périodes de Grenoble et surtout de Melbourne, et les avoir rendus spéciales.

Grazie!

# Contents

# List of Figures

# List of Tables

# List of Abbreviations

**2D, 3D** . . . . Two- or three-dimensional, referring in this thesis to spatial dimensions in an image

**PT** . . . . . Phyllodes tumors

**AS** . . . . . Angiosarcoma

**LCIS** . . . . . Lobular carcinoma in situ

**DCIS** . . . . . Ductal carcinoma in situ

**IDC** . . . . . Invasive ductal carcinoma

**ILC** . . . . . Invasive lobular carcinoma

**MRI** . . . . . Magnetic resonance imaging

**DBT** . . . . . Digital breast tomosynthesis

**DBCT** . . . . . Dedicated breast computed tomography

**MBI** . . . . . Molecular breast imaging

**PEM** . . . . . Positron emission mammography

**EIT** . . . . . Electrical impedance imaging

**UST** . . . . . Ultrasound tomography

**PBI** . . . . . Propagation based imaging

**PB-CT** . . . . Propagation based phase-contrast computed tomography

**ABI** . . . . . Analyser-based imaging

**EI** . . . . . Edge illumination

**GI** . . . . . Grating x-ray interferometry

**SAXS** . . . . . Small-angle scattering

**USAXS** . . . . Ultra-small-angle scattering

**SR** . . . . . Synchrotron radiation

**LINAC** . . . . Linear accelerator

**BM** . . . . . Bending magnet

**ID** . . . . . Insertion device

**FBP** . . . . . Filtered back projection

**ART** . . . . . Algebraic reconstruction technique

**STP** . . . . . SYRMEP Tomo Project

**SIRT** . . . . . Simultaneous Iterative Reconstruction Technique

**SART** . . . . . Simultaneous Algebraic Reconstruction Technique

**CGLS** . . . . . Conjugate Gradient Least Squares

**EST** . . . . . Equally Sloped Tomography

**MR-FBP** . . . Minimum Residual FBP

**TV** . . . . . Total variation minimisation

**SNR** . . . . . Signal-to-noise ratio

**AGD** . . . . . Average Glandular Dose

**MSE** . . . . . Mean squared Error

**UQI** . . . . . Universal Quality Index

**NQM** . . . . . Noise Quality Measure

**SSIM** . . . . . Structural Similarity Index

**iFBP** . . . . . Iterative Filtered Back Projection

**MC** . . . . . Monte Carlo

**ROI** . . . . . Region of Interest

**PSF** . . . . . Point spread function

**MTF** . . . . . Modulation transfer function

**FoM** . . . . . Figure of Merit

# Introduzione in Italiano

Il cancro al seno è una delle tipologie di tumore pi diagnosticata tra le donne e rappresenta la seconda causa di morte per cancro. Di conseguenza, il cancro al seno e la sua diagnosi precoce sono diventati un problema cruciale per la salute pubblica. Per tale ragione, si è diffuso un crescente interesse verso lo sviluppo di nuovi mezzi e tecniche di imaging che possano supportare o sostituire la mammografia convenzionale (note per la sua limitata specificità), col fine ultimo di migliorare l'efficienza dei programmi di screening. In questo contesto, nell'ultimo decennio, a mostrare risultati promettenti nel perfezionamento della diagnosi del cancro al seno, sono state le tecniche a contrasto di fase, le quali sfruttano la rifrazione dei raggi x anziché il loro assorbimento. È stato dimostrato che le variazioni di fase del fascio di raggi x che passa attraverso i tessuti molli, possono essere due o tre ordini di grandezza più elevate rispetto alle variazioni di assorbimento, ottenendo dunque un pi elevato contrasto sulle immagini. Inoltre, le tecniche a contrasto di fase permetterebbero di ridurre la dose di radiazione rilasciata alla paziente durante l'esame. Esistono diversi approcci di metodi a contrasto di fase, tuttavia, nel presente lavoro di tesi, ci si soffermerà sulla cosidetta tecnica "propagation-based" (PB-CT), che è quella caratterizzata dalla più semplice implementazione, in quanto non necessita di elementi ottici addizionali. Fino ad oggi, la sua applicazione, dato l'alto livello richiesto di coerenza spaziale del fascio di raggi x, è limitata ai sincrotroni. Tuttavia, l'ottimizzazione presentata in questo lavoro, può essere estesa non solo alle altre tecniche a contrasto di fase ma anche ai setup con sorgenti compatte. Lo scopo di questo lavoro di tesi è quello di ottimizzare il protocollo sperimentale e l'analisi dei dati per l'imaging in-vivo del seno con tomografia a contrasto di fase. Verranno dunque descritti i risultati di molteplici studi di fattibilità condotti ad Elettra e all'Australian Synchrotron. Con diversi setup

sperimentali e a diverse scale di risoluzione, sono stati studiati vari campioni di tessuto mammario umano e un fantoccio test appositamente progettato e realizzato. Le immagini, poi sono state ricostruite seguendo diverse strategie di pre-processing, algoritmo di ricostruzione e post-processing. Una particolare attenzione è stata posta nei confronti del "phase retrieval", ovvero l'algoritmo che permette di sfruttare l'informazione proveniente dall'effetto di contrasto di fase, e del suo effetto sul valore diagnostico delle immagini ricostruite. Le immagini sono state, infine, valutate in maniera quantitativa utilizzando indici di qualità oggettivi e in maniera qualitativa sfruttando la valutazione soggettiva di radiologi esperti. Una volta stabilito il protocollo corretto, una seconda serie di campioni è stata acquisita seguendo la strategia scelta e con un sistema dedicato di breast-CT, per mettere in risalto le potenzialità della tecnica a contrasto di fase rispetto alla tomografia in assorbimento. Infine un è stato studiato e proposto un ulteriore potenziale utilizzo della PB-CT, ovvero l'istologia virtuale. Questa volta i campioni sono stati acquisiti ad una più alta risoluzione e sono stati confrontati con immagini istologiche.

In sintesi, il presente lavoro di tesi è suddiviso come segue:

*Capitolo 1.* Breve descrizione dell'anatomia del seno, delle tipologie di cancro e delle tecniche convenzionali e innovative attualmente impiegate per la diagnosi del cancro al seno.

*Capitolo 2.* Teoria dell'imaging a contrasto di fase e descrizione delle tecniche più utilizzate con particolare attenzione verso la cosiddetta "propagation-based".

*Capitolo 3.* Principio di funzionamento di un sincrotrone e descrizione dettagliata delle linee di luce SYRMEP e IMBL.

*Capitolo 4.* Descrizione dei metodi di elaborazione dell'immagine: dalla trasformata di Radon alla renderizzazione tridimensionale.

*Capitolo 5.* Risultati sperimentali ottenuti applicando la tecnica a contrasto di fase alla diagnosi del cancro al seno: studio riguardante l'ottimizzazione dei parametri sperimentali e di ricostruzione.

*Capitolo 6.* Risultati sperimentali ottenuti applicando la tecnica a contrasto di fase alla diagnosi del cancro al seno: confronto con i sistemi dedicati di tomografia al

seno basati sull'assorbimento.

*Capitolo 7.* Risultati sperimentali ottenuti applicando la tecnica a contrasto di fase alla diagnosi del cancro al seno: studio di fattibilità riguardante la potenziale utilità dell'istologia virtuale.

# Introduction

Breast cancer is one of the most frequently diagnosed cancer types among women and it is the second leading cause of cancer related death (Siegel et al. (2016)). Therefore, breast cancer has become a critical public health concern and its detection at an early stage is crucial (Shah et al. (2016)). For this reason, to improve the effectiveness of breast cancer screening, there is an increasing interest in the development of novel tools and imaging techniques that may supplement or replace mammography which is known for its limited specificity (Sprague et al. (2017)). In this context, in recent years, the development of x-ray phase-contrast imaging techniques, which exploit x-rays refraction in the body, have shown promising results for refining breast cancer diagnosis (Coan et al. (2013)). It has been demonstrated that for x-rays passing through soft tissues, phase variations can be two to three orders of magnitude larger than absorption, and therefore an increased image contrast can be achieved with phase sensitive techniques (Beltran et al. (2011)). In addition, phase-contrast techniques hold the potential to reduce the radiation dose delivered to the patient (Diemoz et al. (2012); Keyriläinen et al. (2011); Pagot et al. (2005); Sztrókay et al. (2012)). Several approaches for phase-contrast CT techniques have been reported (Coan et al. (2013); Gureyev et al. (2014); Keyriläinen et al. (2010); Olivo et al. (2013)). In this work, the focus is on propagation-based phase-contrast CT (PB-CT) as it does not re quire additional optical elements which makes it very dose efficient and easy to implement (Gureyev et al. (2013)). Up to now the required level of spatial coherence of the incident x-ray beam used in PB-CT has practically limited its application to synchrotron facilities, however, the optimisation scheme for PB-CT breast imaging presented here can be generalised to novel generator-based phase-contrast imaging setups (including analyser-based imaging, edge-illumination, and grating-based imaging) or compact

sources. The aim of this thesis work was to optimise the experimental protocol and data analysis for in-vivo three-dimensional phase-contrast breast imaging. Results are presented of feasibility studies carried out at Elettra and Australian Synchrotron using the propagation-based phase-contrast tomography method. Several breast tissue samples, of a size corresponding to a full human breast, and a custom designed plastic phantom have been studied at different resolution scales and experimental conditions. Several computed tomography reconstruction algorithms with different pre-processing and post-processing steps have been considered. Special attention was paid to the effect of phase retrieval on the diagnostic value of the reconstructed images. The images were quantitatively evaluated using objective quality indices and subjective assessments performed by experienced radiologists and pathologists. Once the protocol has been established, a second series of samples has been acquired with both synchrotron (following the chosen strategy) and a dedicated breast-CT system, in order to assess the advantages of phase-contrast technique with respect to absorption based tomographic technique. Finally, an innovative use of 3D phase-contrast micro-computed tomography (micro-CT) has been studied and presented, i.e. the virtual histology. This time the specimens have been acquired at higher spatial resolution and compared with the conventional histological microscopy images.

In summary, the Thesis is organised as follows:

*Chapter 1.* Brief description of the breast anatomy and breast cancer types and of the conventional and innovative techniques used to detect breast cancer.

*Chapter 2.* Theory of the phase-contrast imaging and description of the most used phase sensitive technique with particular attention to the propagation-based.

*Chapter 3.* Working principle of a synchrotron facility and detailed description of the set-up at SYRMEP and IMBL beamlines.

*Chapter 4.* Description of the image processing methods: from the Radon transform to the 3D rendering.

*Chapter 5.* Experimental results obtained by applying the propagation-based imaging technique to the breast cancer detection - study on the optimisation of

experimental and reconstruction parameters.

*Chapter 6.* Experimental results obtained by applying the propagation-based imaging technique to the breast cancer detection - comparison with dedicated absorption-based breast-CT system.

*Chapter 7.* Experimental results obtained by applying the propagation-based imaging technique to the breast cancer detection - feasibility study on the potential usefulness of virtual histology.

# References

Beltran, M.A., Paganin, D.M., Siu, K.K.W., Fouras, A., Hooper, S.B., Reser, D.H., Kitchen, M.J., 2011. Interface-specific x-ray phase retrieval tomography of complex biological organs. Phys. Med. Biol. 56, 7353. URL: http://stacks.iop.org/0031-9155/56/i=23/a=002, doi:10.1088/0031-9155/56/23/002.

Coan, P., Bravin, A., Tromba, G., 2013. Phase-contrast x-ray imaging of the breast: recent developments towards clinics. J. Phys. D: Appl. Phys. 46, 494007. URL: http://stacks.iop.org/0022-3727/46/i=49/a=494007, doi:10.1088/0022-3727/46/49/494007.

Diemoz, P.C., Bravin, A., Coan, P., 2012. Theoretical comparison of three X-ray phase-contrast imaging techniques: propagation-based imaging, analyzer-based imaging and grating interferometry. Opt Express 20, 2789–2805.

Gureyev, T., Mohammadi, S., Nesterets, Y., Dullin, C., Tromba, G., 2013. Accuracy and precision of reconstruction of complex refractive index in near-field single-distance propagation-based phase-contrast tomography. Journal of Applied Physics 114. doi:10.1063/1.4824491.

Gureyev, T.E., Nesterets, Y.I., de Hoog, F., Schmalz, G., Mayo, S.C., Mohammadi, S., Tromba, G., 2014. Duality between noise and spatial resolution in linear systems. Opt Express 22, 9087–9094.

Keyriläinen, J., Bravin, A., Fernández, M., Tenhunen, M., Virkkunen, P., Suortti, P., 2010. Phase-contrast X-ray imaging of breast. Acta Radiol 51, 866–884. doi:10.3109/02841851.2010.504742.

Keyriläinen, J., Fernández, M., Bravin, A., Karjalainen-Lindsberg, M.L., Leidenius, M., von Smitten, K., Tenhunen, M., Kangasmäki, A., Sipilä, P., Nemoz, C., Virkkunen, P., Suortti, P., 2011. Comparison of in vitro breast cancer visibility in analyser-based computed tomography with histopathology, mammography,

computed tomography and magnetic resonance imaging. J Synchrotron Radiat 18, 689–696. doi:10.1107/S090904951102810X.

Olivo, A., Gkoumas, S., Endrizzi, M., Hagen, C.K., Szafraniec, M.B., Diemoz, P.C., Munro, P.R.T., Ignatyev, K., Johnson, B., Horrocks, J.A., Vinnicombe, S.J., Jones, J.L., Speller, R.D., 2013. Low-dose phase contrast mammography with conventional x-ray sources. Med Phys 40, 090701. doi:10.1118/1.4817480.

Pagot, E., Fiedler, S., Cloetens, P., Bravin, A., Coan, P., Fezzaa, K., José Baruchel, Härtwig, J., 2005. Quantitative comparison between two phase contrast techniques: diffraction enhanced imaging and phase propagation imaging. Phys. Med. Biol. 50, 709. URL: http://stacks.iop.org/0031-9155/50/i=4/a=010, doi:10.1088/0031-9155/50/4/010.

Shah, C., Arthur, D.W., Wazer, D., Khan, A., Ridner, S., Vicini, F., 2016. The impact of early detection and intervention of breast cancer-related lymphedema: a systematic review. Cancer Med 5, 1154–1162. doi:10.1002/cam4.691.

Siegel, R.L., Miller, K.D., Jemal, A., 2016. Cancer statistics, 2016. CA Cancer J Clin 66, 7–30. doi:10.3322/caac.21332.

Sprague, B.L., Arao, R.F., Miglioretti, D.L., Henderson, L.M., Buist, D.S.M., Onega, T., Rauscher, G.H., Lee, J.M., Tosteson, A.N.A., Kerlikowske, K., Lehman, C.D., 2017. National Performance Benchmarks for Modern Diagnostic Digital Mammography: Update from the Breast Cancer Surveillance Consortium. Radiology 283, 59–69. URL: http://pubs.rsna.org/doi/10.1148/radiol.2017161519, doi:10.1148/radiol.2017161519.

Sztrókay, A., Diemoz, P.C., Schlossbauer, T., Brun, E., Bamberg, F., Mayr, D., Reiser, M.F., Bravin, A., Coan, P., 2012. High-resolution breast tomography at high energy: a feasibility study of phase contrast imaging on a whole breast. Phys Med Biol 57, 2931–2942. doi:10.1088/0031-9155/57/10/2931.

# 1

# Breast anatomy and Imaging techniques

## Contents

## 1.1 *Introduction*

Breast cancer is the most common malignancy among women in developed countries, next to lung and bronchus cancer (Siegel et al. (2016)). It is the most frequent cancer among women, with an estimated 1.67 million new cases diagnosed in 2012, constantly increasing in numbers around the world (Ferlay et al. (2015)). According to statistics, the 5-year survival rates in women diagnosed of breast cancers has considerably improved in the last years, with 75% survival rate in 1975, 79% survival rate in 1985 and 89% survival rate in 2003 registered in USA (Jemal et al. (2004)). Likely explanations for these reductions are early detection by mammography screening and advances in treatment. There is in fact evidence, that the early diagnosis of breast cancer can improve the prognosis. It is estimated that an early detected tumour (less than 10 mm in size), which has not invaded the mammary glands, can be successfully treated in about 90% of cases, whereas this value drops to about 55% if glandular invasion has occurred and to 18% in the case of metastases (Sant et al. (2003)). Mammography has been the frontline screening tool for breast cancer for decades with over 1.3 million women being examined each year, yet high rates of error have persisted despite the most recent technological improvements. Radiologists miss between 30% and 40% of early breast cancers and only 10% of women recalled for further examinations have cancer. (Poplack et al. (2005); Rawashdeh et al. (2013)). Many countries have implemented regular breast screening of women after the age of 40 or 50 with 2D x-ray mammography being the main screening and diagnostic technique. Despite important recent advances in mammographic examination, such as the introduction of digital breast tomosynthesis, limitations remain around diagnostic efficacy, radiation dose and patient discomfort/pain. The limitations of mammography and digital breast tomosynthesis can be summarised as follows:

- Diagnostic efficacy: Sensitivity of 2D digital mammography varies from approximately 50% to 80%. About 20% of breast cancers are not detectable at all. Specificity also varies due to overlap between the appearances of benign

and malignant breast tissue characteristics, requiring biopsy to distinguish between the two.

- Radiation dose: A significant amount of radiation is delivered each time a woman undergoes mammography. Also, a significant variation in the dose delivered can exist due to equipment used and location of examination. The breast is the most radiosensitive organ in the body and since the risk of cancer induction from x-ray exposures is directly related to the level of radiation dose, novel methods that minimise radiation exposures need to be sought.

- Patient discomfort/pain: Forcible compression of the breast is needed to create a more uniform breast thickness in 2D mammography and tomosynthesis, however this compression can result in a substantial amount of pain or discomfort for a large majority of women.

In the light of these considerations, there is a strong need for improvements of currently available methods for breast imaging.

## 1.2 Breast anatomy and types of breast cancer

The breast is composed of mammary glands surrounded by a connective tissue stroma. The mammary glands are modified sweat glands, they consist of a series of ducts and secretory lobules (15-20), each lobule consists of many alveoli drained by a single lactiferous duct. These ducts converge at the nipple like spokes of a wheel. The connective tissue stroma is a supporting structure which surrounds the mammary glands. It has a fibrous and a fatty component. The fibrous stroma condenses to form suspensory ligaments (of Cooper), these ligaments have two main functions: attach and secure the breast to the dermis and underlying pectoral fascia and separate the secretory lobules of the breast. The base of the breast lies on the pectoral fascia - a flat sheet of connective tissue associated with the pectoralis major muscle. It acts as an attachment point for the suspensory ligaments. The layer of loose connective tissue between the breast and pectoral fascia is known as retro-mammary space. Arterial supply to the medial aspect of the breast is via the internal thoracic artery, a branch of the subclavian artery. The lateral part of the breast receives blood from four vessels:

- Lateral thoracic and thoracoacromial branches - originate from the axillary artery.
- Lateral mammary branches - originate from the posterior intercostal arteries (derived from the aorta). They supply the lateral aspect of the breast in the 2nd 3rd and 4th intercostal spaces.
- Mammary branch - originates from the anterior intercostal artery.

The veins of the breast correspond with the arteries, draining into the axillary and internal thoracic veins. The lymphatic drainage of the breast is of great clinical importance due to its role in the metastasis of breast cancer cells. There are three groups of lymph nodes that receive lymph from breast tissue: the axillary nodes (75%), parasternal nodes (20%) and posterior intercostal nodes (5%). The skin of the breast also receives lymphatic drainage: skin drains to the axillary,

inferior deep cervical and infraclavicular nodes; nipple and areola drains to the subareolar lymphatic plexus. The breast is innervated by the anterior and lateral cutaneous branches of the 4th to 6th intercostal nerves. These nerves contain both sensory and autonomic nerve fibres (the autonomic fibres regulate smooth muscle and blood vessel tone). It should be noted that the nerves do not control the secretion of milk. This is regulated by the hormone prolactin, which is secreted from the anterior pituitary gland.

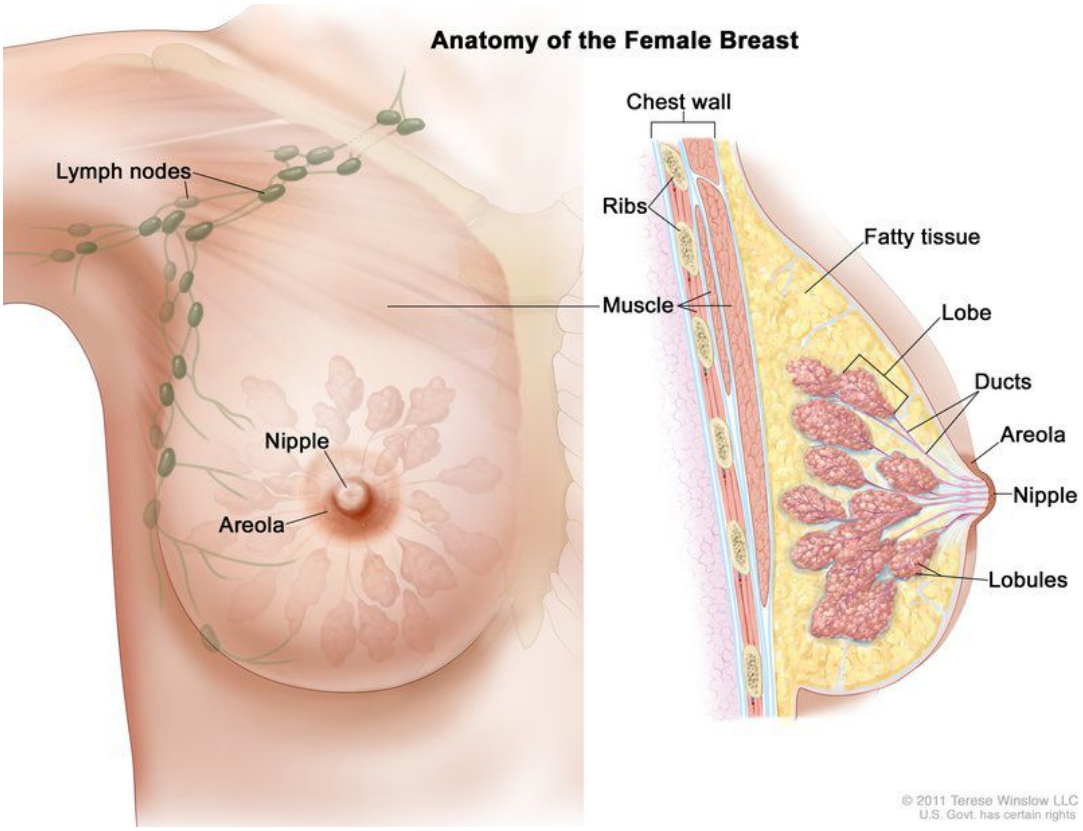


**Figure 1.1:** Drawing of female breast anatomy showing the lymph nodes, nipple, areola, chest wall, ribs, muscle, fatty tissue, lobe, ducts, and lobules.

Breast cancers can be divided into two main overarching groups: the carcinomas and the sarcomas. Carcinomas are cancers that arise from the epithelial component of the breast. The epithelial component consists of the cells that line the lobules and terminal ducts; under normal conditions, these epithelial cells are responsible for making milk. Carcinomas comprise the clear majority of all breast cancers, and will be further discussed below. Sarcomas are rare cancers that arise from the

stromal (connective tissue) components of the breast. These stromal component cells include myofibroblasts and blood vessel cells, and cancers arising from these "supportive" cells include phyllodes tumors (PT) and angiosarcoma (AS). Sarcomas account for less than 1% of primary breast cancers. Within the large group of carcinomas, there are many different types of breast cancer. The first major division is between in situ and invasive carcinoma. In situ carcinoma is "pre-invasive" carcinoma that has not yet invaded the breast tissue. These in situ cancer cells grow inside of the pre-exisiting normal lobules or ducts (LCIS and DCIS). In situ carcinoma has significant potential to become invasive cancer, and that is why it must be adequately treated to prevent the patient from developing invasive cancer. Invasive cancers have cancer cells that infiltrate outside of the normal breast lobules and ducts to grow into the breast connective tissue. Invasive carcinomas have the potential to spread to other sites of the body, such as lymph nodes or other organs, in the form of metastases. Approximately 80% of breast carcinomas are invasive ductal carcinoma (IDC), followed by invasive lobular carcinomas (ILC) which account for approximately 10-15% of cases. Invasive ductal carcinomas and invasive lobular carcinomas have distinct pathologic features. Specifically, lobular carcinomas grow as single cells arranged individually, in single file, or in sheets, and they have different molecular and genetic aberrations that distinguish them from ductal carcinomas. Ductal and lobular carcinomas may have different prognoses and treatment options, depending upon all the other features of the particular cancer. The remaining cases of invasive carcinoma are comprised of other special types of breast cancer that are characterized by unique pathologic findings. These special types include colloid (mucinous), medullary, micropapillary, papillary, and tubular. It is important to distinguish between these various subtypes, because they can have different prognoses and treatment implications.

## 1.3 Breast imaging methods

The effectiveness of cancer treatment in breast are strongly dependent on the stage at which the pathology is detected. An early detection could significantly lower the

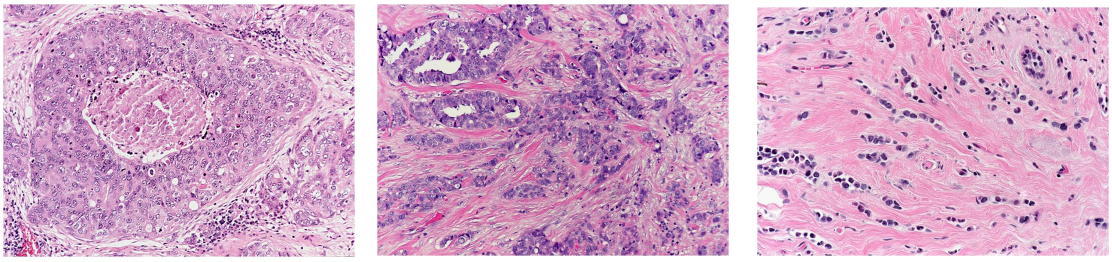

**Figure 1.2:** Histologic examples of in situ and invasive carcinomas of the breast. On the left side, a high grade ductal carcinoma in situ, in the middle an invasive ductal carcinoma and on the right an invasive lobular carcinoma.

morbidity and the mortality rate, accordingly, different complementary imaging techniques are nowadays available and used in the clinical practice.

### 1.3.1 Conventional imaging techniques and related limitations

*Mammography* - Among all the currently available imaging techniques, conventional mammography (classical 2D x-ray absorption based imaging), is still the gold standard employed for breast cancer screening. So far, it is also the method that achieves the highest spatial resolution, (about 20 (lp/mm)) (**?**). However, as the different tissues within the breast have only minor differences in x-ray absorption and moreover their 3D distribution is projected onto a planar image causing overlapping of structures, the specificity and sensitivity of mammography is rather poor. In addition, since the differences in x-ray absorption become smaller with increasing x-ray energy, mammography exams are performed at relatively low energies thus increasing the radiation dose. At the same time, because of the high radio-sensitivity of the breast, the dose delivered to the patient during a mammography examination must be limited to minimise its radio-toxicity. This of course, leads the achievable absorption contrast to be lower, and affects the visualisation of malignancies in the mammograms. Besides, the image contrast is further decreased by the scattered radiation, which fogs to a certain extent the image signal despite the anti-scatter grids that are typically employed to reduce this effect.

*Ultrasound* - Breast ultrasound, as opposed to x-ray mammography, has not been considered for breast cancer screening. It is more used as a complementary analysis tool because of the significant overlap in characteristics of benign tissues and malignant lesions. Ultrasound is useful for looking at some breast changes, such as those that can be felt but not seen on a mammogram or changes in women with dense breast tissue. It also can be used to look at a change that may have been seen on a mammogram or to tell the difference between fluid-filled cysts and solid masses. This kind of examination can be used to help guide a biopsy needle into an area of change so cells can be taken out and tested for cancer. It can also be used to look for and guide a biopsy needle into swollen lymph nodes under the arm. Moreover, its main disadvantage resides in its poor ability to detect micro-calcifications, which are frequently linked to breast cancer.

*Magnetic resonance imaging (MRI)* - A breast MRI examination is mainly used for women who have already been diagnosed with breast cancer. It is applied to measure the size of the cancer, look for other tumours in the breast, and to check for tumours in the opposite breast. For certain women at high risk for breast cancer, a screening MRI is recommended along with a yearly mammogram. MRI is not recommended as a screening tool by itself because it can miss some cancers that a mammogram would find. Although MRI can find some cancers not seen on a mammogram, it?s also more likely to find something that turns out not to be cancer (high rates of false positive cases). False-positive findings have to be checked out to know that cancer isn?t present. This means more tests and/or biopsies. Therefore, MRI is not recommended as a screening test for women at average risk of breast cancer, because it would mean unneeded biopsies and other tests for many of these women. High costs, bulkiness of the equipment and the large acquisition times (between 45 and 60 minutes) are also other disadvantages related to MRI. Furthermore, breast MRI is not sensitive to micro-calcifications, which can be an early indication of breast disease and represent a frequent finding on mammography.

*Digital breast tomosynthesis (DBT)* - In this technique, multiple projection images are reconstructed allowing visual review of thin breast sections offering the potential to unmask cancers obscured by normal tissue located above and below the lesion. DBT involves the acquisition of multiple projection exposures by a digital detector from a mammographic x-ray source which moves over a limited arc angle. These projection image data sets are reconstructed using specific algorithms. The clinical reader is presented with a series of images (slices) through the entire breast; because each reconstructed slice may be as thin as 0.5 mm, masses and mass margins that may otherwise be superimposed with out of plane structures should be more visible in the reconstructed slice. This allows the visualisation (detection) and better characterisation of the lesions. However, it is not possible to focus on areas between two adjacent slices and the presence of micro-calcifications can, in some case, cause artefacts on images. Additionally the small difference in x-ray attenuation, in particular between the glandular and tumour tissues, still constitutes a problem for this method.

*Dedicated breast CT (DBCT)* - This method represents a new technology which may allow true three-dimensional imaging of the breast using the same fundamental x-ray contrast mechanism with which breast imagers are already familiar. The breast to be imaged is positioned in a hole in the centre of the breast CT table, as then women lies prone with her breast in the pendant position. This allows the CT scanner hardware to rotate in the horizontal plane and acquire the projection data necessary for cone beam CT reconstruction. As for the tomosynthesis, even if the overlapping tissue problem is solved, the small differences in x-ray absorption coefficient between soft-tissue are still representing a problem in this method. This, together with the poor visualisation of micro-calcifications on un-enhanced DBCT and the high level of radiation dose delivered to the patient, poses a significant barrier to the use of this modality for breast cancer screening since many cases of DCIS might not be visualised. For this reason, the use of contrast enhancement is now being diffused (Uhlig et al. (2017)).

### 1.3.2 Experimental breast imaging techniques

To overcome the limitation of the conventional images technique, some newer tests are now being studied for breast imaging. These new methods are in the earliest stages of research. It will probably take time to see if any of them are as good as or better than those we use today.

*Optical imaging* - This method uses visible light passing into the breast and then measures the light that returns or passes through the tissue. The technique does not use ionising radiation and does not require breast compression. Studies going on now are looking at combining optical imaging with other tests like MRI or 3D mammography to help diagnose breast cancer.

*Molecular breast imaging (MBI)* - This test is being studied as a way to follow up breast problems (such as a lump or an abnormal mammogram). It?s also being studied as a test that can be used along with mammograms for women with dense breasts.

*Positron Emission Mammography (PEM)* - PEM technique uses sugar attached to a radioactive particle to detect cancer cells. The PEM scanner is approved by the Food and Drug Administration (FDA). Working much like a PET scan, a PEM scan may be better able to detect small clusters of cancer cells within the breast. Right now, it?s being studied in women with breast cancer or other breast problems to see if it can show which lumps are cancer.

*Electrical impedance imaging (EIT)* - This kind of examination scans the breast for electrical conductivity. It?s based on the idea that breast cancer cells conduct electricity differently from normal cells. The test passes a very small electrical current through the breast and then detects it on the skin of the breast. This is done using small electrodes that are taped to the skin. EIT does not use radiation or compress the breasts. This test is approved by the Food and Drug Administration

(FDA) to help classify tumours found on mammograms. However, today there hasn't had enough clinical testing to use it in breast cancer screening.

*Whole breast ultrasound tomography (UST)* - In contrast to conventional ultrasound, an ultrasound tomography system surrounds the entire breast with a ring of sensors, allowing for detection of the ultrasound signal scatter field from all angles of transmission. A variety of processing techniques are then used to combine and fuse the images into one image. For cancer imaging, pixels are examined in the three sets of ultrasound tomography images (reflection, sound speed, and attenuation). Thresholds are then assigned based on prior evidence showing that cancer tends to be highly stiff and dense; therefore, cancer should have high sound speed and high attenuation. Only pixels that exceed both thresholds simultaneously are displayed, allowing for the isolation of regions that are biomechanically different. Though its resolution isn't quite as good as MRI, the ultrasound tomography system overall offers similar sensitivity for different tissue types.

Another important class of experimental techniques, which have been investigated in recent years, is represented by the so-called phase-contrast imaging methods. These techniques hold the potential to give a significant improvement with respect to conventional absorption imaging and to overcome the limitation of the intrinsic low contrast of soft tissue in conventional radiology. It has been proved on both in-vitro and clinical studies (that will be better described later on) that phase-contrast mammography could provide greatly increased contrast for soft tissues and at lower radiation doses. Based on this results, it is reasonable to think that the application of phase-contrast principle on computed tomography could have an important role in the diagnosis process of breast cancer, overcoming any gains seen with recent technologies such as full field digital mammography or digital breast tomosynthesis (DBT). In the next chapter, an overview on the physical principles of phase-contrast will be given and the most used and promising phase-contrast techniques will be described.

# References

Ferlay, J., Soerjomataram, I., Dikshit, R., Eser, S., Mathers, C., Rebelo, M., Parkin, D.M., Forman, D., Bray, F., 2015. Cancer incidence and mortality worldwide: sources, methods and major patterns in GLOBOCAN 2012. Int. J. Cancer 136, E359–386. doi:10.1002/ijc.29210.

Jemal, A., Clegg, L.X., Ward, E., Ries, L.A.G., Wu, X., Jamison, P.M., Wingo, P.A., Howe, H.L., Anderson, R.N., Edwards, B.K., 2004. Annual report to the nation on the status of cancer, 1975-2001, with a special feature regarding survival. Cancer 101, 3–27. doi:10.1002/cncr.20288.

Poplack, S.P., Carney, P.A., Weiss, J.E., Titus-Ernstoff, L., Goodrich, M.E., Tosteson, A.N.A., 2005. Screening mammography: costs and use of screening-related services. Radiology 234, 79–85. doi:10.1148/radiol.2341040125.

Rawashdeh, M.A., Lee, W.B., Bourne, R.M., Ryan, E.A., Pietrzyk, M.W., Reed, W.M., Heard, R.C., Black, D.A., Brennan, P.C., 2013. Markers of good performance in mammography depend on number of annual readings. Radiology 269, 61–67. doi:10.1148/radiol.13122581.

Sant, M., Allemani, C., Capocaccia, R., Hakulinen, T., Aareleid, T., Coebergh, J.W., Coleman, M.P., Grosclaude, P., Martinez, C., Bell, J., Youngson, J., Berrino, F., EUROCARE Working Group, 2003. Stage at diagnosis is a key explanation of differences in breast cancer survival across Europe. Int. J. Cancer 106, 416–422. doi:10.1002/ijc.11226.

Siegel, R.L., Miller, K.D., Jemal, A., 2016. Cancer statistics, 2016. CA Cancer J Clin 66, 7–30. doi:10.3322/caac.21332.

Uhlig, J., Fischer, U., von Fintel, E., Stahnke, V., Perske, C., Lotz, J., Wienbeck, S., 2017. Contrast Enhancement on Cone-Beam Breast-CT for Discrimination of Breast Cancer Immunohistochemical Subtypes. Transl Oncol 10, 904–910. URL:

https://www.ncbi.nlm.nih.gov/pmc/articles/PMC5614638/, doi:10.1016/j.tranon.2017.08.010.

# 2
# Phase-Contrast Imaging

## Contents

## 2.1 *Introduction*

In conventional x-ray absorption based imaging techniques, the contrast between different materials is generated by the differences in density, thickness of the sample and x-ray absorption coefficient. In the energy range of hard x-rays, however, these latter differences can be very tiny (in the order of 0.1 - 0.3 $cm^{-1}$ for energies between 10 and 60 $keV$) when dealing with elements with low atomic number $Z$, as biological soft tissues. In medical imaging field, these conditions could lead to a wrong or incomplete characterization of the features defining the pathologic state. To overcome these limitations, in the last 20 years, phase-contrast imaging techniques have been extensively studied and applied to different medical and biological purposes. Their application to the diagnostic x-rays range became possible after the advent of the third-generation of synchrotrons facilities. The fundamental difference between these methods and the "conventional" ones, is that these techniques can exploit the refractions of x-rays rather than their absorption as source of contrast. As it will be described in this chapter, the interaction between x-ray and matter can be described in terms of the refraction index, whose real part $\delta$ , and imaginary part, $\beta$, are related to the electromagnetic phase shifts and to the x-ray attenuation in the object, respectively. For hard x-rays, $\delta$ could be orders of magnitude higher than the absorption component, allowing to increase the contrast between different soft tissues and at the same time reduce the radiation dose. Three main approaches to x-ray phase-contrast imaging currently attract the most attention, these are: propagation-based, analyser-based and grating-based imaging (Bravin et al. (2013), Wilkins et al. (2014),Auweter et al. (2014)). Recent quantitative studies (Diemoz et al. (2012)) have shown that all these methods can deliver comparable outcomes depending on the specific parameters of the experiment. However, the propagation-based (PB) phase-contrast (PB-CT) (Wilkins et al. (1996), Wilkins et al. (2014)) is the simplest in its experimental implementation (as it does not involve any optical elements), as well as in its theoretical underpinnings and it is the one used for the experimental work of this thesis, for this reason, it will

be more extensively described. The needed experimental requirements in terms of spatial and temporal coherence of the beam will also be discussed.

## 2.2 The complex refractive index

X-ray propagation through matter is usually described by mean of the complex refractive index, expressed as:

$$n = 1 - \delta + i\beta \tag{2.1}$$

$\delta$ represents the refractive index decrement, which is related to the phase shifts of the electromagnetic wave in the matter and, therefore, its deviation from the incident direction due to the scattering with electrons of the medium (Azároff (1968)). $\beta$ is the absorption term which is linked to the absorption of x-rays into the matter, mainly due to the photoelectric effect at low x-ray energies and Compton scattering in the other cases. The free-electrons model can properly describe the polarisation of the medium immersed in an electromagnetic field, for hard x-ray and far from absorption edges. In this model the electric susceptibility $\chi$ is proportional to the electron density $\rho_E$. How the $\delta$ and $\beta$ terms are related to the real and imaginary part of the susceptibility $\chi$, is described as follows (Zachariasen (1945)):

$$\delta = -\frac{1}{2}\chi_{0r} \tag{2.2}$$

$$\beta = \frac{1}{2}\chi_{0i} \tag{2.3}$$

this relation could be written also as (Jackson (1975)):

$$\delta = \frac{r_e \lambda^2 \rho_E}{2\pi} \tag{2.4}$$

$$\beta = \frac{r_e \lambda^3 \rho_E}{4\pi^2 c} \sum_j \frac{f_j \gamma_j}{Z} \tag{2.5}$$

where $r_e$ is the electron radius, $\lambda$ the x-rays wavelength, $f_j$ is the number of electrons per atom with damping constant $\gamma_j$, and $Z$ is the atomic number that gives the total number of electrons per atom; the sum is over all the electrons of the atom. The terms $\rho_E$ and $\rho$ are linked by the relationship $\rho_E = \frac{Z}{V} = \frac{Z\rho N_A}{A}$ where $V$ is the volume of reference, $N_A$ is the Avogadro number and $A$ is the atomic weight. The decrement of the refractive index can also be expressed as:

$$\delta = \frac{r_e \lambda^2}{2\pi V} \sum_j (Z + f_j^{'}) \tag{2.6}$$

where $f_j^{'}$ is the real part of the wavelength-dependent dispersion correction of the atomic scattering factor. The absorption term $\beta$ can be written, in the same way, as:

$$\beta = \frac{r_e \lambda^2}{2\pi V} \sum_j f_j^{''} \tag{2.7}$$

For an energy range, far from the absorption edges, $f_j^{'}$ tends to zero, while $f_j^{''}$ that is dominated by the absorption process, behaves with the energy as $E^{-m}$ with $m \in [3, 4]$. The absorption index $\beta$ is linked to the linear absorption coefficient $\mu$, by means of the following relation (Raven et al. (1996)):

$$\mu = \frac{2\pi\beta}{\delta} \tag{2.8}$$

Because of the local changes in the medium, the quantities $\beta$ and $\delta$, are functions of the spatial coordinates $(x, y, z)$. In a pure crystalline medium, the scattering properties of the incident radiation are usually described through the structure factor. If the Bragg reflection condition is not satisfied, the wave propagation cannot be influenced by the regular crystalline structure. In this latter case, the refractive index can be expressed as follows:

$$n = 1 - \frac{r_e \lambda^2}{2\pi} \frac{F_0}{V} \tag{2.9}$$

When $\beta$ and $\delta$ are very small, $n$ deviates slightly from 1. The quantity $\delta$ can be three order of magnitude much bigger than $\beta$ in the common diagnostic range, as reported in the following figure:

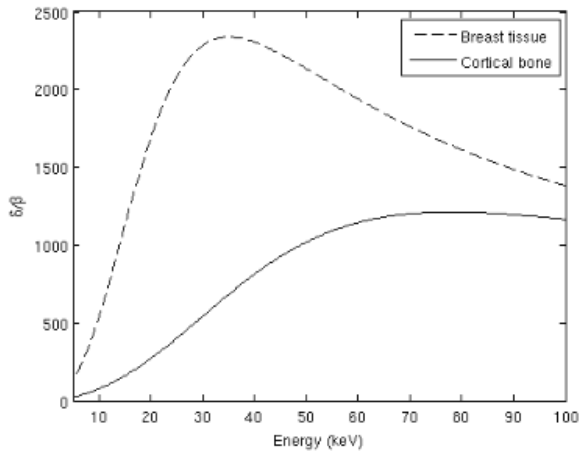


**Figure 2.1:** $\delta/\beta$ ratio for breast tissue and cortical bone. Values have been computed using the EPDL97 database (Cullen et al. (1997)). The compositions have been taken from taken from NIST.

The main advantage of phase-contrast imaging with respect to absorption based imaging techniques, comes from this big difference between$\beta$ and $\delta$. The term $\delta$ is related to the phase of the x-ray incident beam by the relation $\varphi = -2\pi\delta t/\lambda$ , where $t$ is the thickness of the material traversed by the beam, for this reason the energy dependence of the phase and of the linear attenuation coefficient can be expressed as $\varphi \sim E^{-1}$ and $\mu \sim E^{-3}$. It can be now considered an object described by $n(x, y, z)$, irradiated by a monochromatic beam of a certain wavelength $\lambda$, propagating along the $z$ axis. The wave passing through the object can be defined as:

$$\Psi_{obj}(x, y) = T(x, y)\Psi_{in}(x, y) \tag{2.10}$$

where $\Psi_{in}(x, y)$ is the incident wave on the object and $\Psi_{obj}(x, y)$ is the wave that

exit the sample surface. $T(x, y)$ is the complex transmission function that describe the interaction between the wave and the object, and it can be expressed as:

$$T(x, y) = A(x, y)e^{i\phi(x,y)} \tag{2.11}$$

The amplitude modulation is given by the projection of $\beta$ of refractive index distribution along the x-ray direction $z$.

$$A(x, y) = e^{-B(x,y)} \tag{2.12}$$

with

$$B(x, y) = \frac{2\pi}{\lambda} \int \beta(x, y, z)\mathrm{d}z \tag{2.13}$$

The phase modulation is provided by the projection along $z$ of $\delta$:

$$\phi(x, y) = -\frac{2\pi}{\lambda} \int \mathrm{d}z[1 - \delta(x, y, z)] = \phi_0 - \frac{2\pi}{\lambda} \int \mathrm{d}z\delta(x, y, z) \tag{2.14}$$

As a consequence of the distortion of the wavefront due to the phase shift caused by the object, the x-ray beam passing through the sample is locally refracted by an angle $\Delta\alpha$ defined as (Born et al. (1999)):

$$\Delta\alpha(x, y; \lambda) \simeq -\frac{2\pi}{\lambda} \overrightarrow{\nabla}_{x,y}\phi(x, y; \lambda) \tag{2.15}$$

## 2.3 Spatial and temporal coherence

Coherence is a fundamental characteristic needed for any phase contrast imaging system as it can describe the ability of the system to produce observable effects of interference and diffraction. It can be defined a *temporal (or longitudinal) coherence*, concerning the energy spectrum of the x-ray beam (the narrower is the spectral bandwidth, the higher is the coherence) and a *spatial (or lateral) coherence* regarding the source size and the geometry of the system (the smaller is the source size and the larger is the source-to-sample distance, the higher the coherence). A perfectly coherent system is a hypothetical monochromatic point-like source, a real source has a low or high degree of coherence depending on how these two requirements are satisfied. To better define the degree of coherence, for partial coherent sources, coherence lengths can be used. The temporal one $L_t = \lambda^2/\Delta\lambda$ (with $\Delta\lambda$ equal to the spectral bandwidth) defines the length up to which the beam can be considered as coherent along the propagation direction. The spatial coherence length $L_s = \lambda z_1/S$ (where $z_1$ is the source-to-sample distance and $S$ is the source size) defines a scale for the coherence on the object plane, which is perpendicular to the beam propagation direction (Fig. 2.2).

A feature on the object plane with a size comparable to $L_s$ will see the beam as spatially coherent (Cloetens et al. (1996)).

## 2.4 Phase-based Techniques for x-ray Imaging

Phase-based x-ray techniques hold the potential to greatly improve the quality of x-ray imaging, especially in the biomedical field. As mentioned before, the difference between the refractive decrement $\delta$ and the absorption term $\beta$, in the diagnostic x-ray energy range, is typically 1000 times big. As a consequence, the phase shift effect induced by the object on the beam, can be much larger with respect to the absorption effect, which is the base principle of the image formation in conventional x-ray techniques. This implies that the sensitivity of the imaging system can be enhanced, particularly when the contrast rising from the differences

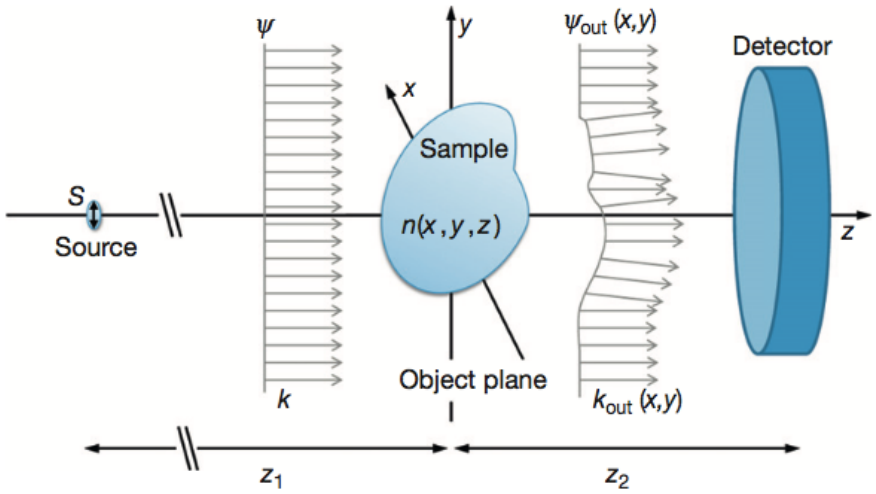


**Figure 2.2:** Sketch of model treating x-rays as waves. A parallel monochromatic x-ray beam, represented by the plane wave $c$, impinges on a sample, characterised by the refractive index $n(x, y, z)$. The wave $\Psi_{out}(x, y)$ leaving the object plane is locally affected by the object, both in intensity and phase. $k$ and $k_{out}$ are the wave vectors of $\Psi$ and $\Psi_{out}(x, y)$, respectively. $z_1$ is the source-to-sample distance, $z_2$ is the sample-to-detector distance, and $S$ is the source size.

in absorption coefficient is not sufficient to distinguish tiny details inserted in a similar background, as for example for breast tumour embedded in healthy glandular tissue. Moreover, since phase-based x-ray imaging methods could provide good quality images even with low absorption in the body, energies higher than those typically used in medical imaging could be exploited. The quantities $\beta$ and $\delta$ both decrease with growing energy, but, as seen in the previous paragraph, while $\beta$ goes down with the third power of the energy, $\delta$ decreases with the second power (eq. 2.4). This means that, by selecting a suitable energy, it is possible to ensure a low radiation dose to the patient keeping low the imaginary part $\beta$, and at the same time obtain good phase-contrast images (with well discriminated features) being the refractive index decrement sufficiently large. Different phase-based x-ray imaging methods have been studied in the last 20 years and are nowadays in continuous development. In the following paragraphs the most common approaches, which have reached interesting results in the medical field and could possibly be applied into clinical practice will be briefly described, namely: analyser-based imaging (ABI), edge illumination (EI), Talbot (or grating) x-ray interferometry (GI). Several

reviews partially or fully dedicated to these topics have appeared quite regularly in the recent scientific literature: inspiring articles are due for instance to Fitzgerald, Suortti and Thomlinson (2003), Lewis (2004), Momose (2005), Zhou and Brahme (2008); moreover, Olivo (2010) focused on the patents and intellectual property issues related to phase-sensitive techniques; finally, very wide-ranging works have been released by Nugent (2010) and Bravin et al. (2013). Particular attention will be paid on propagation-based phase contrast x-ray imaging method (PBI), as it has been used for the scope of the present thesis work.

### 2.4.1 Propagation-based imaging technique

In PBI technique, an x-ray beam with a high degree of coherence irradiates the sample, giving rise to a phase shift that is spatially varying. As the beam passes through the object, parts of the wavefront, having done different deflections, interfere producing a characteristic pattern that is after registered by a detector placed at a suitable distance (Fig.3) (Snigirev et al. (1995), Cloetens et al. (1996)). Due to the Fresnel diffraction, the phase shifts are then converted into detectable intensity variations (Born et al. (1999)).

As this technique doesn?t require optical elements between the sample and the detector, its great advantage with respect to the other phase-contrast imaging methods is the simplicity of the setup. This avoids the possibility of arising aberration from the optical elements and implies a potentially high spatial resolution, which depends mainly on the size of the source (Pogany et al. (1997), Arhatari et al. (2004), Gureyev et al. (2008)). The propagation-based imaging modality can be included in the differential phase-contrast imaging methods, as the image signal depends on the spatial variation of the phase shift induced by the sample rather than directly on it. The image contrast in this method is, at a first approximation, proportional to the Laplacian of the phase shift in a plane perpendicular to the optical axis. A crucial dependence of the phase-contrast signal on the effective propagation distance can be defined as: $D = dl/(d + l)$, where $d$ and $l$ are the sample-to-detector and the source-to-sample distances respectively. For $l \gg d$

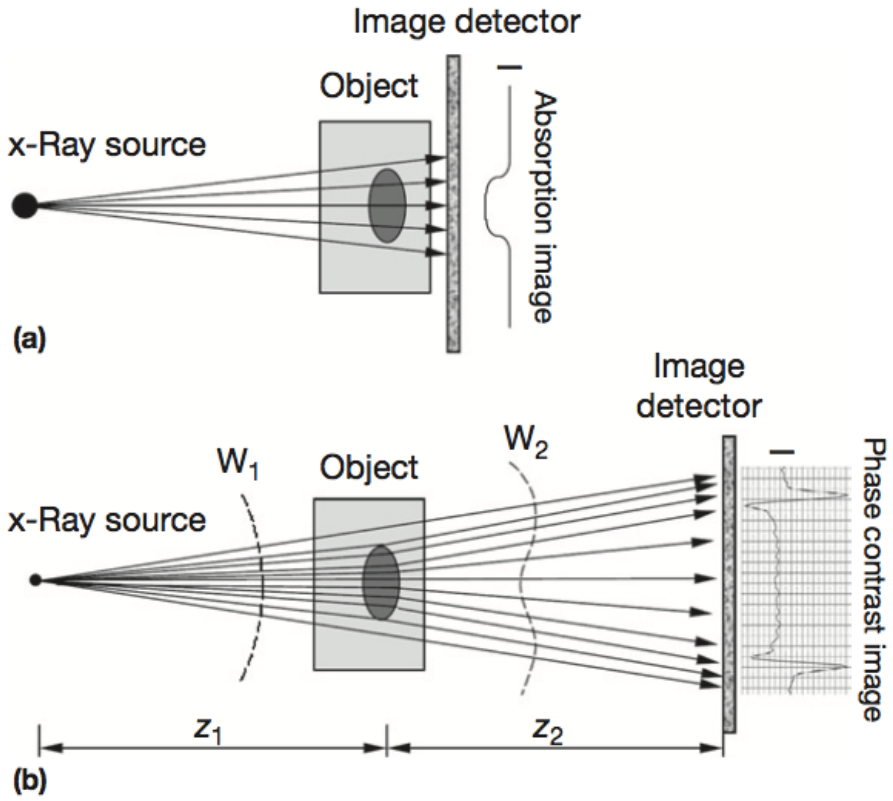


**Figure 2.3:** Comparison between (a) conventional attenuation imaging, where the detector is in contact with the sample, and (b) PBI, where the detector is placed at a suitable distance to allow the detection of a typical edge-enhanced image profile. (Reproduced from Zhou and Brahme (2008))

the effective distance is determined by the propagation distance, so $D \simeq d$, and this a usual condition found in synchrotron setups. When increasing the defocus distance, taking into account a monochromatic plane wave and considering the transverse characteristic length scale $h$ of the sample, four different regimes may be defined (Mayo et al. (2002), Gureyev (2003)):

- Absorption regime: the sample-to-detector distance is close to zero.
- Near-field diffraction regime: the effective propagation distance is relatively small, such that $r_F^2 = \lambda D \ll h^2$. The term $r_F$ is the radius in the sample plane of the so-called Fresnel zone, and it determines the finite region in the object that contributes to a point $P$ in the image. In this conditions, the contrast is formed locally around specific object features. The boundaries of the object

are strongly enhanced and a distinct interference pattern corresponds to every edge, giving reliable information on the geometry of the object. To express the above condition for the near-field regime, a Fresnel number must be defined as $N_F \equiv h^2/(\lambda D)$ , so that $N_F \gg 1$.

- Fresnel regime: here the defocus distance is $r_F^2 = \lambda D \approx h^2$, that is equivalent to $N_F \approx 1$.

- Fraunhofer regime: the effective propagation distance is quite large and is $r_F^2 = \lambda D \gg h^2$, and then $N_F \ll 1$. In this conditions, the interference fringes ca be well detected but they cannot be related to a specific edge of the sample, so that the shape of the sample is difficult to be recognised.

Thus, based on the different experimental setups, the Fresnel diffraction pattern highlights different features of the object. It can be demonstrated that the image is most sensitive to a given frequencies range $f$ of a particular phase feature at a distance $D$ defined as $D \approx 1/(2\lambda f^2)$. At this distance, the phase contrast contribution is maximised. In order to retrieve a quantitative information on the absorption and on the phase shift caused by the object on the beam, a series of algorithms have been studied. This inverse problem is usually solved by coupling a set of Fresnel diffraction patterns recorded at different distances $z$. However, an algorithm that calculates these two quantities by means of one single PB distance has been also developed and widely diffused (Gureyev et al. (1995), Bronnikov (1999), Paganin et al. (2002), Gureyev et al. (2004), Beltran et al. (2010)).

#### 2.4.1.1 General Propagation-based Imaging formalism

The base theory of the propagation-based imaging technique is the Fresnel diffraction formalism. As described before in eq. 2.10, in certain conditions where there is a spatial coherent x-ray beam of a wavelength incident on a thin sample defined by a complex refractive index distribution $n(x, y, z)$, the wave exiting from the surface of the sample can be computed multiplying the wave at the entrance of the object by the object complex transmission function. Now, considering the wave going out from the

object $\Psi_{obj}$ as paraxial, along the propagation distance $D$, before being recorded by the detector, all the non-negligible plane-wave components of the field make a small angle with the optical axis, then the wave after a certain path $D$ can be expressed as:

$$\Psi_D(\mathbf{x}) = P_D(\mathbf{x}) \otimes \Psi_{obj}(\mathbf{x}) \tag{2.16}$$

where $\otimes$ is the convolution symbol, $\mathbf{x} = (x, y)$ are the spatial coordinates in the plane orthogonal to the propagation direction $z$ and $P_D(x)$ denotes the Fresnel propagator, that can be described as (Born et al. (1999)):

$$P_D(\mathbf{x}) = \frac{exp^{\frac{i2\pi D}{\lambda}}}{i\lambda D} exp(i\frac{\pi}{\lambda D}|\mathbf{x}|^2) \tag{2.17}$$

As known, a wave propagating in free space can be descripted in the Fourier domain. Eq. 2.17 in the Fourier domain becomes:

$$\tilde{P}_D(\mathbf{f}) = exp(i2\pi D/\lambda) exp(-i\pi\lambda D|\mathbf{f}|^2 \tag{2.18}$$

with $f = (f_x, f_y)$ indicating the spatial frequency coordinates. In the same way, naming $\tilde{\Psi}_{obj}$ and $\tilde{\Psi}_D$ the Fourier transform of $\Psi_{obj}$ and $\Psi_D$ respectively, eq. 2.16 will be:

$$\tilde{\Psi}_D(\mathbf{f}) = \tilde{P}_D(\mathbf{f}) \cdot \tilde{\Psi}_{obj}(\mathbf{f}) \tag{2.19}$$

After covering the propagation distance $D$, the effective intensity on the detector is given by:

$$I_D(\mathbf{x}) = |\Psi_D(\mathbf{x})|^2 = |P_D(\mathbf{x}) \otimes \Psi_{obj}(\mathbf{x})|^2 \tag{2.20}$$

In the Fourier domain, eq. 2.20 can be expressed in the near-field diffraction regime as (Guigay (1977)):

$$\tilde{I}_D(\mathbf{f}) = \int T\left(\mathbf{x} - \frac{\lambda D f}{2}\right) T^*\left(\mathbf{x} + \frac{\lambda D f}{2}\right) exp(-i2\pi\mathbf{x}\cdot\mathbf{f})\mathrm{d}x \tag{2.21}$$

For small propagation distances, the transmission function $T$ can be approximated with a Taylor first order expansion (Turner et al. (2004)):

$$T\left(\mathbf{x} + \frac{\lambda D f}{2}\right) \approx T(\mathbf{x}) + \frac{1}{2}\lambda D\mathbf{f}\cdot\nabla T(\mathbf{x}) \tag{2.22}$$

If this last expression for $T$ is used into eq. 2.21, considering only the terms linear with respect to $D$, the equation becomes:

$$I_D(\mathbf{x}) = I_T(\mathbf{x}) - \frac{\lambda D}{2\pi}\nabla[I_T(\mathbf{x})\nabla\phi(\mathbf{x})] \tag{2.23}$$

Again, for small propagation distances eq. 2.23 is equal to:

$$\nabla[I_T(\mathbf{x})\nabla\phi(\mathbf{x})] = -\frac{2\pi}{\lambda}\frac{\partial}{\partial z}I_T(\mathbf{x}) \tag{2.24}$$

which represents the so-called transport of intensity equation (Teague (1982)). Under the assumption that the non-propagated wave $\Psi_{obj}$ is varying sufficiently slowly in the plane perpendicular to the propagation direction, $I_T$ can be computed outside the gradient operator so that:

$$I_D(\mathbf{x}) = I_T(\mathbf{x}) = \left[1 - \frac{\lambda D}{2\pi}\nabla^2\phi(\mathbf{x})\right] \tag{2.25}$$

Accordingly, for small propagation distances and for slowly varying object absorption, the contrast is proportional to the Laplacian of the phase of the object. Moreover,

the contrast increases for growing propagation distances $D$, until the limit given by the approximation given in eq. 2.22. In the next paragraph, it will be explained how, under certain conditions, eq. 2.25 can be used to retrieve the phase of the object from the measurement of the intensity at a single propagation distance (Gureyev et al. (1995), Bronnikov (1999), Paganin et al. (2002), Beltran et al. (2010)).

#### 2.4.1.2 Derivation of the TIE-Hom Phase retrieval algorithm

To derive the algorithm for quantitative phase extraction from a single distance image, it is useful to firstly assume that the source-to-sample distance ($z_1$ in Fig. 2.3 is infinite, in order to have a collimated illumination and consider the magnification as unit. A second important assumption that has to be done is the "homogeneity" of the object, i.e. the sample has to be composed of a single material. When considering a normally incident plane-wave radiation of constant intensity over the sample area, the contact image, and so the intensity of the beam exiting from the sample surface ($z = 0$), is well described by the Beer?s absorption law:

$$I(\mathbf{x}, z = 0) = I_{IN} e^{-\mu T(\mathbf{x})} \tag{2.26}$$

As in the previous paragraphs, $T(\mathbf{x})$ is the transmission function, i.e. the projected thickness of the homogeneous object into the detector plane, $\mu$ is the linear absorption coefficient, and $I_{IN}$ is the intensity of the incident wave. The phase of the irradiating beam, $\phi(\mathbf{x})$, exiting from the sample, if the sample can be considered sufficiently thin, will be proportional to the transmission function:

$$\phi(\mathbf{x}, z = 0) = -\frac{2\pi}{\lambda} \delta T(\mathbf{x}) \tag{2.27}$$

where $\delta$ is the real part of the refractive index. Substituting eq. 2.26 and eq. 2.27 into eq. 2.24, gives a resulting equation that is non-linear in $T(\mathbf{x})$, however it is possible to re-write it as a linear equation in $e^{-\mu T(\mathbf{x})}$:

$$-\frac{\delta}{\mu}I_{IN}\nabla^2 e^{-\mu T(\mathbf{x})} = \frac{\partial}{\partial z}I(\mathbf{x}, z=0) \tag{2.28}$$

using the following identity:

$$\partial\nabla\cdot\left(e^{-\mu T(\mathbf{x})}\nabla T(\mathbf{x})\right) = -\frac{\delta}{\mu}\nabla^2 e^{-\mu T(\mathbf{x})} \tag{2.29}$$

Taking into account a second sample-to-detector distance ($z_2$ in Fig. 2.3), the right-hand term of eq. 2.28 using the intensity measurements can be:

$$\frac{\partial}{\partial z}I(\mathbf{x}, z=0) \approx \frac{I(\mathbf{x}, z=2) - e^{-\mu T\mathbf{x}I_{IN}}}{z_2} \tag{2.30}$$

Using this new expression and re-arranging terms, eq. 2.28 can be written as:

$$\left(-\frac{z_2\delta}{\mu}\nabla^2 + 1\right)e^{-\mu T(\mathbf{x})} = \frac{I(\mathbf{x}, z=z_2)}{I_{IN}} \tag{2.31}$$

At this point, to proceed, it is useful to represent the contact ($z=0$) and the phase contrast image ($z=z_2$) as Fourier integrals:

$$\begin{cases} I_{IN}e^{-\mu T(\mathbf{x})} = \frac{I_{IN}}{2\pi}\iint \mathcal{F}\left\{e^{-\mu T(\mathbf{x})}\right\}e^{i\mathbf{k}\cdot\mathbf{x}}\mathrm{d}\mathbf{k} \\ I(\mathbf{x}, z=z_2) = \frac{1}{2\pi}\iint \mathcal{F}\left\{I(\mathbf{x}, z=z_2)\right\}e^{i\mathbf{k}\cdot\mathbf{x}}\mathrm{d}\mathbf{k} \end{cases} \tag{2.32}$$

with $\mathcal{F}\{\}$ indicating the Fourier transformation. These last two definitions can be then substituted in eq. 2.31 to have:

$$F\left\{e^{-\mu T(\mathbf{x})}\right\} = \mu\frac{\mathcal{F}\left\{I(\mathbf{x}, z=z_2)\right\}/I_{IN}}{z_2\delta|\mathbf{k}|^2 + \mu} \tag{2.33}$$

It is possible then to solve eq. 2.33 for $T(\mathbf{x})$, taking its inverse Fourier transform:

$$T(\mathbf{x}) = -\frac{1}{\mu}\log_e\left(\mathcal{F}^{-1}\left\{\mu\frac{\mathcal{F}\left\{I(\mathbf{x}, z=z_2)\right\}/I_{IN}}{z_2\delta|\mathbf{k}|^2+\mu}\right\}\right) \tag{2.34}$$

To complete the derivation, it is necessary to remove the first assumption of infinite distance between source and object. It is demonstrable, by means of the Fresnel diffraction integral (Papoulis (1981)), that the intensity of a weakly refracting sample illuminated by a point source, at a certain distance $z = z_1$ from it, is linked to the intensity $I_\infty(\mathbf{x}, z)$, which would result from normally incident collimate illumination of the same sample, by (Pogany et al. (1997)):

$$I_{z_1}(\mathbf{x}, z) = \frac{1}{M^2}I_\infty\left(\frac{x}{M}, \frac{z}{M}\right) \tag{2.35}$$

where $M = (z_1 + z_2)/z_1$, represents the lignification of the image resulting from the point-source illumination. This last equation can be used to transform eq. 2.34 into a form suitable for a point-source illumination that is the final result:

$$T(\mathbf{x}) = -\frac{1}{\mu}\log_e\left(\mathcal{F}^{-1}\left\{\mu\frac{\mathcal{F}\left\{M^2 I(M\mathbf{x}, z=z_2)\right\}/I_{IN}}{z_2\delta|\mathbf{k}|^2/M+\mu}\right\}\right) \tag{2.36}$$

This lead to the solution of the transport-of-intensity equation seen above (eq.2.24), for the transmission function $T(\mathbf{x})$ of a homogeneous object, using one single propagation distance. This single image, using eq. 2.26 and eq. 2.27, can easily give information about the intensity and the phase of the radiation exiting the sample surface.

### 2.4.2 Analyser-Based Imaging

Analyser-based technique is based on the use of an analyser crystal placed between the object and the detector (Fig. 2.4), it has to be noticed that in the figure all the crystals are used in Bragg geometry, but it is known that alternative arrangements can also use the Laue diffraction (Chapman et al. (1996), Kitchen et al. (2011)).

As for the PBI, for its application, a mono-energetic and highly collimated x-ray beam is fundamental. The crystal behaves as band-pass filter, modulating the intensity of the beam after having crossed the sample.

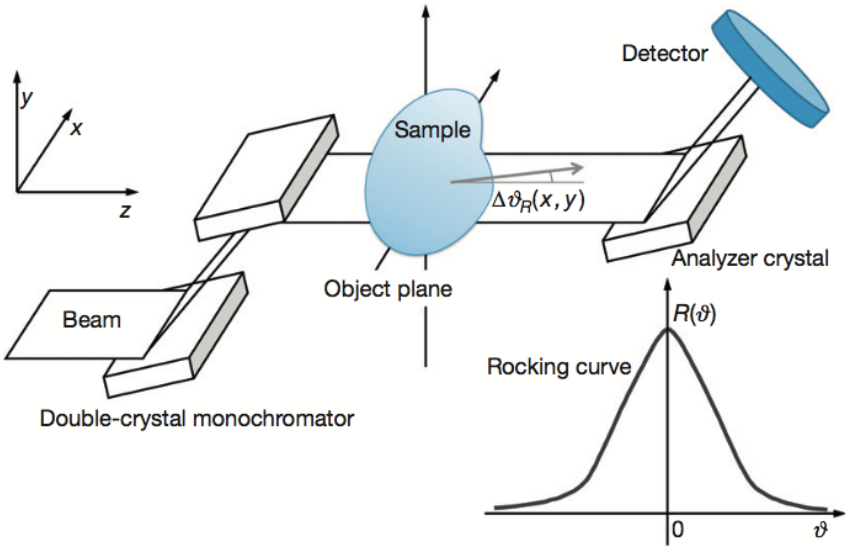


**Figure 2.4:** Scheme of an ABI setup. The rocking curve is obtained with no sample in the beam. When the sample is in the beam, the rocking curve acts as an angular band-pass filter and the analyser crystal selectively diffracts photons according to their deviation angle $\Delta\theta_R(x, y)$ upon exiting the sample. (Reproduced from Rigon (2014))

This allows to exploit the phase effects as an additional source of contrast on the image. The basic principle relies on the fact that, when the analyser crystal reaches perfectly the peak of its reflectivity curve (known as rocking curve), it can act as an anti-scattering grid, giving a well-defined pure absorption image. When the crystal is positioned at different points of the rocking curve, it is possible to obtain additional phase effects (such as refraction). ABI images, indeed, are usually represented by a mixture of absorption, refraction, small and ultra-small angle scattering effects. There is not a precise distinction of these effects, as they have similar physical origin (Davis (1994)), however it is possible to outline the differences among them as follows. Taking into account the spatial resolution of the detector in use in a certain setup, refraction refers to the effect of an object big with respect to the detector pixel size. In this conditions, a precise deviation

angle $\alpha(x, y)$ can be related to each point of the sample plane corresponding to each pixel on the detector. The refraction angle can be calculated as:

$$\alpha \cong \frac{1}{k}\sqrt{\left(\frac{\partial}{\partial x}\phi(\mathbf{x})\right)^2 + \left(\frac{\partial}{\partial y}\phi(\mathbf{x})\right)^2} = \frac{1}{k}|\nabla\phi(\mathbf{x})| \tag{2.37}$$

where $k$ is the wave number, and it is usually a few microradians. Scattering effect, contrariwise, refers internal structure smaller than the detector pixel size, so not resolved by the detector (Rigon et al. (2003)). Small-angle scattering (SAXS), deal with diffuse photon deviations in the range of milliradians, that come from nano-scale internal structures. Lastly, ultra-small-angle x-ray scattering (USAXS), applies on larger structure (from hundreds of nanometers to several micrometers) giving deviation angles in the microradians range. This last distinction between SAXS and USAXS is possible thanks to the angular selection of the crystal that acts in the microradians range, accordingly, while SAXS is totally absorbed, USAXS is comparable to the acceptance window of the analyser. This means that the width of the rocking curve is in the same order of magnitude than the tiny deviations experienced by the beam crossing the object. The basic idea is that, the beam, after crossing the sample so after being deviated in the microradians range, arrives onto the analyser crystal whit a certain misalignment angle with respect to the un-deviated photons beam. Therefore, since the deviated photons have different probability to reach the detector because of the extreme sensitivity of the rocking curve to small angular displacement, it is possible to say that the analyser transforms this angular deviation in a modulation of the beam intensity on the detector. The simplest mathematical model to describe the ABI behaviour considers that the photons exiting from the sample plane $xy$ at a certain point $(x, y)$ could be either give a small angle x-ray scattering (SAXS) or refracted with a defined refraction angle $\alpha(x, y)$, with respect to the propagation direction $z$. It has to be noticed that, ABI imaging systems are sensitive just to the component of the wave that lies on the diffraction plane of the crystal, $yz$ in the reference system of Fig. 2.4. Thus, the projection of the refraction angle $\alpha(x, y)$ on the plane $yz$ will be:

$$\Delta\theta_R(x,y) = \frac{1}{k}\frac{\partial}{\partial y}\phi(x,y) = -\frac{\partial}{\partial y}\int \delta(x,y,z)\mathrm{d}z \cong -\frac{r_0\lambda^2}{2\pi}\frac{\partial}{\partial y}\int \rho_e(x,y,z)\mathrm{d}z \quad (2.38)$$

where $r_0 \cong 2.82 \times 10^{-15}\ m$ is the classical electron radius and $\rho_e$ is the electron density (i.e. the number of electrons per unit volume). Eq. 2.38 represents the so-called refraction angle, that is actually the component of the refraction angle in the crystal diffraction plane, as it is the one to which ABI system is sensitive. It is, then, possible to define the actual intensity that reaches the detector when the analyser crystal is set at a certain angular position $\overline{\theta}$ of the rocking curve $R(\theta)$, as:

$$I(\overline{\theta};x,y) = I_R(x,y)R(\overline{\theta} + \Delta\theta_R(x,y)) \quad (2.39)$$

where $I_R(x,y)$ is the intensity accounting for absorption and extinction and is called apparent absorption (Chapman et al. (1997)). When the refraction angle is small, eq. 2.39 can be further approximated, by means of a first order Taylor expansion, to:

$$I(\overline{\theta};x,y) = I_R(x,y)[R(\overline{\theta}) + \dot{R}(\overline{\theta}) \cdot \Delta\theta_R(x,y)] \quad (2.40)$$

with $\dot{R}(\overline{\theta})$ indicating the derivative of the rocking curve $R(\theta)$ at the angular position $\overline{\theta}$. This last equation, highlights how images acquired with this technique, could contain different amount of extinction and refraction dependently on the chosen working point $\overline{\theta}$.

### 2.4.3 Edge Illumination Imaging

Edge Illumination (EI) method is based, in a similar way to the ABI, on the detection of the refraction angles suffered by photons when crossing the object. Contrariwise to the ABI instead, there is no need for a second crystal between the sample and the detector, thus leading to a simplified setup well-suited for conventional x-ray tubes, as it doesn't require an elevated degree of mechanical

stability and beam coherence (Olivo and Speller (2007a), Olivo and Speller (2007b)). However, to describe the working principle, it is useful to refer to the simplest implementation of the technique, that is the one used in synchrotron setup, see Fig. 2.5 (Olivo et al. (2011, 2012, 2013)). There is a first slit placed before the sample called *pre-sample slit*, that is meant to collimate the beam and has an aperture usually of a few micrometers. In front of the detector, there is then a second slit, called detector slit, that is aligned with one pixel's row of the detector.

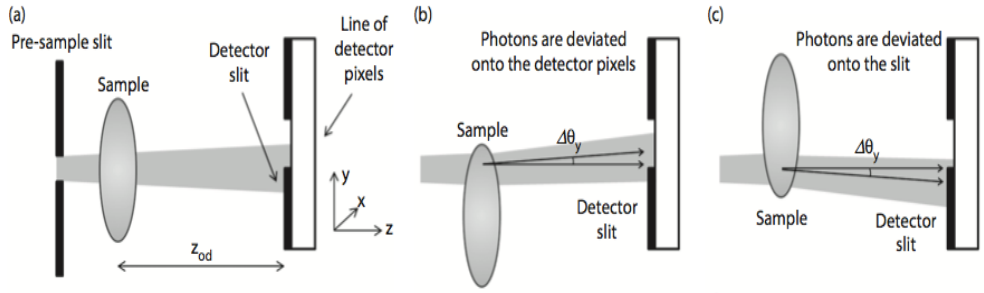


**Figure 2.5:** Scheme of a typical synchrotron EI setup based on the use of two slits (not to scale). (a) No refraction from the object, (b) photons refracted onto the detector pixels increase the detector signal, and (c) photons deviated out of the detector pixels decrease the detector signal. (Reproduced from noa (2017))

There is a slight misalignment between the two slits, in such a way that the beam exiting from the first slit, reaches the edge of the *detector slit*, thus the beam is partially stopped by the second slit (*partial illumination* condition). If there is a sample in the system, the beam will be refracted, thus the small portion of the beam falling on the *detector slit* will be shifted by the quantity $\Delta y = z_{od} \tan(\Delta\theta_y)$, where $z_{od}$ represents the distance between the sample and the *detector slit*, and $\Delta\theta_y$ is the component of the refraction angle in the direction orthogonal to the slits. For small refraction angles, in the order of microradians, the shift can be approximated to $\Delta y \approx z_{od} \cdot (\Delta\theta_y)$, the displacement is typically less than few micrometers for propagation distances of about 1 $m$. If the beam is shifted towards the aperture, the counts on the detector will increase, vice versa, if the deviation goes towards the slits the counts on the detector will be less. In this way, it is possible to translate the refraction angle caused by the object, into a modulation of the intensity on the

detector. The whole image of the sample can be obtained scanning the sample, step by step, in the direction orthogonal to the slits and then pasting together all the single lines. When using conventional x-ray tube, the above described working principle, can be achieved by substituting the two slits with two masks (Fig. 6), characterised by several apertures, avoiding the vertical sample scan (Olivo and Speller (2007a)). The period of the mask is commensurate to the detector pixel size, in order for the apertures to match every pixel row.

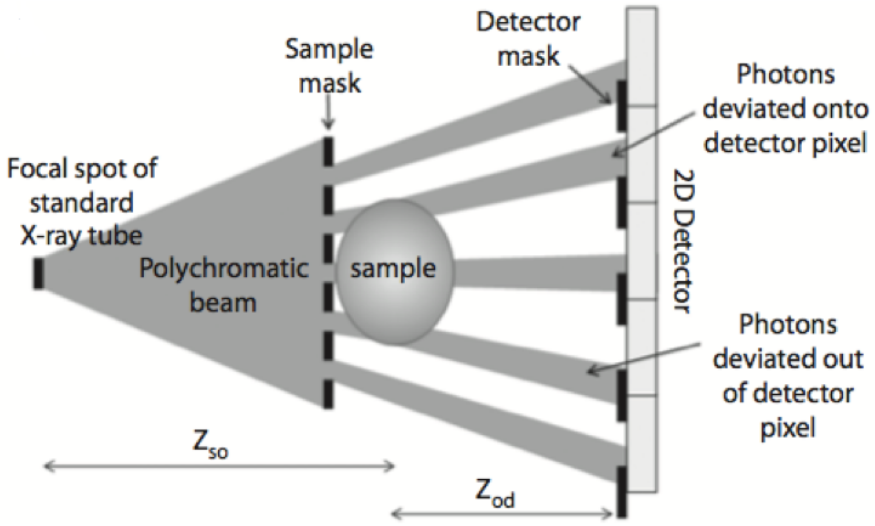


**Figure 2.6:** Scheme of laboratory EI setup based on the use of an X-ray tube and a pair of masks (not to scale))

As there is no more need for sample scans, the total acquisition time could be much smaller, as different zones of the object can be acquired at the same time taking advantage of different aperture pairs. There are other existing implementations of EI method, that foresee, for example, the removal of the second mask using a detector with sharp boundaries between each pixel row (Krejci et al. (2010)), or a high-resolution detector. In this latter case, the deviation caused by the refraction, the fall of the intensity caused by the absorption, and the beam broadening caused by the scattering effect, can be retrieved by fitting the values of various pixels illuminated by each portion of the beam (Vittoria et al. (2014, 2015)). Lastly, another implementation, able to be sensitive to beam displacement in two directions, can be

settled-up using L-shaped masks, improving the sample visualisation and simplifying the integration of the refraction signal to obtain the phase map, but increasing the setup complexity and the acquisition time (Olivo et al. (2009), Kallon et al. (2015)).

### 2.4.4 Grating x-ray Interferometry

Grating-based imaging (GI) system bases its functioning on the use of grating interferometers. The technique is based on the optical phenomenon discovered by Talbot in the 1830s and foresees the use of a phase grating and an analyzer grating (Momose (2003)). The image reproducing the grating is repeated at regular distances $d_T = \frac{2p^2}{\lambda}$, where $p$ is the period of the grating. As in the previous cases, the object causes absorption, refraction and scattering effect on the x-ray beam, modifying the interference pattern. Accordingly, the angular shifting can be exploited as an intensity modulation on the detector, measuring the changes in the interference pattern with and without the sample. The second grating, is placed at a fractional Talbot length distance ($d_T$), and it is needed to analyse the interference pattern (see Fig. 2.7).

There are two methods meant to distinguish the different contributions to the signal: the phase-stepping technique (Weitkamp et al. (2005)) and the method making use of the Moiré fringes (Momose (2003)). Both of them can be used to obtain planar and tomographic images and are able to produce information about both real and imaginary component of the complex refractive index (Weitkamp et al. (2005), Momose et al. (2009)). The described setup, is the one typically used in synchrotron facilities as it requires a high degree of spatial coherence of the x-ray beam; however, the GI method can be implemented in conventional x-ray tubes, using a third additional grating, called Talbot-Lau interferometer. Conventional x-ray sources, can be efficiently used with the phase stepping configuration as the position of the interference fringes arising behind the source grating is independent of the wavelength over a wide x-ray energy range (Weitkamp et al. (2005)). On the contrary, the Moiré configuration allows the use of a moderate polychromaticity,

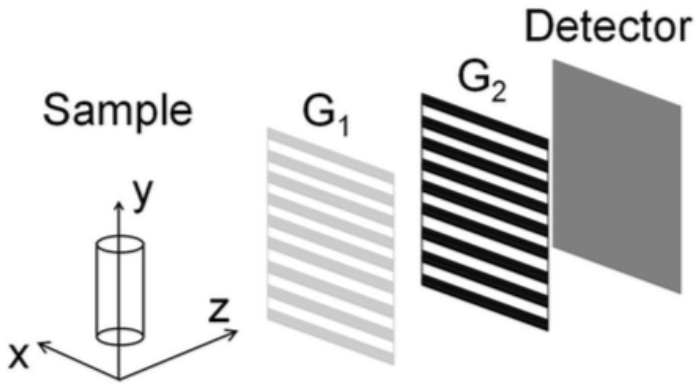


**Figure 2.7:** Scheme of GI setup. A pattern of x-ray interference fringes is formed downstream a linear diffraction grating G1 (beam splitter); its local distortions from its ideal regular shape contain information on the sample structure. Since the fringes are too closely spaced to be resolved by the pixel detector used to record images, an additional absorption grid (G2, analyser grating) in front of the detector is needed to transform fringe-position information into intensity values on the detector pixels.

as a wide bandwidth of energies decreases the visibility of the Moiré fringes and worsens the image quality (Momose et al. (2006)).

# References

, 2017. Handbook of X-ray Imaging: Physics and Technology. URL: https://www.crcpress.com/Handbook-of-X-ray-Imaging-Physics-and-Technology/Russo/p/book/9781498741521.

Arhatari, B.D., Mancuso, A.P., Peele, A.G., Nugent, K.A., 2004. Phase contrast radiography: Image modeling and optimization. Review of Scientific Instruments 75, 5271–5276. URL: http://aip.scitation.org/doi/abs/10.1063/1.1819652, doi:10.1063/1.1819652.

Auweter, S., Herzen, J., Willner, M., Grandl, S., Scherer, K., Bamberg, F., Reiser, M., Pfeiffer, F., Hellerhoff, K., 2014. X-ray phase-contrast imaging of the breast - Advances towards clinical implementation. British Journal of Radiology 87. doi:10.1259/bjr.20130606.

Azároff, L.V., 1968. Elements of X-ray crystallography. McGraw-Hill. Google-Books-ID: e0NRAAAAMAAJ.

Beltran, M.A., Paganin, D.M., Uesugi, K., Kitchen, M.J., 2010. 2d and 3d X-ray phase retrieval of multi-material objects using a single defocus distance. Opt. Express, OE 18, 6423–6436. URL: https://www.osapublishing.org/abstract.cfm?uri=oe-18-7-6423, doi:10.1364/OE.18.006423.

Born, M., Wolf, E., Bhatia, A.B., Clemmow, P.C., Gabor, D., Stokes, A.R., Taylor, A.M., Wayman, P.A., Wilcock, W.L., 1999. Principles of Optics: Electromagnetic Theory of Propagation, Interference and Diffraction of Light. 7 edizione ed., Cambridge University Press, Cambridge ; New York.

Bravin, A., Coan, P., Suortti, P., 2013. X-ray phase-contrast imaging: From pre-clinical applications towards clinics. Physics in Medicine and Biology 58, R1–R35. doi:10.1088/0031-9155/58/1/R1.

Bronnikov, A.V., 1999. Reconstruction formulas in phase-contrast tomography. Optics Communications 171, 239–244. URL: http://www.sciencedirect.com/science/article/pii/S0030401899005751, doi:10.1016/S0030-4018(99)00575-1.

Chapman, D., Thomlinson, W., Arfelli, F., Gmür, N., Zhong, Z., Menk, R., Johnson, R.E., Washburn, D., Pisano, E., Sayers, D., 1996. Mammography imaging studies using a Laue crystal analyzer. Review of Scientific Instruments 67, 3360–3360. URL: http://aip.scitation.org/doi/abs/10.1063/1.1147502, doi:10.1063/1.1147502.

Chapman, D., Thomlinson, W., Johnston, R.E., Washburn, D., Pisano, E., Gmür, N., Zhong, Z., Menk, R., Arfelli, F., Sayers, D., 1997. Diffraction enhanced x-ray imaging. Phys. Med. Biol. 42, 2015. URL: http://stacks.iop.org/0031-9155/42/i=11/a=001, doi:10.1088/0031-9155/42/11/001.

Cloetens, P., Barrett, R., Baruchel, J., Guigay, J.P., Schlenker, M., 1996. Phase objects in synchrotron radiation hard x-ray imaging. Journal of Physics D: Applied Physics 29, 133–146. doi:10.1088/0022-3727/29/1/023.

Cullen, D.E., Hubbell, J.H., Kissel, L., 1997. Epdl97: The Evaluated Photo Data Library '97 Version. Technical Report UCRL–50400-Vol.6-Rev.5. Lawrence Livermore National Lab., CA (United States). URL: https://www.osti.gov/scitech/biblio/295438. dOI: 10.2172/295438.

Davis, T.J., 1994. A unified treatment of small-angle X-ray scattering, X-ray refraction and absorption using the Rytov approximation. Acta Cryst A, Acta Cryst Sect A, Acta Crystallogr A, Acta Crystallogr Sect A, Acta Crystallogr A Found Crystallogr, Acta Crystallogr Sect A Found Crystallogr 50, 686–690. URL: http://scripts.iucr.org/cgi-bin/paper?as0666, doi:10.1107/S0108767394003478.

Diemoz, P., Bravin, A., Langer, M., Coan, P., 2012. Analytical and experimental determination of signal-to-noise ratio and figure of merit in three phase-contrast imaging techniques. Optics Express 20, 27670–27690. doi:10.1364/OE.20.027670.

Fitzgerald, R., . Phase-Sensitive X-Ray Imaging. Physics Today URL: http://physicstoday.scitation.org/doi/10.1063/1.1292471, doi:10.1063/1.1292471.

Guigay, J., 1977. Fourier transform analysis of Fresnel diffraction patterns and in-line holograms. Optik 49.

Gureyev, T.E., 2003. Composite techniques for phase retrieval in the Fresnel region. Optics Communications 220, 49–58. URL: http://www.sciencedirect.com/science/article/pii/S0030401803013531, doi:10.1016/S0030-4018(03)01353-1.

Gureyev, T.E., Davis, T.J., Pogany, A., Mayo, S.C., Wilkins, S.W., 2004. Optical phase retrieval by use of first Born- and Rytov-type approximations. Appl. Opt., AO 43, 2418–2430. URL: https://www.osapublishing.org/abstract.cfm?uri=ao-43-12-2418, doi:10.1364/AO.43.002418.

Gureyev, T.E., Nesterets, Y.I., Stevenson, A.W., Miller, P.R., Pogany, A., Wilkins, S.W., 2008. Some simple rules for contrast, signal-to-noise and resolution in in-line x-ray phase-contrast imaging. Opt. Express, OE 16, 3223–3241. URL: https://www.osapublishing.org/abstract.cfm?uri=oe-16-5-3223, doi:10.1364/OE.16.003223.

Gureyev, T.E., Roberts, A., Nugent, K.A., 1995. Partially coherent fields, the transport-of-intensity equation, and phase uniqueness. J. Opt. Soc. Am. A, JOSAA 12, 1942–1946. URL: https://www.osapublishing.org/abstract.cfm?uri=josaa-12-9-1942, doi:10.1364/JOSAA.12.001942.

Jackson, J.D., 1975. Classical electrodynamics. Wiley. Google-Books-ID: _7rvAAAAMAAJ.

Kallon, G.K., Wesolowski, M., Vittoria, F.A., Endrizzi, M., Basta, D., Millard, T.P., Diemoz, P.C., Olivo, A., 2015. A laboratory based edge-illumination x-ray phase-contrast imaging setup with two-directional sensitivity. Appl. Phys. Lett. 107, 204105. URL: http://aip.scitation.org/doi/abs/10.1063/1.4935983, doi:10.1063/1.4935983.

Kitchen, M.J., Paganin, D.M., Uesugi, K., Allison, B.J., Lewis, R.A., Hooper, S.B., Pavlov, K.M., 2011. Phase contrast image segmentation using a Laue analyser crystal. Phys. Med. Biol. 56, 515. URL: http://stacks.iop.org/0031-9155/56/i=3/a=001, doi:10.1088/0031-9155/56/3/001.

Krejci, F., Jakubek, J., Kroupa, M., 2010. Hard x-ray phase contrast imaging using single absorption grating and hybrid semiconductor pixel detector. Review of Scientific Instruments 81, 113702. URL: http://aip.scitation.org/doi/abs/10.1063/1.3499372, doi:10.1063/1.3499372.

Lewis, R., 2004. Medical phase contrast x-ray imaging: Current status and future prospects. Physics in Medicine and Biology 49, 3573–3583. doi:10.1088/0031-9155/49/16/005.

Mayo, S.C., Miller, P.R., Wilkins, S.W., Davis, T.J., Gao, D., Gureyev, T.E., Paganin, D., Parry, D.J., Pogany, A., Stevenson, A.W., 2002. Quantitative X-ray projection microscopy: phase-contrast and multi-spectral imaging. J Microsc 207, 79–96.

Momose, A., 2003. Phase-sensitive imaging and phase tomography using X-ray interferometers. Opt. Express, OE 11, 2303–2314. URL: https://www.osapublishing.org/abstract.cfm?uri=oe-11-19-2303, doi:10.1364/OE.11.002303.

Momose, A., 2005. Recent advances in X-ray phase imaging. Japanese Journal of Applied Physics, Part 1: Regular Papers and Short Notes and Review Papers 44, 6355–6367. doi:10.1143/JJAP.44.6355.

Momose, A., Yashiro, W., Maikusa, H., Takeda, Y., 2009. High-speed X-ray phase imaging and X-ray phase tomography with Talbot interferometer and white synchrotron radiation. Opt. Express, OE 17, 12540–12545. URL: https://www.osapublishing.org/abstract.cfm?uri=oe-17-15-12540, doi:10.1364/OE.17.012540.

Momose, A., Yashiro, W., Takeda, Y., Suzuki, Y., Hattori, T., 2006. Phase Tomography by X-ray Talbot Interferometry for Biological Imaging. Jpn. J. Appl. Phys. 45, 5254. URL: http://iopscience.iop.org/article/10.1143/JJAP.45.5254/meta, doi:10.1143/JJAP.45.5254.

Nugent, K.A., 2010. Coherent methods in the X-ray sciences. Advances in Physics 59, 1–99. URL: https://doi.org/10.1080/00018730903270926, doi:10.1080/00018730903270926.

Olivo, A., 2010. Recent patents in X-ray phase contrast imaging. Recent Patents on Biomedical Engineering 3, 95–106. doi:10.2174/1874764711003020095.

Olivo, A., Bohndiek, S.E., Griffiths, J.A., Konstantinidis, A., Speller, R.D., 2009. A non-free-space propagation x-ray phase contrast imaging method sensitive to phase effects in two directions simultaneously. Appl. Phys. Lett. 94, 044108. URL: http://aip.scitation.org/doi/abs/10.1063/1.3078410, doi:10.1063/1.3078410.

Olivo, A., Diemoz, P.C., Bravin, A., 2012. Amplification of the phase contrast signal at very high x-ray energies. Opt. Lett., OL 37, 915–917. URL: https://www.osapublishing.org/abstract.cfm?uri=ol-37-5-915, doi:10.1364/OL.37.000915.

Olivo, A., Gkoumas, S., Endrizzi, M., Hagen, C.K., Szafraniec, M.B., Diemoz, P.C., Munro, P.R.T., Ignatyev, K., Johnson, B., Horrocks, J.A., Vinnicombe, S.J., Jones, J.L., Speller, R.D., 2013. Low-dose phase contrast mammography with conventional x-ray sources. Med Phys 40, 090701. doi:10.1118/1.4817480.

Olivo, A., Ignatyev, K., Munro, P.R.T., Speller, R.D., 2011. A coded-aperture based method allowing non-interferometric phase contrast imaging with incoherent X-ray sources. Nuclear Instruments and Methods in Physics Research Section A: Accelerators, Spectrometers, Detectors and Associated Equipment 648, S28–S31. URL: http://www.sciencedirect.com/science/article/pii/S0168900211000684, doi:10.1016/j.nima.2011.01.018.

Olivo, A., Speller, R., 2007a. A coded-aperture technique allowing x-ray phase contrast imaging with conventional sources. Appl. Phys. Lett. 91, 074106. URL: http://aip.scitation.org/doi/abs/10.1063/1.2772193, doi:10.1063/1.2772193.

Olivo, A., Speller, R., 2007b. Modelling of a novel x-ray phase contrast imaging technique based on coded apertures. Phys. Med. Biol. 52, 6555. URL: http://stacks.iop.org/0031-9155/52/i=22/a=001, doi:10.1088/0031-9155/52/22/001.

Paganin, D., Mayo, S.C., Gureyev, T.E., Miller, P.R., Wilkins, S.W., 2002. Simultaneous phase and amplitude extraction from a single defocused image of a homogeneous object. J Microsc 206, 33–40.

Papoulis, A., 1981. Systems and Transforms With Applications in Optics. Krieger Pub Co, Malabar, Fla.

Pogany, A., Gao, D., Wilkins, S.W., 1997. Contrast and resolution in imaging with a microfocus x-ray source. Review of Scientific Instruments 68, 2774–2782. URL: http://aip.scitation.org/doi/abs/10.1063/1.1148194, doi:10.1063/1.1148194.

Raven, C., Snigirev, A., Snigireva, I., Spanne, P., Souvorov, A., Kohn, V., 1996. Phase-contrast microtomography with coherent high-energy synchrotron x rays. Appl. Phys. Lett. 69, 1826–1828. URL: http://aip.scitation.org/doi/abs/10.1063/1.117446, doi:10.1063/1.117446.

Rigon, L., 2014. 2.08 - x-Ray Imaging with Coherent Sources, in: Brahme, A. (Ed.), Comprehensive Biomedical Physics. Elsevier, Oxford, pp. 193–220. URL: https://www.sciencedirect.com/science/article/pii/B9780444536327002094. dOI: 10.1016/B978-0-444-53632-7.00209-4.

Rigon, L., Besch, H.J., Arfelli, F., Menk, R.H., Heitner, G., Hartmute Plothow-Besch, 2003. A new DEI algorithm capable of investigating sub-pixel structures. J. Phys. D: Appl. Phys. 36, A107. URL: http://stacks.iop.org/0022-3727/36/i=10A/a=322, doi:10.1088/0022-3727/36/10A/322.

Snigirev, A., Snigireva, I., Kohn, V., Kuznetsov, S., Schelokov, I., 1995. On the possibilities of x-ray phase contrast microimaging by coherent high-energy synchrotron radiation. Review of Scientific Instruments 66, 5486–5492. URL: http://aip.scitation.org/doi/abs/10.1063/1.1146073, doi:10.1063/1.1146073.

Suortti, P., Thomlinson, W., 2003. Medical applications of synchrotron radiation. Physics in Medicine and Biology 48, R1–R35. doi:10.1088/0031-9155/48/13/201.

Teague, M.R., 1982. Irradiance moments: their propagation and use for unique retrieval of phase. J. Opt. Soc. Am., JOSA 72, 1199–1209. URL: https://www.osapublishing.org/abstract.cfm?uri=josa-72-9-1199, doi:10.1364/JOSA.72.001199.

Turner, L.D., Dhal, B.B., Hayes, J.P., Mancuso, A.P., Nugent, K.A., Paterson, D., Scholten, R.E., Tran, C.Q., Peele, A.G., 2004. X-ray phase imaging: Demonstration of extended conditions with homogeneous objects. Opt. Express, OE 12, 2960–2965. URL: https://www.osapublishing.org/abstract.cfm?uri=oe-12-13-2960, doi:10.1364/OPEX.12.002960.

Vittoria, F.A., Endrizzi, M., Diemoz, P.C., Wagner, U.H., Rau, C., Robinson, I.K., Olivo, A., 2014. Virtual edge illumination and one dimensional beam tracking for absorption, refraction, and scattering retrieval. Appl. Phys. Lett.

104, 134102. URL: http://aip.scitation.org/doi/abs/10.1063/1.4870528, doi:10.1063/1.4870528.

Vittoria, F.A., Kallon, G.K.N., Basta, D., Diemoz, P.C., Robinson, I.K., Olivo, A., Endrizzi, M., 2015. Beam tracking approach for single–shot retrieval of absorption, refraction, and dark–field signals with laboratory x–ray sources. Appl. Phys. Lett. 106, 224102. URL: http://aip.scitation.org/doi/abs/10.1063/1.4922189, doi:10.1063/1.4922189.

Weitkamp, T., Diaz, A., David, C., Pfeiffer, F., Stampanoni, M., Cloetens, P., Ziegler, E., 2005. X-ray phase imaging with a grating interferometer. Opt. Express, OE 13, 6296–6304. URL: https://www.osapublishing.org/abstract.cfm?uri=oe-13-16-6296, doi:10.1364/OPEX.13.006296.

Wilkins, S., Gureyev, T., Gao, D., Pogany, A., Stevenson, A., 1996. Phase-contrast imaging using polychromatic hard X-rays. Nature 384, 335–338. doi:10.1038/384335a0.

Wilkins, S., Nesterets, Y., Gureyev, T., Mayo, S., Pogany, A., Stevenson, A., 2014. On the evolution and relative merits of hard X-ray phase-contrast imaging methods. Philosophical Transactions of the Royal Society A: Mathematical, Physical and Engineering Sciences 372. doi:10.1098/rsta.2013.0021.

Zachariasen, W.H., 1945. Theory of X-ray Diffraction in Crystals [by] William H. Zachariasen ... J. Wiley & sons, Incorporated. Google-Books-ID: W3bdAQAACAAJ.

Zhou, S.A., Brahme, A., 2008. Development of phase-contrast X-ray imaging techniques and potential medical applications. Phys Med 24, 129–148. doi:10.1016/j.ejmp.2008.05.006.

# 3
# Experimental setups

## Contents

## 3.1 *Introduction*

In field of medical diagnostics and for research purposes, x-ray radiation is conventionally produced by x-ray tubes. Their basic principle was discovered by Röntgen in 1895, a current is applied to a metal cathode producing free electrons, which are then accelerated by an electric field using high voltage towards a metal anode. The collision with the target (anode) forces the electron to suddenly decelerate releasing energy. The majority of this energy (95%) is converted in heat and the other 5% in x-rays, this effect is known as *Brehmsstrahlung*. At the same time, if the incoming electrons have sufficiently high energy, they can be able to remove an electron from an inner shell of the anode (ionisation process). The resulting vacancy, can then be filled by an electron dropping down from a higher state, emitting x-ray photons with a precise energy determined by the difference between the energy level of the two states. These x-rays are known as *characteristic x-rays*. The x-ray spectrum, produced by conventional tubes is determined by its characteristics, such as the anode material, the voltage applied and the filters eventually placed in the x-ray beam. It may be worth to underline that, due to the broad energy spectrum and the rather big focal spot size, conventional x-ray tubes have a rather poor coherence both temporally and spatially. Alternatives micro-focus x-ray sources have been developed, where the anode is replaced by a jet of liquid metal, thus achieving a brilliance one order of magnitude higher than a solid anode x-ray tube (Tuohimaa et al. (2007)), even at high energies (Larsson et al. (2011)). Other types of coherent sources use an electron beam, of about 10 $MeV$, directed on a metal wire target. In this case, the spectrum of the energy is quite broad and poorly coherent, but is characterised by a high intensity and high degree of spatial coherence, thus it could be suitable for phase-contrast biomedical imaging (Hirai et al. (2006)). Another area recently spreading, concerns the development of inverse Compton scattering sources (Carroll et al. (2003)). They are based on a relativistic collision between a high-power laser pulse and an electron beam accelerated to energies of a few megaelectron volts. The result of this collision, is the generation of x-ray with tuneable energy and a narrow bandwidth in a small-angle cone beam

geometry. The beam can achieve a sufficiently high degree of lateral coherence and a sufficient flux for biomedical imaging applications (Bech et al. (2009); Yamada et al. (2009)). Despite this expanding interest in the development of new alternative x-ray sources, synchrotron x-ray sources are still considered as the gold standard for x-ray production, mainly because of their capability of generating very intense x-ray beams with an extremely high spatial coherence. In this chapter, the working principles of a synchrotron will be described, highlighting the advantages of the use of synchrotron radiation for phase-contrast imaging. Two medical imaging beamlines, will be also described, as they have been used for the experimental part of this thesis.

## 3.2 Synchrotron x-ray sources

A synchrotron is composed of a large storage ring, with a diameter in the range of several hundred meter. In such a ring circulates an electron beam with an energy of few giga-electron volts. A pre-acceleration is performed, using disc-loaded wave guides, (Brefeld and Gurtler (1991)) in a linear accelerator (LINAC), electrons are then injected into a first synchrotron accelerator (booster), where their energy is "ramped" to the final energy. In the first and second generation SR machines, the booster was made to operate as a synchrotron and as a storage ring at the same time. In the new generation of SR facilities, electrons are transferred to a second ring, called "storage ring", where the electron energy is kept constant (see Fig. 3.1). To accelerate the electrons in the booster, radiofrequency cavities are used.

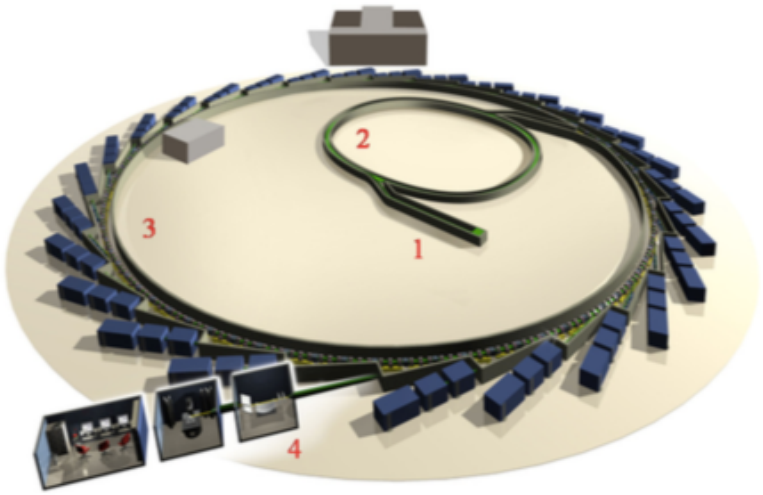


**Figure 3.1:** Schematic representation of a third-generation synchrotron radiation facility. 1) Linear accelerator (LINAC), 2) acceleration ring (Booster), 3) storage ring and 4) beamline.

Other important components are the quadrupole and sextupole magnets; suitably combined, they provide focusing forces that keep the electron-beam transverse dimensions small. Straight sections are also present, with elements for the injection

of the electrons from an accelerator to the other (LINAC-to-booster, booster-to-storage ring). The electrons run in ultra-high vacuum (less than 10-8 $mbar$) in order to minimise the probability of collisions with residual gas. A closed, continuous high-vacuum chamber extends through the various booster and storage ring elements. As a matter of fact, the ring is a polygon where the sides are linked by bending magnets (BM) deviating the beam towards the next straight section. It is exactly in correspondence to these deviations, that electrons emit electromagnetic radiation, known as synchrotron radiation (SR), which is then carried by transportation lines called beamlines. The radiation is emitted tangentially to the curved trajectory of the accelerated particles and occurs in a narrow cone with a natural opening angle of $1/\gamma$, with $\gamma$ equal to $\gamma = 1/\sqrt{1-\nu^2/c^2}$, where is the electrons speed. Usually, in synchrotron facilities, electrons are produced in bunches of $10^{11}$ particles by means of an electron gun with a frequency up to 10 $Hz$. It is possible to originate beamline in the straight sections as well, placing insertion devices (ID), such as wigglers or undulators, that are able to wiggle (or undulate) the electron beam generating a highly intense electromagnetic radiation. They consist of a sequence of dipole magnets of alternating polarities: the magnetic fields force the electron to oscillate around a straight-line trajectory and the cones of light emitted at each bend superimpose.

- For undulators, the electron beam deflection is less than $1/\gamma$, so that the beams emitted by individual poles can interfere coherently. This leads to a spectrum with strong peaks at a specific energy and its harmonics.

- When using wigglers, the total divergence is much larger than the natural opening angle of the radiation and no more interference occurs. The final beam emitted by the device is the incoherent sum of the beams emitted at each pole, and the x-ray spectrum has a continuous distribution.

Every beamline is, usually, built and equipped for determined scientific purposes and can handle specific experiments, taking into account the photon flux, beam dimension, bandwidth, focus and collimation of the x-ray. The experimental hutches

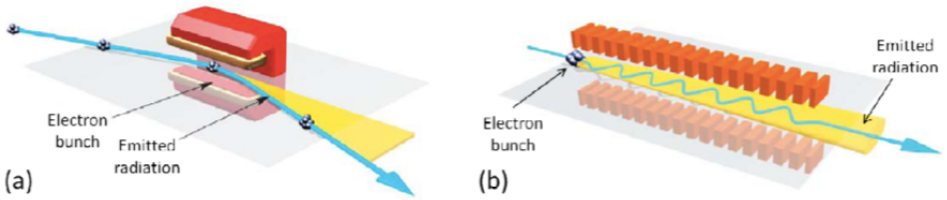


**Figure 3.2:** Schematic representation of a bending magnet (a) and of an insertion device (b).

can be located from tens to some hundreds of meters away from the source. Most of the beamlines, especially the imaging ones, make use of a monochromator crystal, a device meant to select a specific energy with a narrow bandwidth obtaining a virtually mono-energetic and tuneable x-ray source. Typical values are $\Delta\lambda/\lambda \approx 10^3 - 10^5$, furthermore, the produced beam has a high degree of both longitudinal and lateral coherence, the source size is usually of the order of 100 $mm$ and the distance between the source and the sample can exceed 100 $m$. With particular concern to biomedical imaging application, thanks to the high brilliance of the source, the photon flux is sufficiently high to allows acquisition with very short exposure time. Table 3.1). summarises the beamlines that are totally or partially dedicated to biomedical application world-wide.

**Table 3.1:** Beamlines for medical imaging and biomedical applications

| Beamline | Facility | Citation |
|---|---|---|
| X15A | NSLS (*Brookhaven*, NY, USA) | Zhong et al. (2000) |
| SYRMEP | Elettra (*Trieste*, NY, USA) | Tromba et al. (2010) |
| ID17 | ESRF (*Grenoble*, France) | Bravin (2007) |
| ID19 | ESRF (*Grenoble*, France) | Weitkamp et al. (2010) |
| BL14C | PF-KEK (*Tsukuba*, Japan) | Yoneyama et al. (2004) |
| BL20B2 | Spring8 (*Hyogo*, Japan) | Goto et al. (2001) |
| BL20XU | Spring8 (*Hyogo*, Japan) | Suzuki et al. (2004) |
| TOMCAT | SLS-PSI (*Villigen*, Switzerland) | Stampanoni et al. (2006) |
| BMIT-05B1-1 | CLS (*Saskatoon*, Canada) | Wysokinski et al. (2007) |
| BMIT-05ID-2 | CLS (*Saskatoon*, Canada) | Wysokinski et al. (2013) |
| IMBL | Australian Synchrotron (*Melbourne*, Australia) | Hausermann et al. (2010) |
| BL10W1 | SSRF (*Shanghai*, China) | Xie et al. (2013) |
| I13L | Diamond (*Oxfordshire*, UK) | Pešić et al. (2013) |

### 3.2.1 Advantages of synchrotron sources for phase-contrast techniques

One important difference, between conventional x-ray tube and SR sources is the geometry of the imaging system (see Fig. 3.3). The radiation emitted by the x-ray tube has a broad angle and, usually, the sample is placed close to the source. The magnification can be changed $M = (L + D)/L$, either the distance between focal spot and sample (L) or the sample-to-detector one (D).

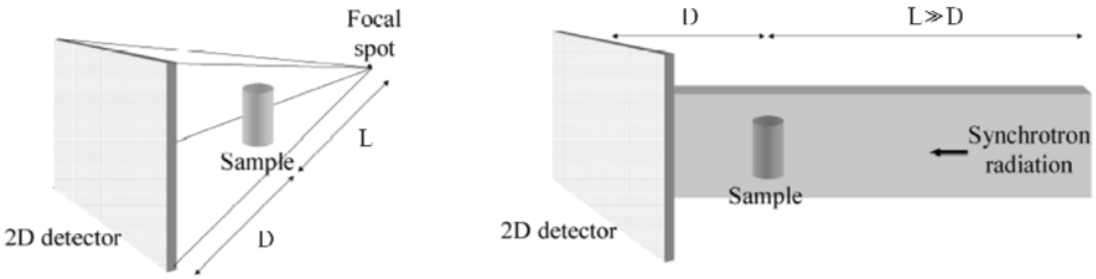


**Figure 3.3:** Schematic representation of the different geometries of irradiation for X-ray tubes (on the left side) and SR imaging (on the right side)

SR sources produce a beam with a small angular opening, for this reason it is possible to place the sample at large distances from the source, keeping a high incident intensity. This feature, together with the small size of the source, is fundamental to reach the degree of spatial coherence requested for the application of most of the phase-contrast techniques described in Chapter 2, and, in addition, provide a good geometrical resolution, $R = S \cdot D/L$. Moreover, the SR beam is almost parallel at the sample position, this property reduces the typical penumbra of the x-ray tubes and allows the application, for example, of the ABI technique that is characterised by a very high angular selectivity of the monochromator and the analyser crystal.

## 3.3 SYRMEP beamline

SYRMEP is the acronym of Synchrotron Radiation for Medical Physics and it is one of the bending magnet of Elettra light source. Thanks to the horizontal

acceptance covered by the front-end port that is 7 $mrad$, the beamline is able to provide, at a distance of about 30 $m$ from the source, a mono-energetic laminar beam with an area of $(210 \times 5)$ $mm$ at 20 $keV$. Depending on the experimental setup, a white beam can be used or a monochromator may be placed between the source and the sample. In the applications of this thesis only the monochromatic configuration depicted in Fig. 3.4 was used. The monochromator is a double Si(1,1,1) crystal, working in Bragg configuration that can select energies from 8.5 to 40 $keV$, with an energy resolution of $10^{-3}$.

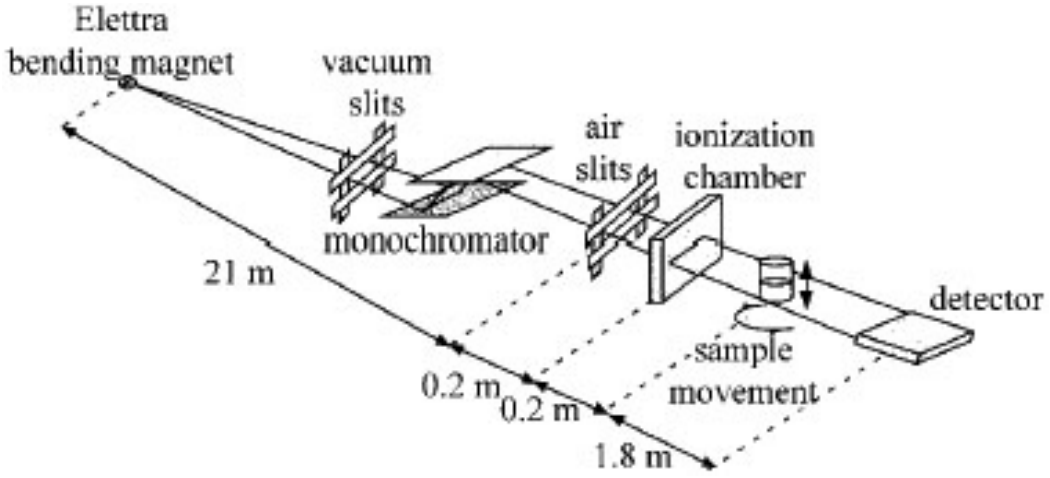


**Figure 3.4:** Schematic view of the SYRMEP beamline in monochromatic beam configuration

There are three experimental stations: the first one is the white-beam station where the beam is intercepted upstream the monochromator; in the second one the sample is located (after the monochromator) at 23 $m$ from the source and the detector is mounted on a 2 $m$ long rail, so that it can be placed at difference distances, allowing the use of the PBI phase-contrast technique. The sample stage is equipped with translational and high-resolution rotational motors adequate for micro-CT applications (Fig. 3.5a). The third station, which from now on will be called *patient hutch*, is the one used for the first research protocol on phase-contrast

clinical mammography. It is equipped with an especially designed support, (similar to a bed with an opening consistent with chest anatomy, allowing the positioning of the breast) where the patient is supposed to lay prone (see Fig. 3.5b). The movement system is equipped with three motion stages: horizontal for positioning, vertical and rotational, along an axis perpendicular to the beam, for scanning.

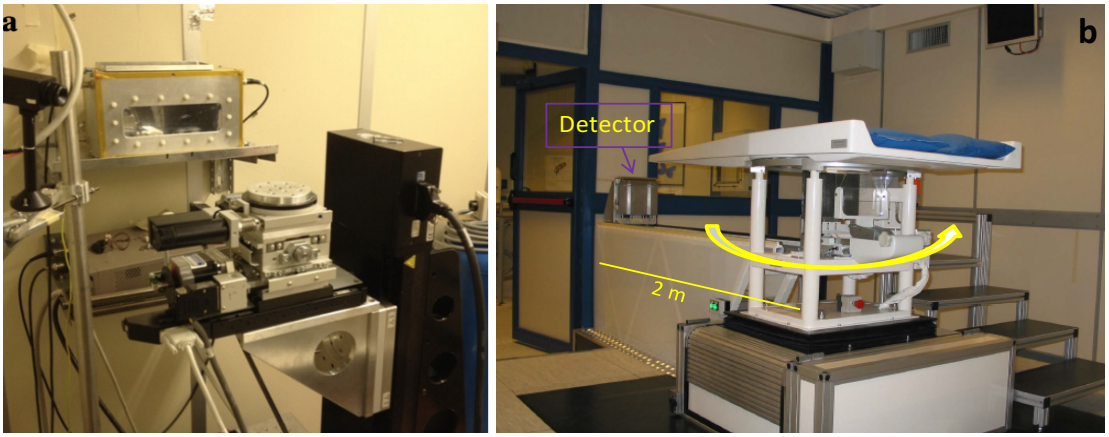


**Figure 3.5:** The experimental hutches of the SYRMEP beamline: a) first station with rotational sample holder and ionisation chamber; b) patient hutch with bed and detector holder.

Various detectors with different field of views and spatial resolutions are available, depending on them the pixel size goes from 1.2 $\mu m$, in white mode, to 100 $\mu m$ in monochromatic mode and for large size samples (Tromba et al. (2010)).

## 3.4 IMBL beamline

The Imaging and Medical Beamline is placed on an insertion device of the Australian Synchrotron. Along the beamline there are 6 radiation enclosures, three optics and three experimental one. All end-stations are designed to accept the full x-ray spectrum from a superconducting wiggler device. Four of the enclosures are situated in the main building, while the third pair are placed in a *Satellite Building* that is supplied with photons by a beamline extension through the wall of the storage ring building (Fig. 3.6). The experimental hutch in the *Satellite Building* is serviced with a beam of radiation which has propagated 136 $m$ from the source to the sample

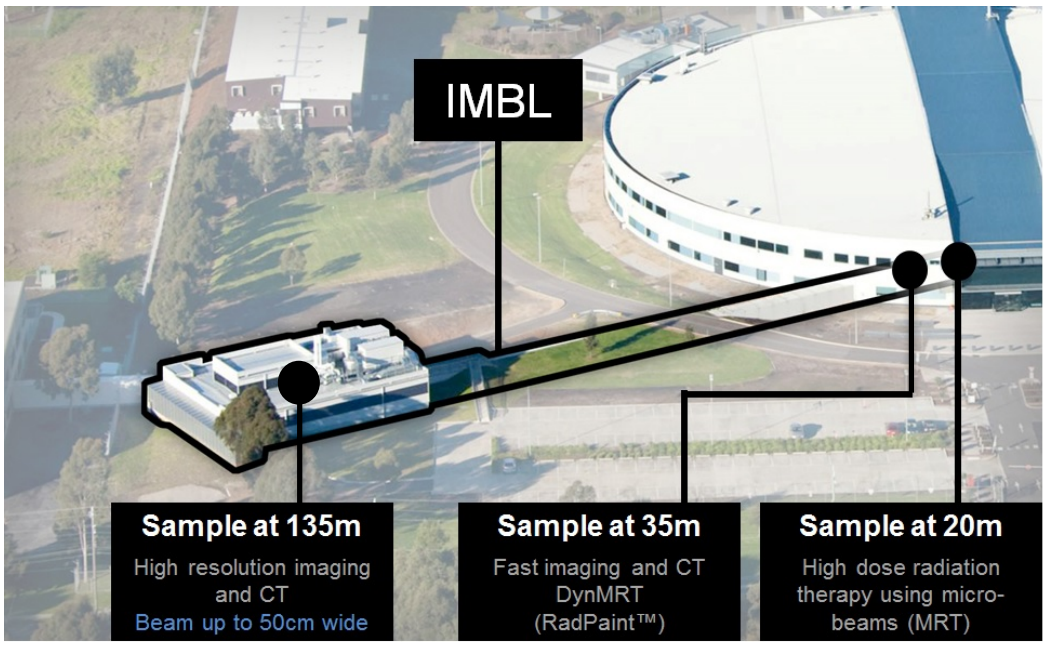


**Figure 3.6:** View of the Australian Synchrotron and the Satellite Building hosting the IMBL. Distances from the source to the samples for the different experimental hutches are shown.

position. The beam therefore has a high degree of phase coherence and a relatively large width. The beam size at 40 $keV$ has an area of $600 \times 50$ $mm$. One side of the Satellite Building is already designed to host human patient, with a reception desk and waiting room, as well as examination and preparation rooms. The other side, is an area dedicated to non-human biomedical imaging, equipped with short term animal handling, preparation and recovery rooms.

The research activity of the IMBL is focused on two main areas: radiation therapy and x-ray imaging, for both of them there is a dedicatedly designed experimental hutch. In the first one, an intense beam is available, able to deliver the high dose required for some of the radiotherapy applications such as micro beam radiation therapy (Blattmann et al. (2005)). A bright monochromatic beam is also available in this hutch derived from a double Laue monochromator situated in one of the optics hutch. In the same station, monochromatic radiotherapy research such as photon activation therapy (PAT) (Corde et al. (2004)) and stereotactic radiation therapy (SSRT) (Jost et al. (2009)) is being carried out. In the imaging hutch, the

one used for the purposes of this thesis, different important programs on both small and large animals radiography have took place. The hutch is well suited for human chest imaging, and it is likely to become the primary clinical facility on the IMBL for breast tomography and other scientific cases (Hausermann et al. (2010)).

# References

Bech, M., Bunk, O., David, C., Ruth, R., Rifkin, J., Loewen, R., Feidenhans'l, R., Pfeiffer, F., 2009. Hard X-ray phase-contrast imaging with the Compact Light Source based on inverse Compton X-rays. J Synchrotron Rad, J Synchrotron Radiat 16, 43–47. URL: http://scripts.iucr.org/cgi-bin/paper?kt5019, doi:10.1107/S090904950803464X.

Blattmann, H., Gebbers, J.O., Bräuer-Krisch, E., Bravin, A., Le Duc, G., Burkard, W., Di Michiel, M., Djonov, V., Slatkin, D.N., Stepanek, J., Laissue, J.A., 2005. Applications of synchrotron X-rays to radiotherapy. Nuclear Instruments and Methods in Physics Research Section A: Accelerators, Spectrometers, Detectors and Associated Equipment 548, 17–22. URL: http://www.sciencedirect.com/science/article/pii/S0168900205006418, doi:10.1016/j.nima.2005.03.060.

Bravin, A., 2007. THE BIOMEDICAL PROGRAMS AT THE ID17 BEAMLINE OF THE EUROPEAN SYNCHROTRON RADIATION FACILITY, in: Brilliant Light in Life and Material Sciences. Springer, Dordrecht. NATO Security through Science Series, pp. 225–239. URL: https://link.springer.com/chapter/10.1007/978-1-4020-5724-3_21. dOI: 10.1007/978-1-4020-5724-3_21.

Brefeld, W., Gurtler, P., 1991. Superconducting Magnet Systems, in: Handbook on Synchrotron Radiation. springer, berlin, heidelberg ed.. volume 1.

Carroll, F.E., Mendenhall, M.H., Traeger, R.H., Brau, C., Waters, J.W., 2003. Pulsed Tunable Monochromatic X-Ray Beams from a Compact Source: New Opportunities. American Journal of Roentgenology 181, 1197–1202. URL: http://www.ajronline.org/doi/abs/10.2214/ajr.181.5.1811197, doi:10.2214/ajr.181.5.1811197.

Corde, S., Joubert, A., Adam, J.F., Charvet, A.M., Bas, J.F.L., Estève, F., Elleaume, H., Balosso, J., 2004. Synchrotron radiation-based experimental determination

of the optimal energy for cell radiotoxicity enhancement following photoelectric effect on stable iodinated compounds. British Journal of Cancer 91, 544. URL: https://www.nature.com/articles/6601951, doi:10.1038/sj.bjc.6601951.

Goto, S., Takeshita, K., Suzuki, Y., Ohashi, H., Asano, Y., Kimura, H., Matsushita, T., Yagi, N., Isshiki, M., Yamazaki, H., Yoneda, Y., Umetani, K., Ishikawa, T., 2001. Construction and commissioning of a 215-m-long beamline at SPring-8. Nuclear Instruments and Methods in Physics Research Section A: Accelerators, Spectrometers, Detectors and Associated Equipment 467-468, 682–685. URL: http://www.sciencedirect.com/science/article/pii/S0168900201004454, doi:10.1016/S0168-9002(01)00445-4.

Hausermann, D., Hall, C., Maksimenko, A., Campbell, C., 2010. The Imaging and Medical Beam Line at the Australian Synchrotron. AIP Conference Proceedings 1266, 3–9. URL: http://aip.scitation.org/doi/abs/10.1063/1.3478195, doi:10.1063/1.3478195.

Hirai, T., Yamada, H., Sasaki, M., Hasegawa, D., Morita, M., Oda, Y., Takaku, J., Hanashima, T., Nitta, N., Takahashi, M., Murata, K., 2006. Refraction contrast 11×-magnified X-ray imaging of large objects by MIRRORCLE-type table-top synchrotron. J Synchrotron Rad, J Synchrotron Radiat 13, 397–402. URL: http://scripts.iucr.org/cgi-bin/paper?ot5565, doi:10.1107/S0909049506027026.

Jost, G., Mensing, T., Golfier, S., Lawaczeck, R., Pietsch, H., Hütter, J., Cibik, L., Gerlach, M., Krumrey, M., Fratzscher, D., Arkadiev, V., Wedell, R., Haschke, M., Langhoff, N., Wust, P., Lüdemann, L., 2009. Photoelectric-enhanced radiation therapy with quasi-monochromatic computed tomography. Med. Phys. 36, 2107–2117. URL: http://onlinelibrary.wiley.com/doi/10.1118/1.3125137/abstract, doi:10.1118/1.3125137.

Larsson, D.H., Takman, P.a.C., Lundström, U., Burvall, A., Hertz, H.M., 2011. A 24 keV liquid-metal-jet x-ray source for biomedical applications. Review of

Scientific Instruments 82, 123701. URL: http://aip.scitation.org/doi/abs/10.1063/1.3664870, doi:10.1063/1.3664870.

Pešić, Z.D., Fanis, A.D., Wagner, U., Rau, C., 2013. Experimental stations at I13 beamline at Diamond Light Source. J. Phys.: Conf. Ser. 425, 182003. URL: http://stacks.iop.org/1742-6596/425/i=18/a=182003, doi:10.1088/1742-6596/425/18/182003.

Stampanoni, M., Groso, A., Isenegger, A., Mikuljan, G., Chen, Q., Bertrand, A., Henein, S., Betemps, R., Frommherz, U., Böhler, P., Meister, D., Lange, M., Abela, R., 2006. Trends in synchrotron-based tomographic imaging: the SLS experience, International Society for Optics and Photonics. p. 63180M. URL: https://www.spiedigitallibrary.org/conference-proceedings-of-spie/6318/63180M/Trends-in-synchrotron-based-tomographic-imaging-the-SLS-experience/10.1117/12.679497.short, doi:10.1117/12.679497.

Suzuki, Y., Uesugi, K., Takimoto, N., Fukui, T., Aoyama, K., Takeuchi, A., Takano, H., Yagi, N., Mochizuki, T., Goto, S., Takeshita, K., Takahashi, S., Ohashi, H., Furukawa, Y., Ohata, T., Matsushita, T., Ishizawa, Y., Yamazaki, H., Yabashi, M., Tanaka, T., Kitamura, H., Ishikawa, T., 2004. Construction and Commissioning of A 248 m-long Beamline with X-ray Undulator Light Source. AIP Conference Proceedings 705, 344–347. URL: http://aip.scitation.org/doi/abs/10.1063/1.1757804, doi:10.1063/1.1757804.

Tromba, G., Longo, R., Abrami, A., Arfelli, F., Astolfo, A., Bregant, P., Brun, F., Casarin, K., Chenda, V., Dreossi, D., Hola, M., Kaiser, J., Mancini, L., Menk, R.H., Quai, E., Quaia, E., Rigon, L., Rokvic, T., Sodini, N., Sanabor, D., Schultke, E., Tonutti, M., Vascotto, A., Zanconati, F., Cova, M., Castelli, E., 2010. The SYRMEP Beamline of Elettra: Clinical Mammography and Biomedical Applications. AIP Conference Proceedings 1266, 18–23. URL: http://aip.scitation.org/doi/abs/10.1063/1.3478190, doi:10.1063/1.3478190.

Tuohimaa, T., Otendal, M., Hertz, H.M., 2007. Phase-contrast x-ray imaging with a liquid-metal-jet-anode microfocus source. Applied Physics Letters 91, 074104. URL: http://adsabs.harvard.edu/abs/2007ApPhL..91g4104T, doi:10.1063/1.2769760.

Weitkamp, T., Tafforeau, P., Boller, E., Cloetens, P., Valade, J., Bernard, P., Peyrin, F., Ludwig, W., Helfen, L., Baruchel, J., 2010. Status and evolution of the ESRF beamline ID19. AIP Conference Proceedings 1221, 33–38. URL: http://aip.scitation.org/doi/abs/10.1063/1.3399253, doi:10.1063/1.3399253.

Wysokinski, T.W., Chapman, D., Adams, G., Renier, M., Suortti, P., Thomlinson, W., 2007. Beamlines of the biomedical imaging and therapy facility at the Canadian light source—Part 1. Nuclear Instruments and Methods in Physics Research Section A: Accelerators, Spectrometers, Detectors and Associated Equipment 582, 73–76. URL: http://www.sciencedirect.com/science/article/pii/S0168900207017482, doi:10.1016/j.nima.2007.08.087.

Wysokinski, T.W., Chapman, D., Adams, G., Renier, M., Suortti, P., Thomlinson, W., 2013. Beamlines of the Biomedical Imaging and Therapy Facility at the Canadian Light Source - Part 2. J. Phys.: Conf. Ser. 425, 072013. URL: http://stacks.iop.org/1742-6596/425/i=7/a=072013, doi:10.1088/1742-6596/425/7/072013.

Xie, H., Deng, B., Du, G., Fu, Y., He, Y., Guo, H., Peng, G., Xue, Y., Zhou, G., Ren, Y., Wang, Y., Chen, R., Tong, Y., Xiao, T., 2013. X-ray biomedical imaging beamline at SSRF. J. Inst. 8, C08003. URL: http://stacks.iop.org/1748-0221/8/i=08/a=C08003, doi:10.1088/1748-0221/8/08/C08003.

Yamada, K., Kuroda, R., Toyakawa, H., Ikeura-Sekiguchi, H., Yasumoto, M., Koike, M., Sakai, F., Mori, K., Mori, H., Fukuyama, N., Sato, E., 2009. A trial for fine and low-dose imaging of biological specimens using quasi-monochromatic laser-Compton X-rays. Nuclear Instruments and Methods in Physics Research Section A: Accelerators, Spectrometers, Detectors and Associated Equipment

608, S7–S10. URL: http://www.sciencedirect.com/science/article/pii/S0168900209009553, doi:10.1016/j.nima.2009.05.157.

Yoneyama, A., Takeda, T., Tsuchiya, Y., Wu, J., Thet-Thet-Lwin, Koizumi, A., Hyodo, K., Itai, Y., 2004. A phase-contrast X-ray imaging system—with a 60×30mm field of view—based on a skew-symmetric two-crystal X-ray interferometer. Nuclear Instruments and Methods in Physics Research Section A: Accelerators, Spectrometers, Detectors and Associated Equipment 523, 217–222. URL: http://www.sciencedirect.com/science/article/pii/S0168900203034028, doi:10.1016/j.nima.2003.12.008.

Zhong, Z., Thomlinson, W., Chapman, D., Sayers, D., 2000. Implementation of diffraction-enhanced imaging experiments: at the NSLS and APS. Nuclear Instruments and Methods in Physics Research Section A: Accelerators, Spectrometers, Detectors and Associated Equipment 450, 556–567. URL: http://www.sciencedirect.com/science/article/pii/S0168900200003089, doi:10.1016/S0168-9002(00)00308-9.

# 4
# Image processing methods

## Contents

## 4.1 *Introduction*

In a very simplified way, it is possible to describe the working principle of Computed Tomography (CT), saying that a series of angular projection data are gathered together and processed by a tomographic reconstruction algorithm, producing an image of the section of the sample, called "slice". The obtained image contains, as described in chapter 2, information about the internal 3D distribution of the refractive index, namely about the absorption and with a suitable phase retrieval method, about the phase. The reconstruction of the CT images can be performed by means of several algorithms based on the analytical Fourier-based method or on iterative methods (algebraic and analytical). The most used one, in conventional medical CT applications, is the Filtered Back Projection (FBP) that is an analytical method. The following sections address the mathematical framework that enables such a reconstruction, followed by an assessment of typical artefacts that may occur and limiting the attention to the use of Synchrotron Radiation. All the basic steps of the image processing, such as flat fielding normalisation and ring removal algorithm, will be described as they have been applied to obtain all the images used in this thesis work. Furthermore, the software solutions adopted by the SYRMEP beamline of the Elettra synchrotron, will be described, as its debugging and testing phases have been part of the work carried out during the PhD program. The last part of the chapter will be briefly dedicated to the description of the segmentation process, as it is the fundamental step to perform the three-dimensional rendering that will be showed in the next chapter.

## 4.2 Mathematical background

### 4.2.1 Radon transform

Johann Radon in 1917 derived the fundamental mathematics of reconstructing a function, when its integrals values are given (Radon (1917)). To describe it, one can consider the situation displayed in Fig. 4.1:

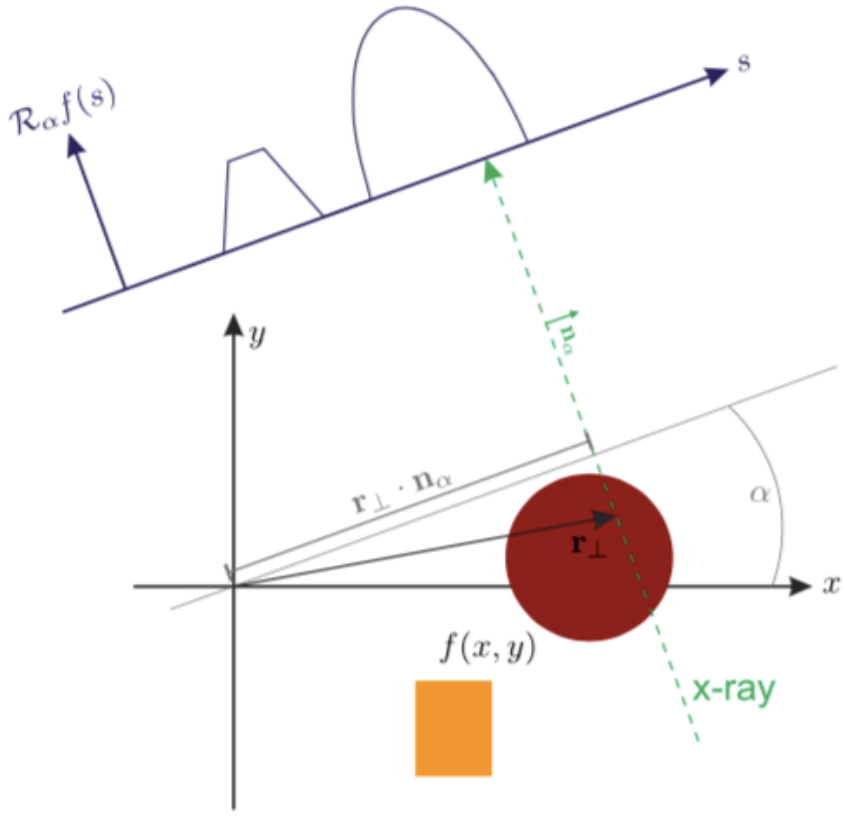


**Figure 4.1:** Schematic illustration of the Radon transform. A 2D object described by a function $f(x, y)$ is illuminated by parallel x-rays (dashed green line) forming an angle $\alpha$ with the y-axis. After interaction with the object, the projected values form a one-dimensional profile $R_\alpha f(s)$ in dependence on the position s along a line, perpendicular to the projection direction.

There is a function (x,y), that represent an object by mapping each point $\mathbf{r}_\perp \in \mathbb{R}^2$ to a value $g \in \mathbb{R}$. The chosen object, is made of two regions of constant values: a sphere with $f(x, y) = 1$ and a rectangle with $f(x, y) = 0.8$, represented with two different colours. The x-ray beam, illustrated as a dashed green arrow,

illuminating the object with a certain angle $\alpha$, is subject to attenuation and phase shift. Behind the object, a projection, given by the accumulation over the whole distance of all the values corresponding to each point (x,y), can be measured. The calculation, for a given angle, is made possible by mean of the *2D Radon Transform* $R_\alpha f$, mathematically expressed as follows (Buzug (2008)):

$$R_\alpha f(s) = \int_{\mathbb{R}^2} f(r_\perp)\delta(r_\perp \cdot n_\alpha - s)\mathrm{d}\mathbf{r}_\perp \tag{4.1}$$

where $r_\perp = (x, y)^T$ is the vector defining the coordinate in the image plane that is orthogonal to the rotation axis, $s$ is the coordinate of the projected profile, $\delta(s - s_0)$ is the one-dimensional Dirac delta distribution and $n_\alpha = (\cos\alpha, \sin\alpha)^T$ is the normal vector perpendicular to the projection direction. The coordinate vector $r_\perp$, doing the scalar product $\mathbf{r}_\perp \cdot \mathbf{n}_\alpha$ is projected to a line forming the angle $\alpha$ with the x-axis (grey line in Fig. 4.1). Accordingly, the argument of the delta-distribution goes to zero for points forming a straight line of angle $\alpha$ with the y-axis with distance $s$ to the origin. In such a way, only points on the direction of the x-ray propagation, contribute to the computing of $R_\alpha f(s)$, so the two-dimensional integral in eq. 4.1 is actually a one-dimensional integral over this line. It has to be noticed that, with the definition of the Radon transform given by eq. 4.1, the generalisation of the Radon transform to higher dimensions $n$ is easily possible (Natterer (2001)). For example, in the case of the 3D radon transform as a function $R : \mathbb{R}^3 \to \mathbb{R}$, in which the integral is calculated over a plane instead of a line, the vector $\mathbf{n}_\alpha$ will become the normal vector of this plane. Taking into account the Radon transform of a single point at a certain distance from the origin, the 2D plot of all the projected values as a function of the angle, is a sine curve; such a data representation is the so-called *sinogram* (see Fig. 4.2).

For a given sinogram $p(\alpha, s) = p_\alpha(s) = R_\alpha f(s)$, it is possible to obtain a 2D image $f(x, y)$ from a set of 1D projections taken at different angles $\alpha$ by mean of an inverse Radon transform formally written as:

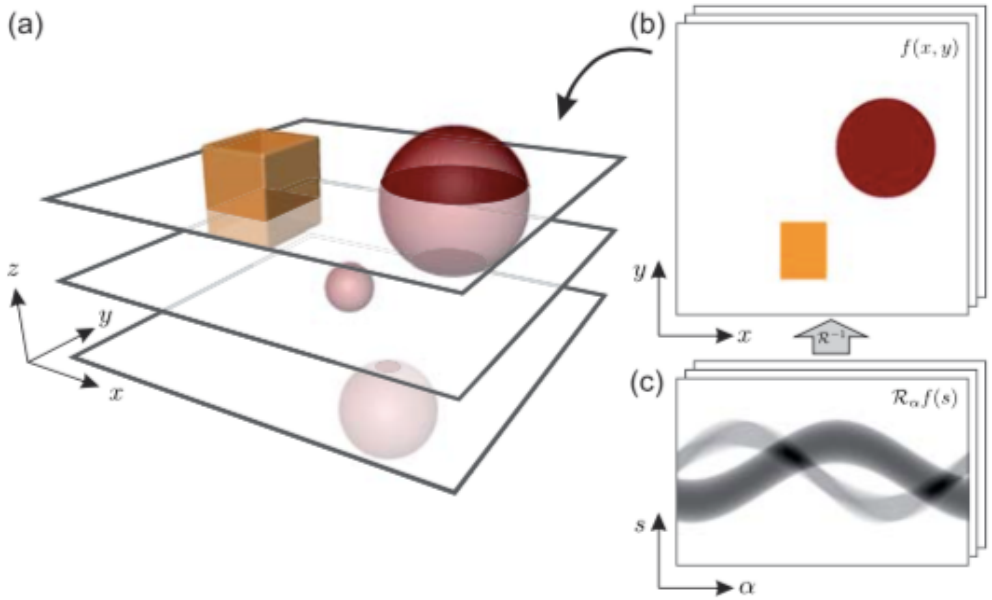


**Figure 4.2:** Illustration of the process from 2D slices to a 3D object. In a tomographic scan, each vertical position in a projection image ($z = const.$) forms (c) a *sinogram*, i.e., the projected profiles $R_\alpha f(s)$ plotted as a function of the projection angle $\alpha$. These can be inverted to obtain (b) a reconstructed slice $f(x, y)$ that subsequently can be virtually stacked to yield (a) a 3D volume.

$$f(x, y) = R^{-1}(p(\alpha, s)) \tag{4.2}$$

Thus, to obtain a 3D reconstruction of an entire object, all the collected $f(x, y)$ can be stacked in the z direction, yielding a 3D dataset $f(x, y, z)$, as shown in Fig. 4.2a.

### 4.2.2 Fourier slice Theorem

When taking into account the $n$-dimensional Radon transform $Rf(s)$, of a certain function $f(r)$ with $r \in \mathbb{R}^n$ and $\mathbf{n}$ normal vector of a hyperplane in $\mathbb{R}^{n-1}$, the Fourier transform with respect to $s$ is:

$$\mathcal{F}_s(Rf)(\rho) = \int_{\mathbb{R}} \left( e^{-2\pi i \rho s} \int_{\mathbb{R}^n} f(r)\delta(\mathbf{r} \cdot \mathbf{n} - s)\mathrm{d}\mathbf{r} \right) \mathrm{d}s = \int_{\mathbb{R}^n} e^{-2\pi i \rho \mathbf{r} \cdot \mathbf{n}} f(\mathbf{r})\mathrm{d}\mathbf{r} \tag{4.3}$$

where the order of integration has been changed and then integral over s have been carried out, eliminating the delta distribution. It is possible to define a coordinate vector in the reciprocal space as $\nu = \rho\mathbf{n}$, so that eq. 4.3 is proportional to the Fourier transform of the function $f(\mathbf{r})$ with respect to the coordinate vector $\mathbf{r}$:

$$\mathcal{F}_s(Rf)(\rho) = \int_{\mathbb{R}^n} e^{-2\pi i\boldsymbol{\nu}\cdot\mathbf{r}} f(\mathbf{r})\mathrm{d}\mathbf{r} = \mathcal{F}_{\mathbf{r}}(f)(\boldsymbol{\nu}) \tag{4.4}$$

This last equation is the *Fourier slice theorem*, which states that the one-dimensional Fourier transform of a projection $Rf(s)$ gives the values of the $n$-dimensional Fourier transform of the starting function $f(\mathbf{r})$ along a slice through the origin defined by $\nu = \rho\mathbf{n}$, and it proves that the Radon transform is invertible for every dimension $n$ (Natterer (2001)). For the 2D case (Fig. 4.3), the theorem will be:

$$\tilde{p}_\alpha(\rho) = \mathcal{F}_s(R_\alpha f)(\rho) = \tilde{f}(\rho\cos\alpha, r\sin\alpha) \tag{4.5}$$

using the typical notation for the Fourier transformed quantities. Accordingly, measuring all the angles, the Fourier space can be totally determined and the initial function $f(\mathbf{r})$ can be reconstructed by mean of the inverse Fourier transform. This method is known as *direct Fourier method*.

Looking at Fig. 4.3 it is noticeable that, when the function $f(\mathbf{r})$ is given at discrete points and a limited number of angles is used, the Fourier space won't be uniformly sampled, as the points won't be on a rectangular grid. For this reason, it is necessary to apply interpolation methods with the consequent introduction of artefacts in the real space. In addition, there is a difference in point density between low (near the origin) and large spatial frequencies, so that high resolution information in the image can be under-represented.

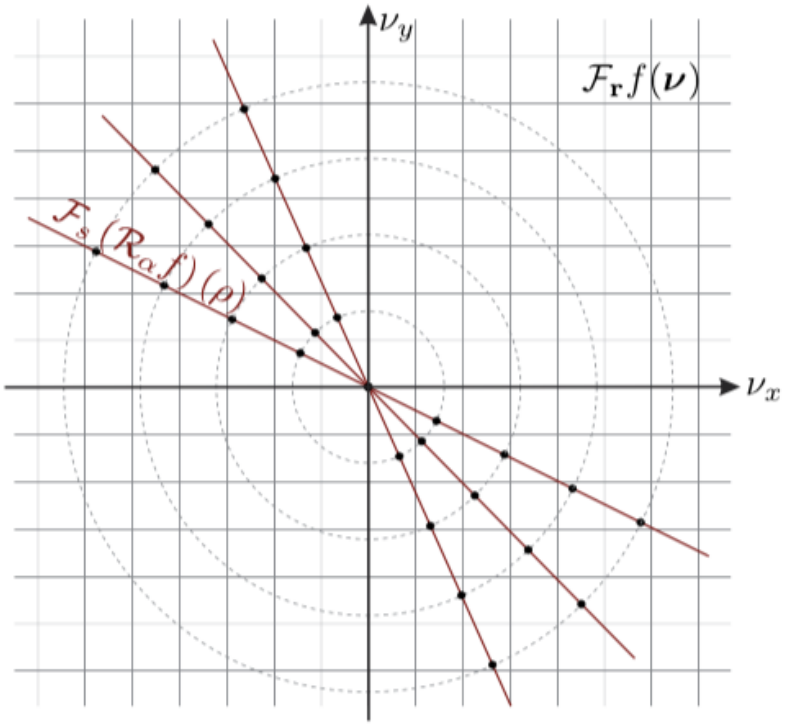


**Figure 4.3:** Illustration of the Fourier slice theorem for 2D case ($n = 2$): The 1D Fourier transform of a projection $R_\alpha f(s)$ corresponds to a slice (red line) in the 2D Fourier transform of the object $f(\boldsymbol{\nu})$. If the function is given at discrete points, indicated by the black dots, a sophisticated interpolation in Fourier space is necessary to avoid artefacts in the tomographic reconstruction.

### 4.2.3 The Filtered Back Projection

To overcome the drawbacks described in the previous paragraph, there is another widely-used approach (Buzug (2008)) that allows to weight the projections in the correct way, this method is called Filtered Back Projection (FBP) and it can be derived as follows:

$$f(\mathbf{r}_\perp) = \int_{\mathbb{R}^2} \tilde{f}(\boldsymbol{\nu}) e^{2\pi i \boldsymbol{\nu}\cdot\mathbf{r}_\perp} \mathrm{d}\boldsymbol{\nu} \tag{4.6}$$

where the function $f(\mathbf{r}_\perp)$ has been written as the inverse Fourier transform of $\tilde{f}$. Eq. 4.6 can be transformed in polar coordinates $(\nu_x, \nu_y)^T = (\rho\cos\alpha, \rho\sin\alpha)^T$, with the Jacobian $|\partial(\nu_x, \nu_y/\partial(\rho, \alpha)| = \rho$, becoming:

$$f(\mathbf{r}_\perp) = \int_0^{2\pi} \int_0^{\infty} \tilde{f}(\rho\cos\alpha, \rho\sin\alpha) e^{2\pi i \rho \mathbf{r}_\perp \cdot \mathbf{n}_\alpha} \cdot \rho \mathrm{d}\rho \mathrm{d}\alpha \tag{4.7}$$

with $\mathbf{r}_\perp \cdot \mathbf{n}_\alpha = (x\cos\alpha + y\sin\alpha)$. Using a symmetry relation for Fourier transform, the integral from 0 to $2\pi$ can be split in two and simplified as:

$$f(\mathbf{r}_\perp) = \int_0^{\pi} \int_{-\infty}^{\infty} \tilde{f}(\rho\cos\alpha, \rho\sin\alpha) e^{2\pi i \rho \mathbf{r}_\perp \cdot \mathbf{n}_\alpha} \cdot \rho \mathrm{d}|\rho|\mathrm{d}\alpha \tag{4.8}$$

Applying then, the Fourier slice theorem, to replace the function $\tilde{f}$ with its projections $\tilde{p}$, it becomes:

$$f(\mathbf{r}_\perp) = \int_0^{\pi} \int_{-\infty}^{\infty} \tilde{p}_\alpha(\rho) e^{2\pi i \rho \mathbf{r}_\perp \cdot \mathbf{n}_\alpha} \cdot |\rho| \mathrm{d}\rho \mathrm{d}\alpha \tag{4.9}$$

To comment the result obtained in eq. 4.9 it is essential to give some more definitions, i.e.:

- *Partial back projection* (for a given 1D projection $p_\alpha(s)$):

$$(R_\alpha^\sharp p_\alpha)(r) = p_\alpha(r \cdot n_\alpha) = p_\alpha(x\cos\alpha + y\sin\alpha) \tag{4.10}$$

  where the values of $p(s)$ are distributed in a 2D space, so that each point gets the value, given in the projection at coordinate $s$, where the point $r$ would be projected to with the Radon transform.

- *Back projection* of a set of projections $p_\alpha(s)$

$$(R_\alpha^\sharp p_\alpha)(r) = \int_0^{\pi} p_\alpha(\mathbf{r} \cdot \mathbf{n}_\alpha) \mathrm{d}\alpha \tag{4.11}$$

  which performs the partial back projection for every angle $\alpha$.

- *Filtered projection* (applying a filter to the projection $p_\alpha$ in Fourier space)

$$p_\alpha^F(s) = \mathcal{F}^{-1}\left(\tilde{h}(\rho)\tilde{p}(\rho)\right) = \int_{-\infty}^{\infty} e^{2\pi i\rho s}\tilde{h}(\rho)\tilde{p}_\alpha(\rho)\mathrm{d}\rho \tag{4.12}$$

  with a filter kernel $\tilde{h}(\rho)$.

Now, going back to eq. 4.9, it can be re-written using the given filtered projection with the kernel $\tilde{h}(\rho) = |\rho|$, yielding to:

$$f(r) = \int_0^\pi = p_\alpha^F(\mathbf{r}\cdot\mathbf{n}_\alpha)\mathrm{d}\alpha \tag{4.13}$$

which is the so-called *Filtered Back Projection*. The reconstruction could also be written as:

$$f(r) = R^\sharp\left(p_\alpha^F(s)\right) = R^\sharp((R_\alpha f)\otimes h)(r) \tag{4.14}$$

with $h(s) = \mathcal{F}^{-1}(\tilde{h}(q))$. The filter $\tilde{h}(q) = |q|$, is known as the Ram-Lak filter (Ramachandran and Lakshminarayanan (1971)), that acts as a high pass filter on the projections. Usually this filter is combined with a window function (e.g. Shepp-Logan (Shepp and Logan (1974))), allowing different behaviours at high spatial frequencies.

### 4.2.4 Algebraic reconstruction methods

As it was mentioned before, apart from the analytical case, there is another class of reconstruction algorithms called *algebraic*, which includes all the iterative reconstruction methods used for the purposes of this thesis. This class considers the function $f(r)$ and its projections $p_\alpha(s)$ given on a discrete grid, e.g., as an image represented by pixels. In this case the Radon transform can be represented by a system matrix $R$, and all the other elements can be discretised as follows:

- the angle $\alpha$ by mean of $\alpha_i$ with $i \in \{1, 2, ...N_\alpha\}$
- the image $f(r)$ by mean of $f \in \mathbb{R}^m$ , with $m = N_x \times N_y$ pixels
- the projections $p_\alpha(s)$ by mean of $p_i \in \mathbb{R}^n$ with $n$ sampling points.

Thus, the system matrix $R_i$ for projection under an angle $\alpha_i$ will be an $m \times n$ matrix and the Radon transform can be formally written as a linear system of equations (Natterer (2001)):

$$p^i = R^i \mathbf{f} \tag{4.15}$$

defined for each angle $\alpha_i$. For $\mathbf{p} = (\mathbf{p}^1, ..., \mathbf{p}^{N_\alpha})$ and $R = (R^1, ..., R^{N_\alpha})$ this can be written as a single operation

$$\mathbf{p} = R\mathbf{f} \tag{4.16}$$

The described system of equations can be, in principle, directly solved however, due to the typical dimensions of an image, the number of the entries can be quite high and, hence, a direct inversion is not easily possible. For this reason, iterative methods, as the one proposed by Kaczmarz in 1937, take each measurement $\mathbf{p}^i$ and they consecutively enforce it by projecting the current guess to this measurement. If the measurements $\mathbf{p}^i$ have a consistent solution, it can be shown that this method will converge to a solution f of eq. 4.15 (Kaczmarz (1937)). An example for $f \in \mathbb{R}^2$ and $\mathbf{p}^i \in \mathbb{R}$ is given in Fig. 4.4.

Under certain assumptions, the current guess $\mathbf{f}^k$ will converge to the solution $\mathbf{f}$ after successively applying orthogonal projections to an initial guess $\mathbf{f}^0$. For $\mathbf{r}_j = (R_{j1}, R_{j2}, ..., R_{jm})^T$, being the transposed row $j$ of the matrix $R$, one iteration step can be written as (Kak and Slaney (2001)):

$$\mathbf{f}^{k+1} = \mathbf{f} + \frac{(p_j - \mathbf{r}_j \cdot \mathbf{f}^k)}{|\mathbf{r}_j|^2} \mathbf{r}_j \tag{4.17}$$

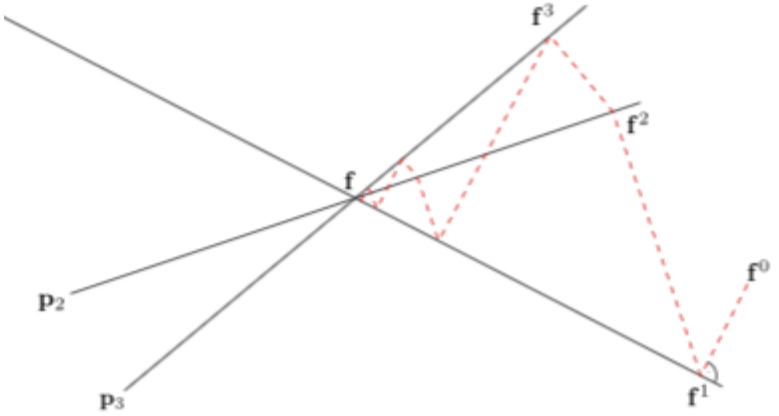


**Figure 4.4:** Illustration of the Kaczmarz method in $\mathbb{R}^2$. The measurements $p_i$ are given as three lines that have the desired solution $\mathbf{f}$ as a common intersection. Starting with an arbitrary solution $\mathbf{f}_0$ and projecting it to the measurement $\mathbf{p}_1$ brings the initial guess to $\mathbf{f}^1$, which is closer to the real solution $\mathbf{f}$. By applying successive orthogonal projections $\mathbf{p}_i$, the method will converge to the solution $\mathbf{f}$.

According with eq. 4.17, points laying on a projection line are corrected by the normalized difference of the re-projected value of a current guess, given by $\mathbf{r}_j \cdot \mathbf{f}^k$, and the measured value of the projection $p_j$ along the same line. This way to solve the tomographic problem is known as *Algebraic Reconstruction Technique* (ART) and it is one of the first proposed iterative methods. The detailed formalisms of all other iterative reconstruction algorithms used in this work won't be given as it goes beyond the scope of this thesis.

## 4.3 Artefacts in SR x-ray Tomography

As a tomographic image is the result of a dataset acquisition and a consequently application of a reconstruction algorithm, imperfection during the recording process may lead to significant artefacts in the final images. In this section, some of the typical artefacts that can occur and some of the general image processing methods commonly used to avoid them, will be presented.

### 4.3.1 Image normalisation

One of the most common problem occurring during a CT acquisition, is the inhomogeneity of the images. This non-uniform aspect can appear, not only in correspondence of the imaged sample, but also outside it, and it can have different origins, such as:

- the temporal instability of the incident x-ray beam due to a possible decrement of the machine current, to the vibrations or thermal drift of optical elements (e.g. filters, crystals) etc. . . .
- the spatial inhomogeneity of the incident beam due to some intrinsic inhomogeneity of the x-ray beam from the wiggler, defects or deformations of optical elements etc. . . .
- the detector response inhomogeneity caused by electron noise, pixels with different gain etc. . . .

To reduce these contributions to the image, usually during an acquisition, together with the object frames, also *darknoise* (taken without the beam illuminating the detector) and *whitefield* (taken with beam on and without sample in the x-ray beam) images are acquired. The normalisation procedure of the original image, usually applied off-line before the slices reconstruction, is finally carried out according the following formula:

$$normalised\ image = \frac{raw\ image\ -\ darknoise}{whitefield\ -\ darknoise} \tag{4.18}$$

where the subtraction and the division calculations are performed on a pixels-by-pixels basis. An example of the results of this normalisation is shown in Fig. 4.5.

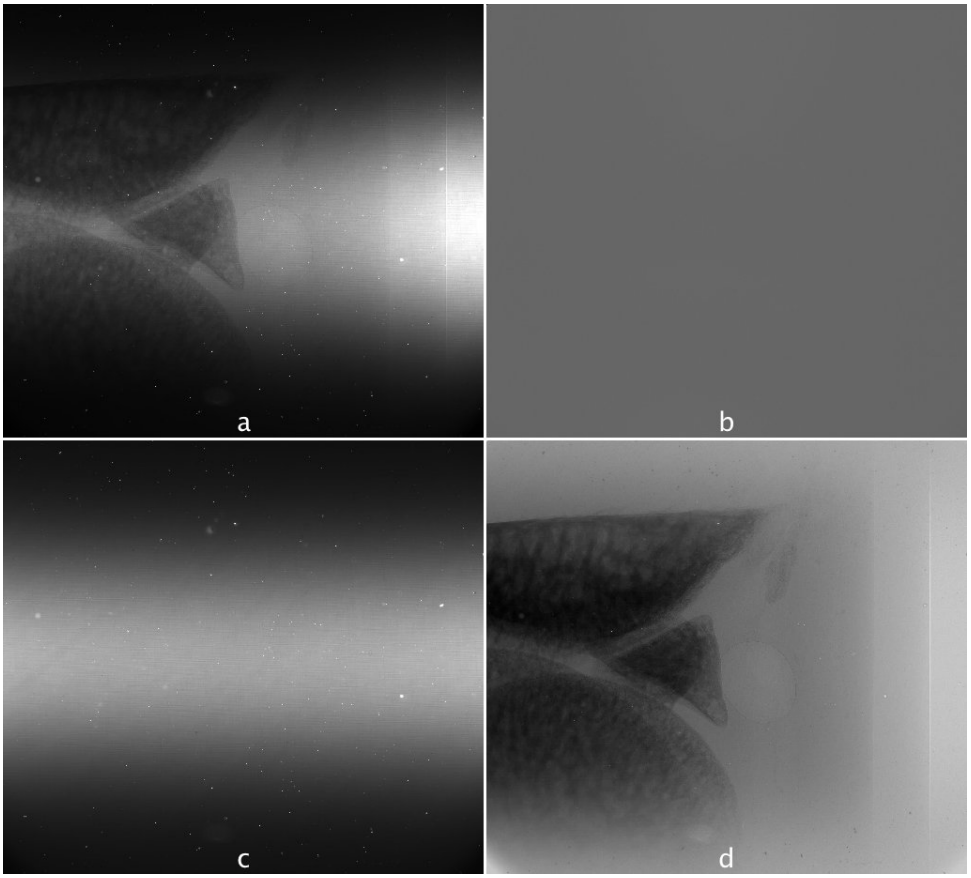


**Figure 4.5:** Normalisation procedure of a rat knee projection image. a) raw image; b) darknoise image; c) whitefield image; d) normalised image.

### 4.3.2 Ring artefacts and ring removal filters

Another recurrent artefact that typically degrades image quality in x-ray tomography, is the presence of concentric rings arising from the non-uniform pixel response of detector elements. The ring shape results from the back projection of stripe artefacts in the sinogram image, which is interpreted as a feature that always has the same distance to the centre of rotation and is present under each angle, thus the reconstruction algorithm will produce a ring. A usual way to overcome this problem is to de-stripe the sinogram, however, in order to avoid the need of additional imaging data (i.e. whitefield and sinogram images), it is possible to apply a de-striping filter directly to the transformed reconstructed slices. To do that, images are transformed into polar coordinates (where the value of the $x$ axis represents the distance from the rotation axis and the values on the $y$ axis

the rotation angle) so that the rings show up as lines parallel to the $y$ direction. Different de-striping filters have been used for the purposes of this thesis, and are briefly described in the following (Brun et al. (2013)).

*Rivers approach*: this method computes the average row of the sinogram by summing and dividing by the number of rows. It is important that the average raw has a very little high-frequency content, as real objects usually move in the sinogram, and are blurred out when computing the average row. At this point, anomalous detector elements will show up as spikes or dips in the average row. The magnitude of these detector anomalies is then computed by subtracting a smoothed version of the average row from the average row. Subtracting the result of this last step from each row in the sinogram, will result in a final sinogram with much less vertical striping (Rivers).

*Oimoen approach*: this filter uses a one-dimensional high pass filter orthogonal to the stripe artefact, to try to isolate the artefact itself from the useful signal. On the obtained high-pass filtered image is, then, applied a low-pass filter parallel to the stripe as the previous one, in order to separate the stripes from the high frequencies noise. At the end, the output image is the difference between the starting un-processed image and the filtered one (J. Oimoen (2000)).

*Boin and Haibel approach*: this filter performs, first, a sum of the grey values of the input image $f$, for each column $i$, resulting in the $y(i)$ signal. Then, after applying a low-pass filter giving $y_s(i)$, each row $j$ is corrected as: $f'_j(i) = f_j(i) \times y_s(i)/y(i)$. For its implementation, classic median or more refined weighted median filters can be used (Boin and Haibel (2006)).

*Münch et al. approach*: this method uses both wavelet and Fourier transform domain processing. In a first step, the structural information of the input image is separated into horizontal, vertical and diagonal bands at different resolution scales by wavelet decomposing the image into $L$ levels. Then, only on the bands containing the stripe information a FFT transformation is applied, followed by a Gaussian function with damping factor $\sigma$ used to remove the stripes. Finally, the de-striped image is reconstructed from the filtered coefficients (Münch et al. (2009)).

## 4.4 Reconstruction software descriptions and features

The SYRMEP Tomo Project (STP) is an in-house software suite composed by newly developed code as well as external libraries. It has been developed both to offer the essential pre-processing and the filtered back projection (FBP) reconstruction algorithm, and to effectively integrate single distance propagation-based phase-contrast experiments (Bravin et al. (2013)) where phase retrieval (Paganin et al. (2002)) is required. Moreover, additional reconstruction algorithms better suited for low-dose or fast CT, where a reduced number of noisy projections are collected, are also available. The STP has a graphical user interface and it is conceived to offer flexibility for the SYRMEP users in terms of an easy switch between a local and remote access (Brun et al. (2015)).

### 4.4.1 Pre-processing

As discussed in previous sections, a pipeline of several pre-reconstruction steps is necessary, such as flat fielding, hot/dark pixel correction, artefacts removal and grey level calibration. All these steps affect the computational time of the global reconstruction process in a non-negligible way. More significantly, their application does not guarantee that a global independent and parallel execution of 2D image processing algorithms "from acquired to reconstructed" can be performed. Barriers and synchronisation methods are required after each intermediate step. A basic distinction can be done between projection-order and sinogram-order pre-processing. While some of the pre-reconstruction steps are traditionally faced by processing each 2D projection (e.g. phase retrieval), other steps are usually effectively handled by processing each sinogram (e.g. ring removal). Moreover, the order of the steps in the pre-processing pipeline might significantly affect the image quality. For instance, a strategy for dark/hot pixel correction might prefer to process raw data projections while another strategy performs better after flat fielding correction. A ring artefacts compensation technique can in principle be applied before or after (or also two times, i.e. before and after) the phase retrieval step. Therefore, a

frequent switch between the projection-perspective and the sinogram- perspective of the dataset is necessary in a flexible pre-processing pipeline. This frequent perspective switch requires intermediate I/O since the imaged data to process is usually larger than the available memory.

### 4.4.2 Tomographic reconstruction

Regarding the image reconstruction methods, the SYRMEP Tomo Project is powered by ASTRA (Palenstijn et al. (2011)) and TomoPy (Gürsoy et al. (2014)). It integrates also publicly available reconstruction libraries (see e.g. Pelt and Batenburg (2014) and Miao et al. (2005)) as well as custom developed algorithms. Within the reconstruction process, a time-consuming task is the determination of the pixel in the acquired images to be assumed as the rotation axis. Ideally, once the acquisition setup is established, the centre of rotation should be known a priori and it could be adopted throughout the experimental session. However, it is often necessary to tune the centre for each dataset, because of mechanical imperfections in vertical or horizontal translation stages, thermal drifts, etc. Moreover, if the tomography system is perfectly aligned, then the rotation centre should be the same for all slices in the sample. However, there may be a slight misalignment of the rotation axis and the columns of the detector, such that there is a systematic change in the optimum rotation axis from the top to bottom of the sample. The STP offers automatic strategies for the determination of the centre of rotation in order to speed-up this time-consuming task.

### 4.4.3 Example of application

To show the benefits in terms of image quality when using different reconstruction algorithms and phase retrieval, this section presents a few results produced by the STP. A test object consisting of a polyoxymethylene ($CH_2OH$) cylinder, 16 $mm$ in diameter, in which six holes of 3 $mm$ diameter have been drilled parallel to the cylinder axis, was considered. The holes were filled with water ($H_2O$), paraffin wax ($C_{25}H_{52}$), glycerol ($C_3H_8O_3$), glucose ($C_6H_{12}O_6$) $10g/50ml$, glucose

$23g/50ml$, and one of them was left empty (see Fig. 4.6). The object was scanned at the SYRMEP beamline with the following experimental parameters: energy = 21 $keV$, sample-detector distance = 300 $mm$, water cooled 12 bit CCD camera (Photonic Science VHR, $4008 \times 2672$ pixels used in $2 \times 2$ binning mode resulting in pixel size = 9 $\mu m$) coupled to a Gadolinium Oxysulphide scintillator placed on a fibre optic taper. In this application, a value $\delta/\beta = 2178$ was used when applying Paganin's phase retrieval, the value was taken from a publicly available database (`https://ts-imaging.net/Services/Simple/ICUtilXdata.aspx`) and it corresponds to the refractive index of the polyoxymethylene at 21 $keV$.

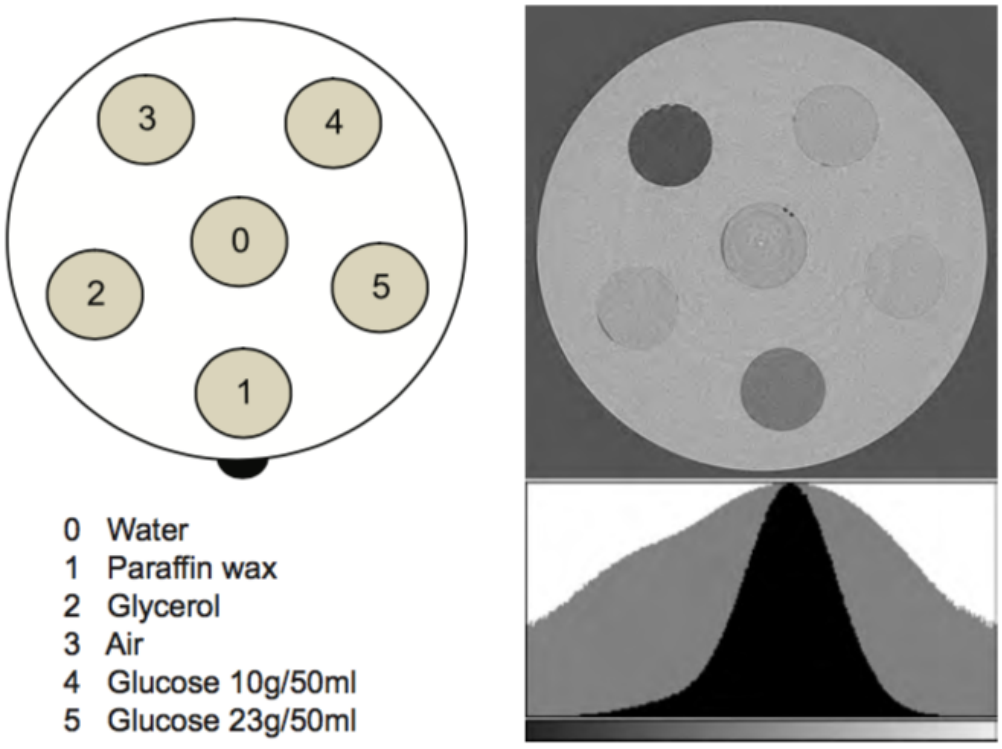


**Figure 4.6:** Scheme of the test object used in this performance testing study and edge-enhanced phase contrast reconstructed slice with FBP using 720 projections. Linear scale grey level histogram in black and logarithmic scale in grey.

Before the actual reconstruction, the projections were flat-field corrected and normalised by considering the air windows on the left and right side of the image as a reference. Then a ring removal filter was applied to better compensate the detector inhomogeneities. When considered, phase retrieval was performed at this stage.

Then, after the application of a reconstruction algorithm, images were calibrated to have a coherent grey scale for all of them. The calibration was performed by selecting the mean grey level of two meaningful and homogeneous areas in the image. A linear rescaling was then applied to each image. In addition to the FBP, the considered reconstruction algorithms are: Simultaneous Iterative Reconstruction Technique (SIRT), Simultaneous Algebraic Reconstruction Technique (SART), Conjugate Gradient Least Squares (CGLS) (Palenstijn et al. (2011)), Equally Sloped Tomography (EST) (Miao et al. (2005)) and Minimum Residual FBP (MR-FBP) (Pelt and Batenburg (2014)). The same number of projections was considered for all the algorithms but the non-linearly spaced angles that better approximate the requirements of the equally sloped tomography approach were adopted for the EST reconstruction. Fig. 4.6 reports the edge-enhanced phase-contrast image obtained by applying the FBP reconstruction algorithm (with Shepp-Logan filtering) after simple flat-fielding and ring removal when considering 720 projections. By observing the grey-level histogram, it can be noticed that image segmentation and further analysis might be hampered due to the monomodal distribution of grey tones. Figures 4.7 reports the output of different reconstruction algorithms after the application of the same pre-processing steps when considering 90 projections (meaning 1/8 of the acquisition time and radiation dose of the reference image). Figure 4.8 reports the results of the application of the same algorithms but with the addition of the intermediate phase retrieval step before the actual reconstruction. It can be noticed that while the most classical approach based on FBP without phase retrieval leads to a noisy image, where the different holes in the object can barely be recognised, iterative algorithms combined with phase retrieval are able to reconstruct images having multi-modal histogram where the inclusions within the phantom can be more easily segmented. Interestingly, promising results are obtained with the SIRT algorithm also without the application of phase retrieval.

However, in the images reconstructed after phase retrieval the phase-contrast fringes at the edges of the drilled holes in the phantom are correctly integrated and a better separation of the peaks in the image histogram is noticeable. Several

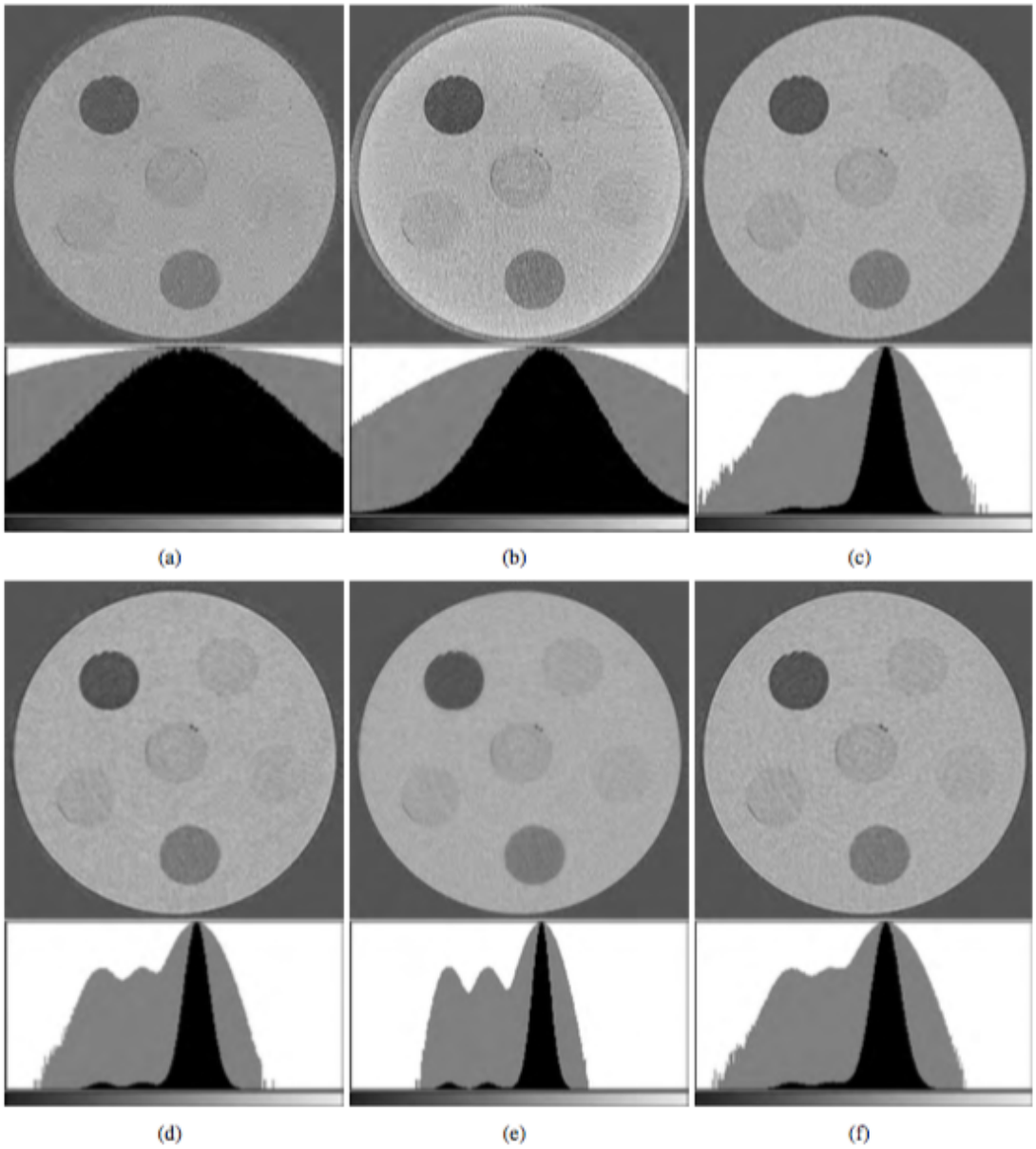


**Figure 4.7:** Reconstructed images when considering only 90 projections according to the following algorithms: a) FBP; b) EST; c) MR-FBP; d) SART; e) SIRT; f) CGLS. The related grey level histogram is reported below each image (the same grey level window was used for all the images). [Linear scale grey level histogram in black and logarithmic scale in grey]

applications can greatly benefit from such an enhanced and flexible reconstruction workflow where phase retrieval and iterative algorithms can be used. When the whole image processing pipeline can be applied in a reasonable amount of time, CT acquisitions with a reduced number of projections are possible, leading to a minimisation of the radiation damage or a faster experiment.

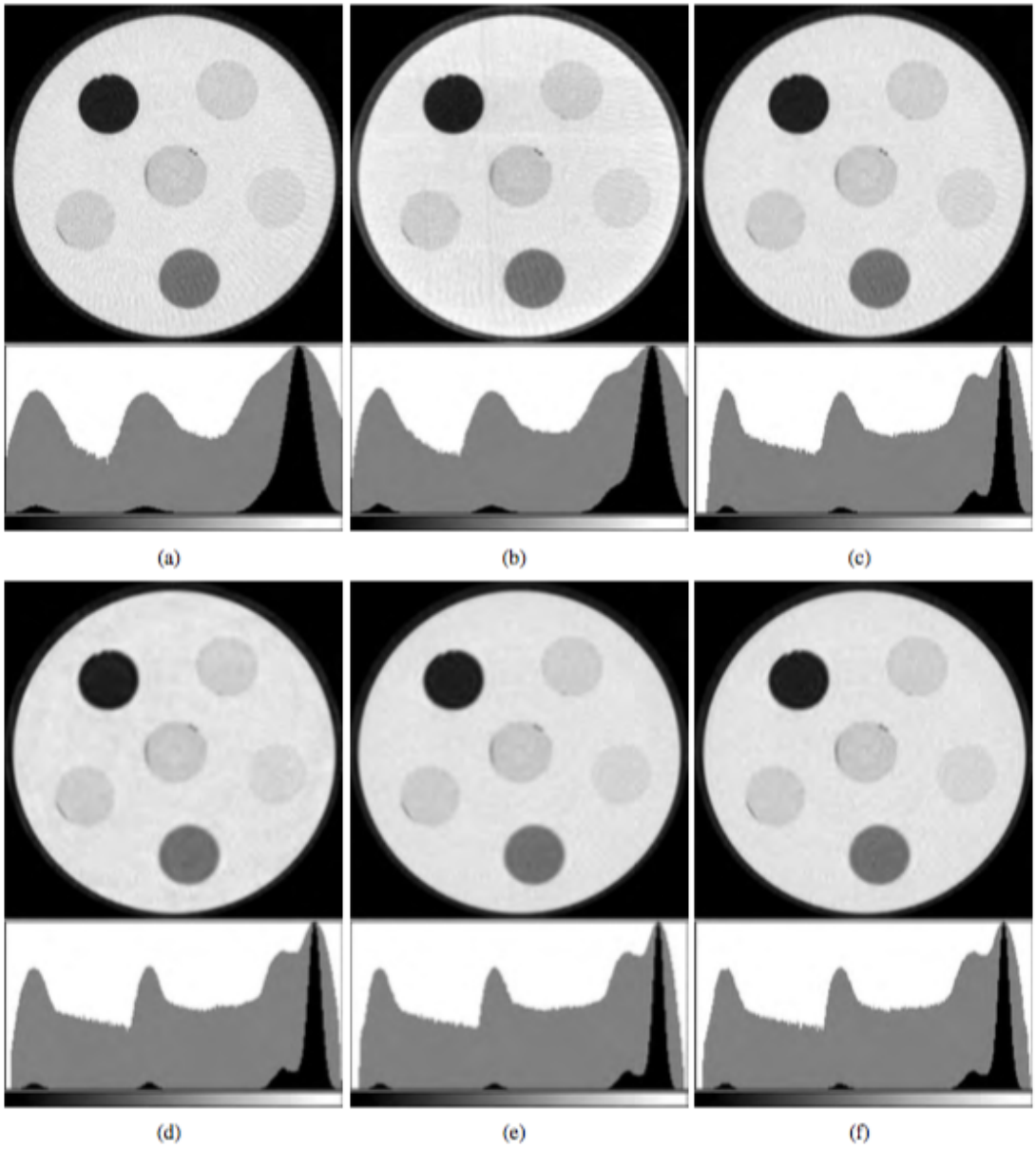


**Figure 4.8:** Reconstructed images after the application of phase retrieval when considering only 90 projections according to the following algorithms: a) FBP; b) EST; c) MR-FBP; d) SART; e) SIRT; f) CGLS. The related gray level histogram is reported below each image (the same gray level window was used for all the images). [Linear scale gray level histogram in black and logarithmic scale in gray]

## 4.5 Three-dimensional rendering

An important advancement in medical imaging technology, made possible by techniques as computed tomography and magnetic resonance, is, for sure, the three-dimensional (3D) visualisation. Developments in this field have revolutionised

the management of many aspects of health care and have led to improved surgical planning and treatments. All 3D rendering techniques represent a 3D volume of data in one or more two-dimensional (2D) planes, conveying the spatial relationships inherent in the data with use of visual depth cues. The data are organised into a 3D matrix of volume elements (voxels), and the dynamic range of the image is preserved, enabling display of (for breast images) vessels, soft tissue, calcifications and, not least, eventual benign or malignant lesions. Moreover, various parameters such as surface shading and opacity can help reveal both surface and internal detail and allow the radiologist or clinician to clearly distinguish most diseases.

### 4.5.1 Segmentation

One crucial step, to obtain a three-dimensional visualisation, is the extraction of the volumetric grade distribution of a particular phase type from a CT volume. Segmentation refers to the determination of the phase type for each voxel in the image, it represents the first heavy modification of the image and it can be considered as a "bridge step" necessary to any further analysis. There is no a unique standard approach to segmentation, the methods described in the following are the ones mostly used for the soft tissue case. The simplest segmentation technique is, probably, *thresholding*: the basic concept lies in the proper selection of a threshold value on the histogram intensities of a grayscale image (i.e. the slice). Individual voxels are, then, marked as "object" voxels if their value is greater than the selected threshold value, and as "background" voxels otherwise. Clearly, how to choose the threshold value, is a key step that can be done either "manually" or using different automatic approaches. A first method, divides arbitrarily the histogram in two parts, each one of them is then modelled with a normal distribution. The value chosen as optimal threshold is the one that minimise a minimum error criterion function between the model and the real histogram (Kittler and Illingworth (1986)). Another method proposes an iterative approach in which, at step n, the average of the foreground and background class means, are used to establish a new threshold $T_n$. The process will stop when the difference $|T_n - T_{n+1}|$ is small enough (Ridler and Calvard (1978)). A

widely diffused method, minimises the weighted sum of intra-class variances of the foreground and background voxels to establish an optimum threshold (Otsu (1979)). A method proposed by Tsai (Tsai (1985)) selects the threshold value imposing that the first three weighted average of the input image are kept in the output image. Another approach applies an entropic thresholding, that means that the obtained final image keeps as much as possible the information of the original image in terms of entropy (Pun (1981)). This method suggested the development of a new one, that considers the image foreground and background as two classes of events: the selected threshold value is the one that maximise the sum of the two entropy values. A more complex version of thresholding process changes the threshold value dynamically over the image instead of using a single value for all the voxels. In such a way, situation as changes in light condition resulting, for example, from a strong illumination gradient or shadows, can be avoided. The methods introduced so far, are able to handle situations with two separated phases, however, some applications may require a classification into more than two classes. For an image containing $N$ subpopulations of voxels having similar intensities, it is possible to select $N-1$ threshold value. In this case, histogram has different peaks of intensity values and the image is, usually, segmented by choosing more than one threshold (*multiple thresholding*) to separate the peaks (e.g., at the bottoms of the valleys between the peaks). A second approach applied in these situations is represented by the classification algorithms. All classification algorithms assume that the image depicts one or more features and that each of these features belongs to one of several distinct and exclusive classes. Classes can be specified automatically (unsupervised classification) or by the user (supervised classification). Classification algorithms, usually, have two steps of processing: a first one, called *training*, selects and isolates characteristic properties of some image features and then, based on these, creates a unique description of each classification category. The *testing* step is meant to use these feature-space partitions to classify image features (Haralick and Kelly (1969)). All these methods are based on the intensity property of the image, the other big class of methods exploits, for the segmentation, the spatial properties of

the image. The simplest approach belonging to this class is the so-called *region growing*: adjacent pixels of similar amplitude are gathered together to form the segmented region. The difference between the algorithms is in the rule they use to make growing the region. A first method combines pairs of pixels into groups called "atomic regions" if they have similar amplitude and they are spatially connected. Then, weak boundaries between regions are removed using heuristic rules (Brice and Fennema (1970)). The method proposed by Adams and Bischof (Adams and Bischof (1994)), asks the user to select a set of seeds corresponding to homogeneous areas. The seed can be either a single voxel or a small cluster of voxels, depending on the desired noise tolerance level. Then, conventional region growing proceeds with one new pixel added to each of the N seeded regions. The process proceeds until neighbouring regions meet at a common boundary. The last approach described in this section concerns the *edge detection* segmentation methods. These techniques segment the image into regions of similar characteristics by detecting the boundary of each region for which there is a significant change in attribute across the boundary (Marr and Hildreth (1980); Nalwa and Binford (1986)). However, this method is rarely used for segmentation of volume images.

# References

Adams, R., Bischof, L., 1994. Seeded region growing. IEEE Transactions on Pattern Analysis and Machine Intelligence 16, 641–647. doi:10.1109/34.295913.

Boin, M., Haibel, A., 2006. Compensation of ring artefacts in synchrotron tomographic images. Opt. Express, OE 14, 12071–12075. URL: https://www.osapublishing.org/abstract.cfm?uri=oe-14-25-12071, doi:10.1364/OE.14.012071.

Bravin, A., Coan, P., Suortti, P., 2013. X-ray phase-contrast imaging: From pre-clinical applications towards clinics. Physics in Medicine and Biology 58, R1–R35. doi:10.1088/0031-9155/58/1/R1.

Brice, C.R., Fennema, C.L., 1970. Scene analysis using regions. Artificial Intelligence 1, 205–226. URL: http://www.sciencedirect.com/science/article/pii/0004370270900081, doi:10.1016/0004-3702(70)90008-1.

Brun, F., Accardo, A., Kourousias, G., Dreossi, D., Pugliese, R., 2013. Effective implementation of ring artifacts removal filters for synchrotron radiation microtomographic images, in: 2013 8th International Symposium on Image and Signal Processing and Analysis (ISPA), pp. 672–676. doi:10.1109/ISPA.2013.6703823.

Brun, F., Pacilè, S., Accardo, A., Kourousias, G., Dreossi, D., Mancini, L., Tromba, G., Pugliese, R., 2015. Enhanced and Flexible Software Tools for X-ray Computed Tomography at the Italian Synchrotron Radiation Facility Elettra. Fundamenta Informaticae 141, 233–243. doi:10.3233/FI-2015-1273.

Buzug, T.M., 2008. Computed Tomography: From Photon Statistics to Modern Cone-Beam CT. Springer Science & Business Media. Google-Books-ID: fNH1fSnjwrkC.

Gürsoy, D., De Carlo, F., Xiao, X., Jacobsen, C., 2014. TomoPy: a framework for the analysis of synchrotron tomographic data. J Synchrotron Rad, J Synchrotron Radiat 21, 1188–1193. URL: http://scripts.iucr.org/cgi-bin/paper?pp5049, doi:10.1107/S1600577514013939.

Haralick, R.M., Kelly, G.L., 1969. Pattern recognition with measurement space and spatial clustering for multiple images. Proceedings of the IEEE 57, 654–665. doi:10.1109/PROC.1969.7020.

J. Oimoen, M., 2000. An effective filter for removal of production artifacts in U.S. Geological Survey 7.5-minute digital elevation models.

Kaczmarz, S., 1937. Angenäherte Auflösung von Systemen linearer Gleichungen. Bulletin International de l'Académie Polonaise des Sciences et des Lettres 35, 355–357.

Kak, A., Slaney, M., 2001. Principles of Computerized Tomographic Imaging. Classics in Applied Mathematics, Society for Industrial and Applied Mathematics. URL: http://epubs.siam.org/doi/book/10.1137/1.9780898719277. dOI: 10.1137/1.9780898719277.

Kittler, J., Illingworth, J., 1986. Minimum error thresholding. Pattern Recognition 19, 41–47. URL: http://www.sciencedirect.com/science/article/pii/0031320386900300, doi:10.1016/0031-3203(86)90030-0.

Marr, D., Hildreth, E., 1980. Theory of edge detection. Proc. R. Soc. Lond., B, Biol. Sci. 207, 187–217.

Miao, J., Förster, F., Levi, O., 2005. Equally sloped tomography with oversampling reconstruction. Phys. Rev. B 72, 052103. URL: https://link.aps.org/doi/10.1103/PhysRevB.72.052103, doi:10.1103/PhysRevB.72.052103.

Münch, B., Trtik, P., Marone, F., Stampanoni, M., 2009. Stripe and ring artifact removal with combined wavelet — Fourier filtering. Opt. Express, OE 17, 8567–8591.

URL: https://www.osapublishing.org/abstract.cfm?uri=oe-17-10-8567, doi:10.1364/OE.17.008567.

Nalwa, V.S., Binford, T.O., 1986. On Detecting Edges. IEEE Transactions on Pattern Analysis and Machine Intelligence PAMI-8, 699–714. doi:10.1109/TPAMI.1986.4767852.

Natterer, F., 2001. The Mathematics of Computerized Tomography. Classics in Applied Mathematics, Society for Industrial and Applied Mathematics. URL: http://epubs.siam.org/doi/book/10.1137/1.9780898719284. dOI: 10.1137/1.9780898719284.

Otsu, N., 1979. A Threshold Selection Method from Gray-Level Histograms. IEEE Transactions on Systems, Man, and Cybernetics 9, 62–66. doi:10.1109/TSMC.1979.4310076.

Paganin, D., Mayo, S.C., Gureyev, T.E., Miller, P.R., Wilkins, S.W., 2002. Simultaneous phase and amplitude extraction from a single defocused image of a homogeneous object. J Microsc 206, 33–40.

Palenstijn, W.J., Batenburg, K.J., Sijbers, J., 2011. Performance improvements for iterative electron tomography reconstruction using graphics processing units (GPUs). Journal of Structural Biology 176, 250–253. URL: http://www.sciencedirect.com/science/article/pii/S1047847711002267, doi:10.1016/j.jsb.2011.07.017.

Pelt, D.M., Batenburg, K.J., 2014. Improving Filtered Backprojection Reconstruction by Data-Dependent Filtering. IEEE Transactions on Image Processing 23, 4750–4762. doi:10.1109/TIP.2014.2341971.

Pun, T., 1981. Entropic thresholding, a new approach. Computer Graphics and Image Processing 16, 210–239. URL: http://www.sciencedirect.com/science/article/pii/0146664X81900381, doi:10.1016/0146-664X(81)90038-1.

Radon, 1917. Aber die Bestimmung von Funktionen durch ihre Integralwerte längs gewisser Mannigfaltigkeiten | BibSonomy. URL: https://www.bibsonomy.org/bibtex/fdcf4d741dfedba3c56a3a942ecc463b.

Ramachandran, G.N., Lakshminarayanan, A.V., 1971. Three-dimensional Reconstruction from Radiographs and Electron Micrographs: Application of Convolutions instead of Fourier Transforms. PNAS 68, 2236–2240. URL: http://www.pnas.org/content/68/9/2236.

Ridler, T., Calvard, E., 1978. Picture Thresholding Using an Iterative Selection Method. IEEE Transactions on Systems, Man, and Cybernetics 8, 630–632. doi:10.1109/TSMC.1978.4310039.

Rivers, M., . Tutorial Introduction to X-ray Computed Microtomography. URL: http://www.mcs.anl.gov/research/projects/X-ray-cmt/rivers/tutorial.html.

Shepp, L.A., Logan, B.F., 1974. The Fourier reconstruction of a head section. IEEE Transactions on Nuclear Science 21, 21–43. doi:10.1109/TNS.1974.6499235.

Tsai, W.H., 1985. Moment-preserving thresolding: A new approach. Computer Vision, Graphics, and Image Processing 29, 377–393. URL: http://www.sciencedirect.com/science/article/pii/0734189X85901331, doi:10.1016/0734-189X(85)90133-1.

# 5

# Application on Breast cancer diagnosis: optimisation of experimental and reconstruction parameters

## Contents

## 5.1 *Introduction*

When physics has to be applied to medicine, the purpose of the research is, clearly, driven by specific clinical issues, physicians define the target and what is important from a medical point of view. In addition, investigation modalities need to be adapted to the specific biological samples in terms of experimental conditions, sample positioning, data presentation and, most of all, delivered radiation dose. Consequently, the information content of the resulting images, is a compromise between a series of parameters (both experimental and not) that influence the image quality. For breast imaging, and for cancer detection in general, having a high-quality image means having an image on which it is possible to do a correct diagnosis, visualising all the important features that characterise the pathology. If this condition could be reached, keeping the radiation dose at a level comparable to that delivered in the present-day clinical 2D mammography, phase-contrast breast CT is likely to outperform the other imaging techniques in terms of diagnostic value and could be used in the large-scale screening programs significantly increasing their efficiency. To this aim, a pilot clinical study involving a limited number of patients is foreseen at the SYRMEP beamline of the ELETTRA synchrotron. The project, called SYRMA 3D (SYnchrotron Radiation for MAmmography), is carried out by a collaboration between INFN (Insituto Nazionale di Fisica Nucleare), University Hospital of Trieste, University of Trieste and Elettra Sincrotrone Trieste S.C.p.A. (Longo et al. (2016)). Thus, as a pre-requisite for successful translation of this technique into clinical practice, it is essential to evaluate, quantify and optimise the main parameters, i.e. the choice of X-ray energy, sample-to-detector distance, detector characteristics, strategies for CT scans and the reconstruction workflow. This needs to be done in order to maximise the image quality and therefore the diagnostic information. In this chapter three different works concerning the optimisation procedure, that can be considered as the main scope of this thesis, will be described.

## 5.2 The image quality assessment

As described in detail in Chapter 4, digital images are subject to a wide variety of distortions during acquisition, processing, compression, storage, transmission and reproduction, any of which may result in a degradation of visual quality. The optimal conditions for the use of PBI breast tomography technique in clinical application, are still not completely known. The major goal of this thesis work was to compare the quality of images obtained at different PBI conditions and processed following different strategies, in order to establish the optimum protocol for the practical application of this technique in breast cancer imaging. Another important aspect of the work, was to understand which is the most suitable method to assess the quality. When dealing with applications in which images need to be ultimately judged by clinicians, theoretically, the only correct method to assess the image quality is a subjective evaluation. Nevertheless, the subjective qualitative evaluation could be too inconvenient, time-consuming and expensive, especially when a large number of parameters influencing the final quality needs to be tested. For this reason, the goal of research in objective image quality assessment is to develop quantitative measures that can automatically predict the perceived image quality. Three main approaches will be described in the following sections, all of them have been sided and validated by a radiological assessment. In the first one, starting from a fixed acquisition setup, a series of reconstruction workflows are evaluated. The second and the third one extend the analysis to different experimental setups in conjunction with different reconstruction strategies.

## 5.3 Full reference indexes

In this first approach, a comparison of different low-dose CT reconstruction workflows for breast tomography is proposed. The opinion of expert radiologists was considered to support the evaluation process. With the ultimate aim of an unsupervised comparison, several quantitative metrics were computed to assess the quality of the reconstructed images. In addition to the evaluation of common image characteristics

(e.g., spatial resolution and signal-to-noise ratio - SNR), new image quality indexes are also presented, which are supposed to take into account the spatial resolution and noise sensitivity of the imaging setup simultaneously. The results presented here refer to a study performed at the SYnchrotron Radiation for MEdical Physics (SYRMEP) beamline of the ELETTRA synchrotron light source, which is, as mentioned in Chapter 3, so far the only synchrotron beamline where trials on human patients have been already conducted in 2D projection mammography mode (

### 5.3.1 Materials and methods

*Samples description and radiation dose assessment*

A polycarbonate phantom with the diameter of 10 $cm$ (Fig. 5.1a) containing 8 holes filled with different materials to simulate x-ray absorption and refraction characteristics of breast tissue was scanned at both high and low photon statistics (i.e. with different photon flux obtained by interposing filters between the source and the sample). A tissue specimen sampled during a surgical mastectomy obtained out of overleft material to be wasted was also scanned at high and low statistic (Fig. 5.1b). Before data acquisition, in addition to standard fixation, the specimen was sealed in a plastic bag under vacuum for a better conservation and handling. Prior to the surgical mastectomy the patient expressed the agreement about the possibility to use this material for scientific experiments. For both the considered samples the experimental parameters are: energy = 32 $keV$, sample-detector distance = 1 $m$, number of projections = 3600, detector binning = $2 \times 2$ with resulting voxel size = 54 $\mu m$ (due to a small geometrical magnification of 24/23 = 1.043 the effective pixel size in the sample plane is 51.75 $\mu m$). CT scans in low statistic were performed with 3600 projection at an Average Glandular Dose (AGD) calculated in the irradiated volume of 136 $mSv$. In order to obtain a value of AGD comparable to the clinical mammography, for each dataset only 1/10 of total projections with added simulated Poisson noise were considered. To be specific, noise was increased by measuring the standard deviation of a background area and multiplying it by a factor 3, thus the resulting AGD released to the sample is reduced to about 1.5

$mSv$. The evaluation of AGD has been performed from the values of air kerma measured by the ionisation chamber of the beamline and applying a Monte Carlo simulation code for the assessment of the delivered doses in the glandular tissue.

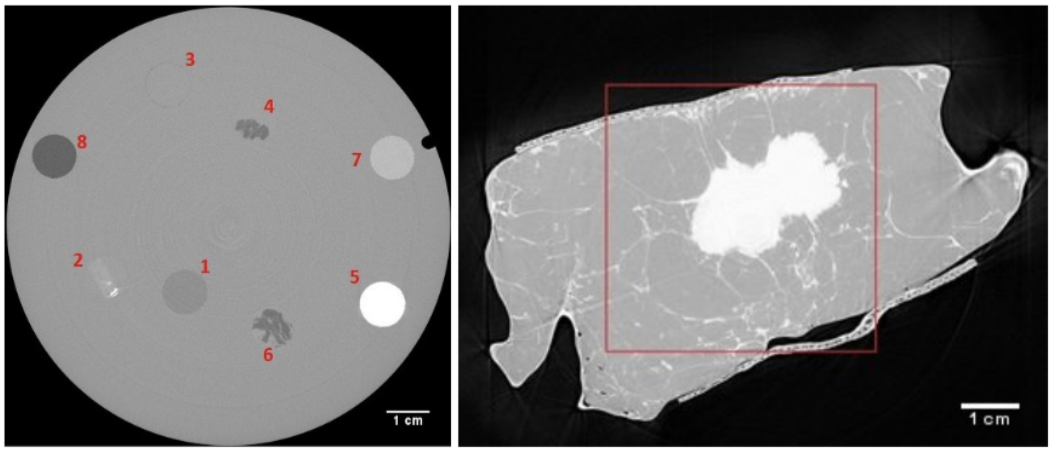


**Figure 5.1:** (a) Polycarbonate phantom where 1 = Glycerol ($C_3H_8O_3$), 2 = Unknown tissue (Malignant), 3 = Water ($H_2O$), 4 = Fibrous tissue, 5 = Calcium Chloride ($CaCl_2$), 6 = Adipose tissue, 7 = Paraffin wax, 8 = Ethanol ($EtOH$); (b) Reference image for the mastectomy sample reconstructed with FBP algorithm and considering 3600 high statistic projections. The red square indicates the region-of-interest used for the image quality assessment

*Reconstruction workflows*

In this manuscript reconstruction workflow refers to the entire process from the acquired projections to the final images, this means that it includes pre-processing steps, the reconstruction algorithm and post-processing steps. In all the considered workflows, before the actual reconstruction, the projections were flat-field corrected and normalised by considering the air windows on the left and right side of the image as a reference. Then a ring removal filter (Boin and Haibel (2006)) was applied in order to better compensate the detector inhomogeneity (Brun et al. (2013, 2015)). The considered CT reconstruction algorithms are: Filtered Back Projection (FBP) (Kak and Slaney (2001)), Simultaneous Iterative Reconstruction Technique (SIRT) (Van der Sluis and van der Vorst, 1990), Simultaneous Algebraic Reconstruction Technique (SART) (Gordon et al., 1970), Conjugate Gradient

Least Squares (CGLS) (van der Sluis and van der Vorst (1990)), Equally Sloped Tomography (EST) (Miao et al. (2005)), Total Variation (TV) minimisation (Tang et al. (2009)) and an iterative FBP algorithm based on the image histogram updates (Myers et al. (2010)). In addition, the effect of in-line single distance phase retrieval was considered. The phase retrieval was performed prior to the actual reconstruction by processing each projection independently, in accordance with the homogeneous Transport of Intensity (TIE-Hom) algorithm (Paganin et al. (2002)), using $\delta/\beta = 1000$ (i.e. a value close to the theoretical value of the ratio of the imaginary part to the real decrement of the relative x-ray refractive index for glandular and adipose tissues) as implemented in X-TRACT software (Gureyev et al. (2011)). A post-processing of the reconstructed images was also considered based on simple spatial filter over a neighbourhood of $w \times w$ pixels, including the optimal Epanechnikov kernel (Gureyev et al. (2014a)) and the edge-preserving image de-noising by the SUSAN method (Smith and Brady (1997)). All these reconstruction algorithms and image filters are available in X-TRACT software which can be downloaded and verified on request (link to sign-up form available here: `http://www.ts-imaging.net/Services/SignUp.aspx`). A summary of the considered workflows is reported in Table 5.1 which also contains the abbreviations used throughout this chapter.

*Quantitative evaluation of the images*

The evaluation of the reconstructed images was carried out by means of full-reference and no- reference image quality assessment indexes (Wang et al. 2004). In the full-reference approach, a complete reference image is assumed to be known. In this work, the reference image (Fig. 5.1b) is the one obtained by applying the FBP reconstruction algorithm and considering all the available projections acquired with high statistics. The underlying assumption is that, when a large number of high quality projections is available, the well-known and widely used FBP algorithm gives good results and therefore it can be assumed as the reference reconstruction

**Table 5.1:** Considered reconstruction workflows

| Abbreviation | Phase Retrieval | Reconstruction | Post-Processing |
|---|---|---|---|
| FBP | no | FBP | no |
| FBP-ITER | no | FBP-ITER | no |
| SIRT | no | SIRT | no |
| SART | no | SART | no |
| CGLS | no | CGLS | no |
| EST | no | EST | no |
| phr FBP | yes | FBP | no |
| phr FBP-ITER | yes | FBP-ITER | no |
| phr FBP-ITER *Epan17* | yes | FBP-ITER | Epanechikov (w = 17) |
| phr FBP-ITER *Susan5* | yes | FBP-ITER | Susan (w = 5) |
| phr TV-MIN | yes | TV | no |
| phr SIRT | yes | SIRT | no |
| phr SART | yes | SART | no |
| phr CGLS | yes | CGLS | no |
| phr EST | yes | EST | no |

workflow. The adopted indexes are: MSE - Mean Squared Error, SNR - Signal-to-Noise Ratio, UQI - Universal Quality Index (Wang and Bovik (2002)), NQM - Noise Quality Measure (Damera-Venkata et al. (2000)) and SSIM - Structural Similarity Index (Wang et al. (2004)). These characteristics are typically evaluated within a representative sub-region of the image where the pixel intensity values can be considered approximately spatially stationary (Geisler and Banks (1995); Wang and Bovik (2002)). While low values for the MSE index suggest a better image quality, higher values for SNR, UQI, NQM and SSIM are instead expected when a higher quality image is considered. The dimensionless no-reference intrinsic quality characteristic $Q_s$ which incorporates both the noise propagation and the spatial resolution properties of a linear system was computed according to the equation:

$$Q_s = \frac{SNR_{out}}{F_{in}^{1/2}} \Delta x \tag{5.1}$$

where $F_{in}$ is the mean value of the incident photon fluence (the number of incident photons per $n$-dimensional volume, in the current context, per unit area), $\Delta x$ is the spatial resolution of the imaging system and $SNR_{out} = S_{out}/\sigma_{out}$ is the

output signal-to-noise ratio (Gureyev et al. (2014a,b)). The CNR was calculated by selecting two meaningful areas of the image containing two strongly different grey levels: a region inside the lesion and a region within the adipose tissue. Then, the following formula was applied:

$$CNR = \frac{|< S_{fibrous} > - < S_{adipose} >|}{\left[\frac{\left(\sigma^2_{fibrous} + \sigma^2_{adipose}\right)}{2}\right]^{1/2}} \tag{5.2}$$

where $S_{fibrous}$ and $S_{adipose}$ are the average value in an homogenous region of fibrous or adipose tissue and $\sigma_{fibrous}$ and $\sigma_{adipose}$ are the corresponding standard deviations in the same regions, that are linked to photon counting noise in raw projections Gureyev et al. (2013); Nesterets and Gureyev (2014). Since the evaluation of FWHM requires a well defined image edge, this index was evaluated by considering the images of the polycarbonate phantom sample. The measure was carried out by taking ten line profiles (60 pixels length) at a polycarbonate - $CaCl_2$ detail interface. The profiles were then fitted with a non-linear sigmoid function. This function was then differentiated and the FWHM of the obtained Gaussian curve was evaluated (Fig. 5.2) (Mohammadi et al. (2014)). The choice to evaluate edges quality on this particular detail was made because $CaCl_2$ is the only detail that presents sufficient differences in grey levels allowing the measure; further in some images reconstructed without phase retrieval it is the only visible detail. It has to be pointed out that the $\delta/\beta$ ratio, used for the phase-retrieved reconstructions, is not optimised on the $CaCl_2$ but on the glandular and adipose tissue, so the selected detail is heavily affected by the phase-retrieval blurring effect.

*Radiological assessment*

Three experienced radiologists and one pathologist with long experience in pathological correlation with radiological imaging expressed a blind opinion in terms of identification of the lesion borders and spiculations, visibility of small connectival residues included in the adipose tissue, perceived contrast and spatial resolution of each reconstructed image. They were asked to give a global score from 0, for

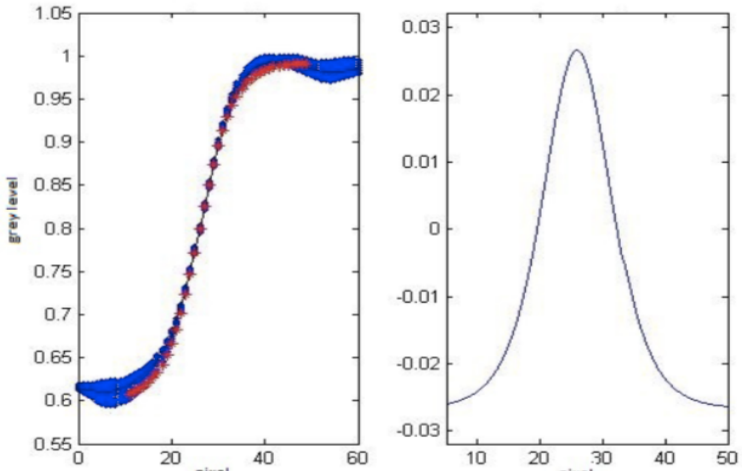


**Figure 5.2:** Edges quality measurement method. On the left part, the figure shows ten individual profiles (blue dots) and the fitted sigmoid function (red dots) used for the evaluation; the right part displays the obtained Gaussian curve where FWHM was calculated.

the worst case, to 4, corresponding to the best image, i.e. the FBP reconstructed slice obtained from the full statistic dataset with 3600 projections (float values were allowed). After a first evaluation, they did a more detailed rating comparing groups of two or three images that previously received the same assessment. Based on their opinion, the images were then classified into three categories: no-diagnostic power (mean radiological score from 0 to 2), i.e. it seems to be hard to diagnose the tumour; poor diagnostic power (mean radiological score from 2 to 3), i.e. it would be possible to diagnose the tumour but without an accurate evaluation of spiculations and/or connnectival residues existing in the tissue; full diagnostic power (mean radiological score higher than 3), i.e. all the relevant features are detectable and quantifiable.

### 5.3.2 Results and discussion

Figures 5.3, 5.3, 5.3 report some of the reconstructed images considered in this study. The images are grouped according to the three categories mentioned above. Table 5.2 reports the computed values for the full-reference indexes when considering the image of the breast tissue sample after the application of all the considered reconstruction workflows. First, it has to be pointed out that the most widespread and well known reconstruction method based on the FBP algorithm is definitely

outperformed by the other approaches. Indeed, the computed indexes suggest that the global quality of the images reconstructed with iterative algorithms is significantly higher than the one obtained with FBP. This is in line with the general consensus that when dealing with a limited number of noisy projections, algebraic techniques are better suited for the reconstruction of tomographic images.

**Table 5.2:** Numerical results of the full-reference quantitative image quality assessment

| | MSE | SNR [dB] | UQI | NQM | SSIM |
|---|---|---|---|---|---|
| FBP | 167.0E-07 | -2.91 | 0.0073 | 8.91 | 0.07 |
| FBP-ITER | 21.1E-07 | 6.09 | 0.0204 | 6.94 | 0.12 |
| SIRT | 6.2E-07 | 11.41 | 0.0403 | 10.00 | 0.28 |
| SART | 4.7E-07 | 12.54 | 0.0475 | 9.31 | 0.29 |
| CGLS | 9.5E-07 | 9.54 | 0.0338 | 9.19 | 0.25 |
| EST | 20.1E-07 | 6.29 | 0.0103 | 9.24 | 0.15 |
| phr FBP-ITER | 2.1E-07 | 16.17 | 0.0496 | 13.10 | 0.47 |
| phr FBP-ITER *Epan17* | 1.6E-07 | 17.25 | 0.0352 | 14.22 | 0.71 |
| phr FBP-ITER *Susan5* | 1.5E-07 | 17.57 | 0.0374 | 14.75 | 0.71 |
| phr TV-MIN | 1.5E-07 | 17.52 | 0.0419 | 14.29 | 0.69 |
| phr FBP | 2.2E-07 | 15.88 | 0.0403 | 12.91 | 0.51 |
| phr SIRT | 1.7E-07 | 16.92 | 0.0402 | 12.99 | 0.67 |
| phr SART | 1.7E-07 | 16.94 | 0.0408 | 12.82 | 0.67 |
| phr CGLS | 1.8E-07 | 16.88 | 0.0419 | 12.95 | 0.65 |
| phr EST | 1.8E-07 | 16.88 | 0.0361 | 12.98 | 0.61 |

The benefit of the phase retrieval pre-reconstruction processing should be noted as well. When comparing the performance of the same reconstruction algorithm with and without the application of phase retrieval (e.g. SIRT vs phr-SIRT), better MSE and SNR are revealed as well as a higher NQM value. The structural similarity index suggests an increased image quality as well. On the other hand, the UQI index seems to be less sensitive to the benefits of phase retrieval. A lower UQI is recorded for e.g. the phr-SART with respect to the SART reconstruction workflow while, instead, the MSE, SNR, NQM and SSIM suggest a better global image quality for the phr-SART. Moreover, a similar situation is observed for the group of FBP-ITER methods. The

MSE, SNR, NQM and SSIM indicate a better quality for this groups compared with the other reconstruction approaches when phase retrieval is considered. However, the UQI index does not seem to highlight the performances of this FBP-ITER based group. When adding post-processing filters to the FBP-ITER algorithm, the UQI index again seems unable to reveal differences that, on the other hand, MSE, SNR, NQM and SSIM seem to suggest. The values of the no-reference quantitative metrics are reported in Table 5.3 . Both the phantom and the tissue sample were considered to validate this approach. Since the resultant trend was quite similar in both cases, for simplicity and experimental relevance, it was chosen to report only the numerical values computed for the tissue sample. For the sake of clarity, these metrics were also applied to the image reconstructed with the FBP algorithm and considering all the projections acquired at high statistics (reference image). The two general trends that have been identified with the use of full-reference image quality indexes (i.e. the improvement of the quality as the consequence of using iterative CT reconstruction algorithms, compared to FBP, and also as a result of including the TIE-Hom phase retrieval into the reconstruction workflow), are repeated in the measured values of the no-reference quality index $Q_s$ (Table 5.3 ). The negative effect of lower spatial resolution on the $Q_s$ values can be seen for "phr-FBP-ITER Epan17" method, where the use of a broad (17-pixel wide) Epanechnikov filter led to the deterioration of the spatial resolution and, as a result, to a lower $Q_s$ score, even though the CNR was considerably higher than in the "phr-FBP-ITER" method, i.e. without the post-processing with the Epanechnikov filter.

On the other hand, the use of edge-preserving filters in the methods like "phr-FBP-ITER Susan5" or "phr-TV-MIN" did not lower the spatial resolution to the same degree and thus resulted in higher $Q_s$ values. As regards to the CNR and the FWHM values it has first to be reminded that they require a joint discussion since CNR solely can lead to misleading conclusions when computed after e.g. post-processing the reconstructed image with a low pass filter. In fact, in this case, the smoothing process produces an enhancement in contrast and noise but it negatively affects the spatial resolution. To better understand the duality of these

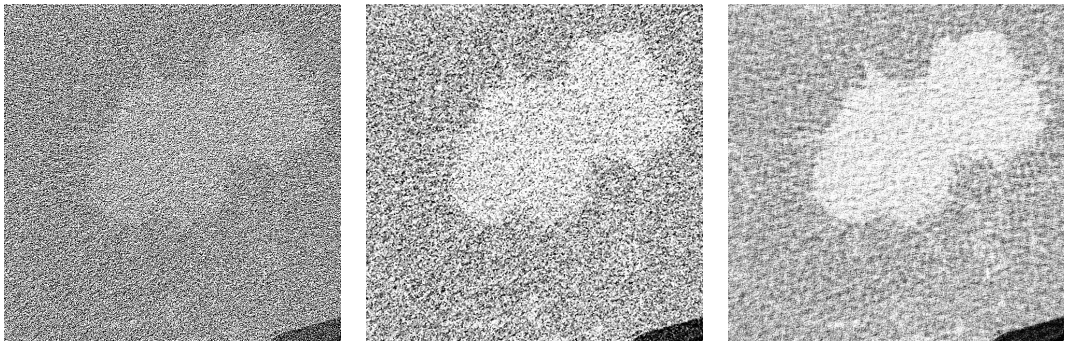

(a) FBP (b) FBP-ITER (c) CGLS

**Figure 5.3:** *No-diagnostic power.* Due to the specific clinical context the main lesion is still noticeable but a global poor contrast to noise ratio can be perceived and connectival residues are not visible.

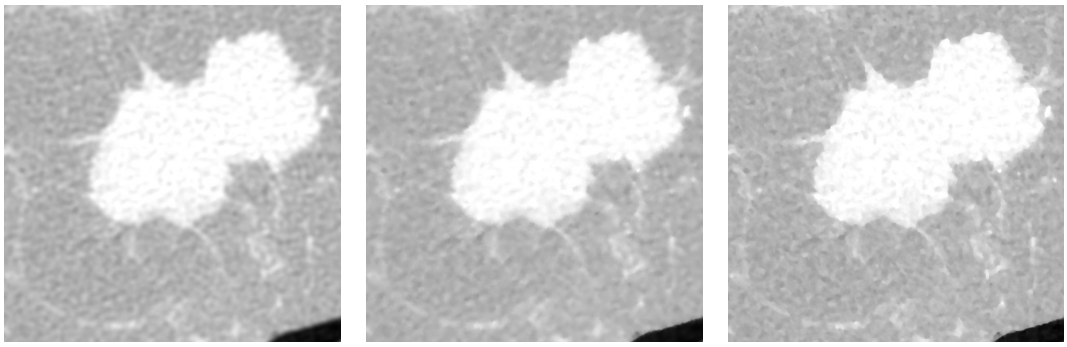

(a) phr FBP-ITER Epan17 (b) phr FBP-ITER Susan5 (c) phr TV-MIN

**Figure 5.4:** *Poor-diagnostic power.* Here the main lesion is well detectable thanks to the increased CNR, however the small connectival residues in the parenchimal area are yet not fully resolved, as well as the spiculations and the lesion borders.

two no-reference indexes, Fig. 5.6 reports in graphical form the relation between CNR' (contrast to noise ratio normalised by the selected area) and FWHM.

The values for the reference image are also plotted to better show that an optimal reconstruction workflow should be as close as possible to the reference, i.e. it should present a low FWHM value and high CNR. The results for the FBP workflow are not represented in Fig. 5.6 because it was impossible to identify an edge in the reconstructed image to be used for the computation of the FWHM. This confirms what already underlined after the application of the full-reference indexes, i.e. the iterative approaches overcome the FBP when dealing with a reduced number of noisy projections. From both Table 5.3 and Fig. 5.6 it could be noticed that the already

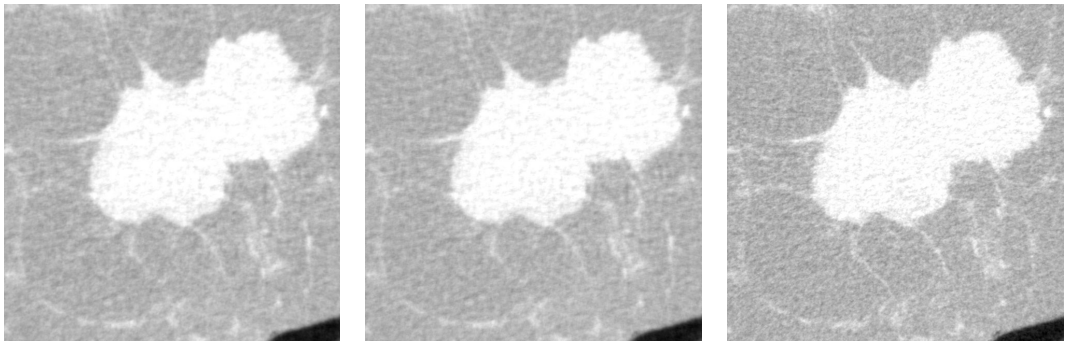

(a) phr SART (b) phr SIRT (c) phr EST

**Figure 5.5:** *Full-diagnostic power.* The main lesion with all the relevant features is clearly visible and quantifiable.

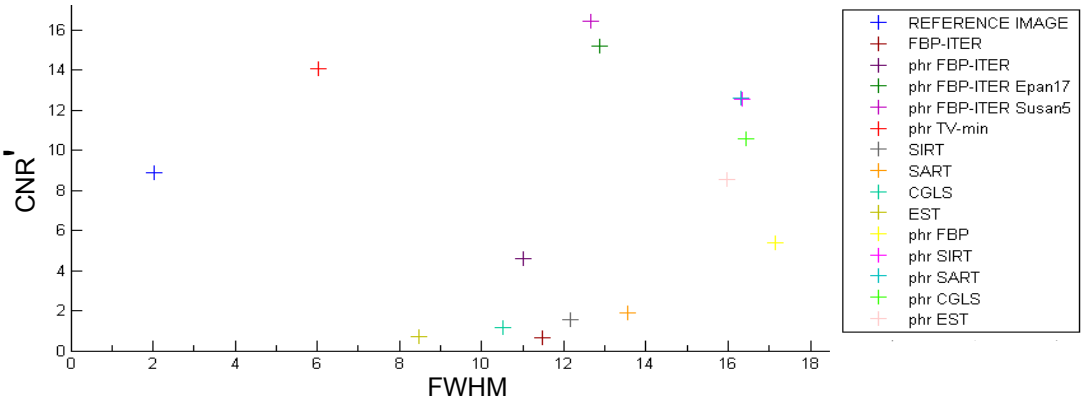


**Figure 5.6:** Full Width Half Maximum with Contrast to Noise Ratio measured on polycarbonate phantom. CNR′ measure is CNR normalised over the selected area.

underlined benefit of the phase retrieval pre-processing is due mainly to an increased CNR but, as expected, a degradation of the edges quality, i.e. a lower value for the FWHM, is also noticeable in the images where phase retrieval has been applied.

In order to better appreciate the effects of this pre-reconstruction processing, phase retrieval was applied also to the reference image and the no-reference indexes were assessed. The computed values are: CNR' = 30.53, FWHM = 5.82, $Q_{s(cancer)}$ = 62 and $Q_{s(adipose)}$ = 38. Again, a substantial improvement in the contrast with a slight reduction of the edges quality is noticeable. This confirms that the quality of the reconstructed image is altered mainly by the phase retrieval step and not by the specific reconstruction algorithm. Table 5.4 reports the results of the subjective evaluation of the images performed by the expert radiologists and the pathologist.

**Table 5.3:** Numerical results for the no-reference quantitative image quality assessment

| | CNR' | FWHM [pixel] | $Q_{s(cancer)}$ | $Q_{s(adipose)}$ |
|---|---|---|---|---|
| Reference Image | 8.88 | 2.03 | 18 | 12 |
| FBP | 0.20 | - | 1 | 0.5 |
| FBP-ITER | 0.67 | 11.47 | 2 | 1 |
| SIRT | 1.53 | 12.17 | 3 | 2 |
| SART | 1.89 | 13.56 | 4 | 3 |
| CGLS | 1.14 | 10.52 | 3 | 2 |
| EST | 0.73 | 8.48 | 2 | 1 |
| phr FBP-ITER | 4.62 | 11.01 | 8 | 5 |
| phr FBP-ITER *Epan17* | 15.18 | 12.88 | 5 | 4 |
| phr FBP-ITER *Susan5* | 16.47 | 12.67 | 17 | 13 |
| phr TV-MIN | 14.06 | 6.03 | 22 | 13 |
| phr FBP | 5.37 | 17.16 | 8 | 6 |
| phr SIRT | 12.58 | 16.35 | 13 | 10 |
| phr SART | 12.60 | 16.32 | 11 | 8 |
| phr CGLS | 10.58 | 16.43 | 14 | 10 |
| phr EST | 8.55 | 15.97 | 11 | 8 |

This subjective evaluation is fundamental to better understand if the benefits in terms of contrast resolution with the simultaneous reduction of edges quality induced by the phase retrieval are tolerated during the radiological evaluation process. The analysis of Table 5.4 with respect to Fig. 5.6 suggests that, at first, the observers focus the attention on the contrast resolution of the images. If an insufficient contrast is detected, a radiologist judges an image as meaningless for the diagnosis process. Beyond a level of contrast considered acceptable, the radiologists prefer the images having the highest edges quality (i.e. the lowest value of FWHM). Therefore, once this acceptable contrast level is identified, it seems that spatial resolution has to be privileged. This is because the diagnosis process for this specific application is based mainly on the morphology of the lesions in the tissue rather than contrast. According with this, "phr-FBP-ITER-Susan5" and "phr-FBP-ITER-Epan17" reconstructions workflow should have been judged as full diagnostic power images. Nevertheless, additional remarks should be made about the texture of these reconstructed images. One of the involved radiologists commented about this

**Table 5.4:** Qualitative assessment of the considered images performed by expert supervisors.

| | Radiol. 1 | Radiol. 2 | Radiol. 3 | Pathologist | Mean Score |
|---|---|---|---|---|---|
| FBP | 1 | 1 | 1 | 1 | 1 |
| FBP-ITER | 1 | 1 | 1 | 0.5 | 0.87 |
| SIRT | 1.5 | 1 | 1.5 | 1.75 | 1.43 |
| SART | 1.5 | 1.25 | 1.5 | 1.75 | 1.5 |
| CGLS | 1 | 1.25 | 1.5 | 1.5 | 1.31 |
| EST | 1 | 1.25 | 1.5 | 1.5 | 1.31 |
| phr FBP-ITER | 3 | 3 | 2.5 | 2 | 2.62 |
| phr FBP-ITER *Epan17* | 2.5 | 3.25 | 2.5 | 2.5 | 2.68 |
| phr FBP-ITER *Susan5* | 2.5 | 3.25 | 3 | 2.5 | 2.81 |
| phr TV-MIN | 1.5 | 2.75 | 2.75 | 2.75 | 2.43 |
| phr FBP | 2.5 | 2.5 | 2.75 | 3.5 | 2.81 |
| phr SIRT | 3.25 | 3.25 | 3.5 | 3 | 3.25 |
| phr SART | 3.25 | 3.25 | 3 | 3 | 3.12 |
| phr CGLS | 2.5 | 3.25 | 3 | 3 | 2.93 |
| phr EST | 3.5 | 3.25 | 3.5 | 3.5 | 3.43 |

and the subjective evaluation for these reconstruction workflows resulted strongly penalised by unrealistic image texture. Figure 5.7 reports the images reconstructed with phr-TV-MIN (affected as well by the same problem) and phr-EST, respectively.

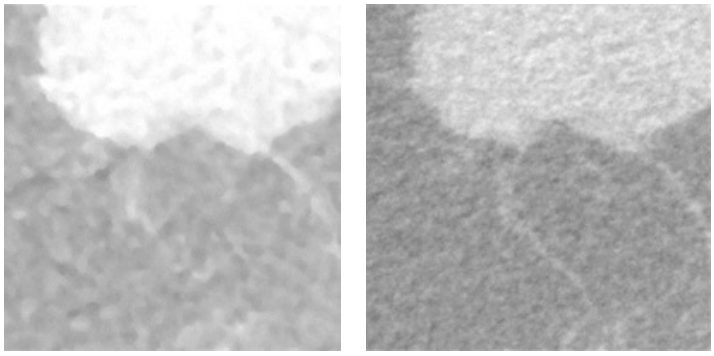

(a) phr TV-MIN (b) phr EST

**Figure 5.7:** Close-up of tissue sample slices pre-processed with phase retrieval and reconstructed with TV-Minimization (a) and EST (b) algorithm. In this small image portion the different textures are better noticeable.

A different texture, and a consequently lower visibility of spicules, is observed after the application of the considered implementation of a TV minimisation algorithm. Interestingly, none of the considered quantitative metrics seemed able to reveal this aspect. Further optimisation of this work should include also a

quantitative evaluation of textural features in the reconstructed images. Moreover, it seems that the radiologists are not concerned by a strong amount of noise in the reconstructed image. This could help the optimisation of the reconstruction workflow since, in order not to sacrifice the spatial resolution, usually more noise can be tolerated. With the aim of an unsupervised evaluation of breast CT images, an additional correlation between the subjective score proposed by the medical personnel and some of the proposed indexes is reported in Fig. 5.8. There is a general agreement between most of the evaluated image quality scores and the radiological assessments, at least as far as the general trends are concerned. Overall, among all the evaluated objective image quality measures, the SSIM score (multiplied by the factor of 6) tracked the radiological assessments the closest.

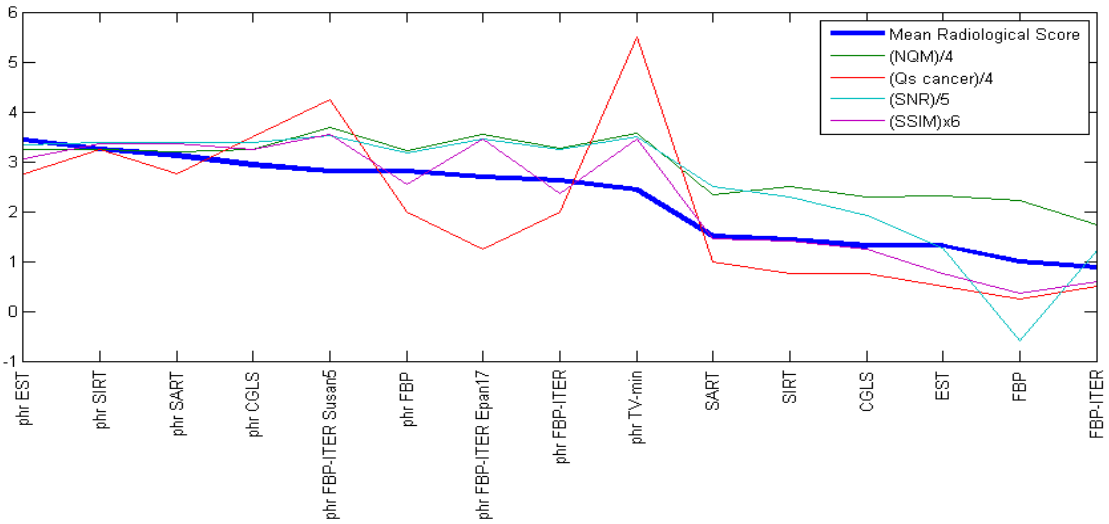


**Figure 5.8:** Correlation between the radiological score and various image quality indexes.

It is worthy to underline that the considered mastectomy sample includes an opacity compatible with a malignant lesion of about 3 *cm* where irregular edges, blurred margins and spicules are strongly visible. Moreover, the lesion is part of a convoluted breast where thin connectival trabeculae are clearly noticeable. When considering this specific diagnostic context, the radiologists confirm that a diagnosis is easy to perform. With the support of the anatomo-pathology unit, further activities will be focused in the search of a more challenging mastectomy sample where e.g. the excised tissue presents small satellite lesions and therefore a

diagnosis could be less easy to perform. Together with the evaluation of additional reconstruction methods, this will help a future refinement of the reconstruction workflows identified in this article as those producing images with full diagnostic power. This should be done in order to better identify the reconstruction workflow most suitable for an in vivo application of low-dose phase contrast breast CT. Finally, in the framework of a clinical trial, further work should be dedicated to the application of the proposed methodology to other experimental setups, such as e.g. different sample-to- detector distances and X-ray energies. An optimisation of the detector to be used is also necessary. The one adopted in the experiment presented in this article was chosen for its high spatial (an effective pixel size of 54 $\mu m$) and contrast resolution, nevertheless for CT *in-vivo* studies on patients, an optimised version with a faster readout will be required. To this aim, the next described work was meant to extend the analysis to other experimental setups and image processing strategies, applying some of the indexes used in this section.

## 5.4 Radiological assessment

This second study a comparison of the results obtained with different experimental setups is carried out, such as different propagation distances and energies, and subsequently evaluated the image acquisition protocols as well as the image reconstruction algorithms. The collected x-ray projection images were optionally phase retrieved using the TIE-Hom method (Paganin et al. (2002)). Subsequently, 3D images of the breast tissue were reconstructed using different CT methods, such as simultaneous iterative reconstruction technique (SIRT) (van der Sluis and van der Vorst (1990)), iterative filtered back projection (iFBP) (Myers et al. (2010)) and several others. A quantitative evaluation of the reconstructed images was performed using several objective image quality metrics, such as the spatial resolution, signal-to-noise ratio (SNR) and the intrinsic quality characteristic $Q_s$ (Gureyev et al. (2014b)). A radiological assessment of the obtained PB-CT images by a relatively large group of 13 medical imaging specialists was carried out and it was demonstrated that the subjective scores assigned by these specialists to different images were generally

in good agreement with the objective image quality indices of the same PB-CT images of the breast tissue specimen. The image quality indices obtained for an extended range of examined parameters (e.g. different distances and energies) were consistent with the theoretical results of propagation-based phase contrast analysis. Also, for the first time in this work a successful cross-identification of features and comparison between histological images and x-ray images obtained with PB-CT of breast tissues, has been performed.

### 5.4.1 Materials and methods

*Experimental setup*

In this study two different detectors were used: Hamamatsu CMOS Flat Panel Sensor C9252DK-14 and DALSA Argus high-resolution CCD TDI sensor. The Hamamatsu detector was used in the partial scan mode, which had a smaller pixel size 100 x 100 $\mu m^2$ at the expense of reduced field of view, compared to the full scan mode of the same detector. This detector has a CsI scintillator directly deposited on a 2D photodiode array. The Dalsa detector was used in the $2 \times 2$ binning mode with an effective pixel size of $54 \times 54 \mu m^2$. Geometrical magnification was taken into account in the evaluation of the effective pixel size of the detectors and sample-to-detector distances (table 5.5). The samples were imaged at three different energies: 32, 35 and 38 $keV$, in PB-CT mode using four different levels of photon statistics (see table 5.7 for the associated radiation doses). The CT scans were collected at three different sample-to-detector distances $R_2 = 0.16$, 1.85 and 9.31 $m$, the latter resulted in strongest phase contrast. Each scan contained 2000 projections collected with 0.18°angular step over 360°. For correction of the x-ray projections, 40 dark current images and 40 flat field images were also collected, half before and half after each sample scan.

*Breast tissue sample*

One human breast tissue specimen (Fig. 5.9) excised during a surgical left mastectomy procedure, was prepared for x-ray phase-contrast CT imaging and for

histological examination. The sample with a malignant lesion was provided by the Department of Pathological Anatomy, University of Trieste Medical School, Cattinara Hospital, Trieste, Italy. The sample was taken from a 67 year-old woman with bro-adipose breast parenchyma. During the histological examination, multiple foci of intraductal papillomatosis and sclerosing adenosis were found. Moreover, histological examination found invasive ductal carcinoma, moderately differentiated (grade 2) with solid-trabecular and focally lobular-like aspects. The maximum diameter of the tumour was 27 $mm$. For imaging, the sample was fixed in formalin and sealed hermetically in a polyethylene container. The specimen was approximately 12 $cm$ by 7.5 $cm$ transversely and about 4 $cm$ thick. Note that the transverse dimensions of the sample were consistent with the conditions of full breast CT imaging, while the thickness of the sample was also larger than the height of the x-ray beam.

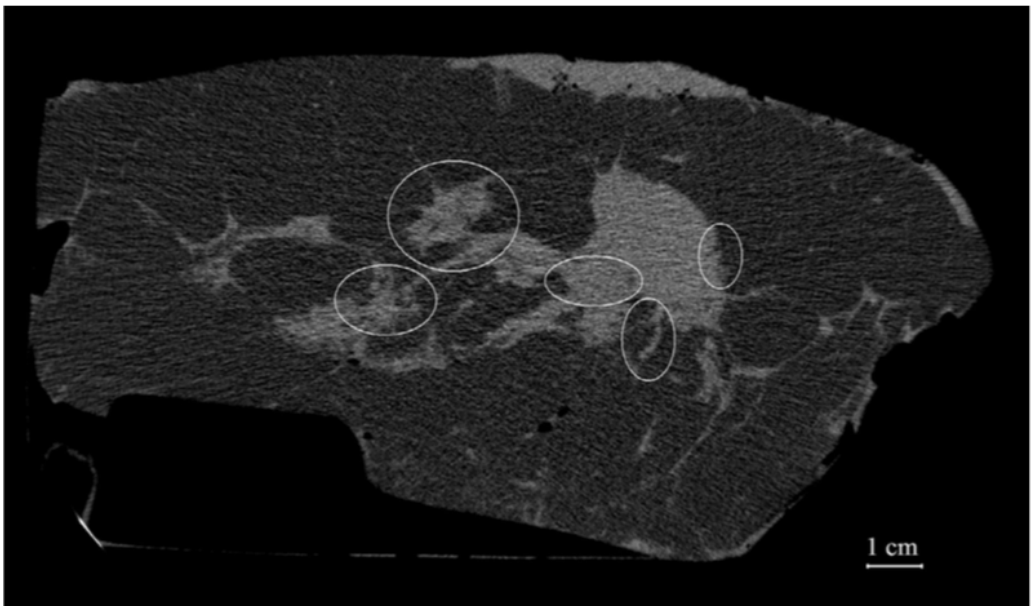


**Figure 5.9:** Reference image of breast tissue sample used in the radiological assessment (SIRT reconstruction from 1000 projections with 1000 iterations, $R_2 = 0.16\ m$, E $= 32\ keV$, Dose $= 2\ mGy$). This image represents an approximation for the conventional (absorption-based or "contact") mammographic image, with the best overall image quality achieved using different reconstruction methods from the data collected at the shortest propagation distance at a given radiation dose. White ovals represent five regions-of-interest (ROIs) which were used for rating in the radiological assessment.

*Radiation dose estimation*

During the experiment, an ion chamber (IC) was installed in the x-ray beam. The readings from the IC, which were used for measuring the photon fluence rate, were recorded during the CT data acquisition. In order to calculate the mean absorbed dose ($D_{abs}$) of the breast tissue, a numerical phantom with the cross-section schematically depicted in figure 5.10 (Dance (1990); Protection and Measurements (2004)) was used. The phantom simulates the breast tissue with radius r (in $cm$) and composed of 50w% gland tissue and 50w% adipose tissue (Hammerstein et al. (1979)), surrounded by adipose tissue (simulating the skin layer) enclosed inside a cylinder of radius Rout (in $cm$). Using this phantom, the mean absorbed dose can be calculated by converting the photon fluences in the sample plane as follows (Johns and Yaffe (1985); Nesterets and Gureyev (2014); Nesterets et al. (2015)):

$$D_{abs}(mGy) = \frac{2}{\pi} 1.602 \times 10^{-10} \frac{R_{out}(cm)}{r^2(cm^2)} \frac{R_{abs,r}\phi(\text{ph cm}^{-2})E(keV)}{\rho_r(\text{g cm}^{-3})} \tag{5.3}$$

Here $R_{abs,r}$ is the fraction of x-ray energy incident on the phantom which is absorbed in the glandular tissue, $\phi$ is the incident photon fluence (in photons per $cm^2$), $\rho_r$ is the mass density of the glandular tissue (in $g\ cm^{-3}$) and E is the x-ray energy (in $keV$). The $R_{abs,r}$ values were calculated using Monte Carlo (MC) simulations with 5 $cm$ and 4.5 $cm$ for $R_{out}$ and $r$, respectively (Nesterets et al. (2015)), assuming that the entire phantom (unlimited along its axis) is uniformly illuminated by the x-ray beam. These values correspond to the dimensions of the sample used in the experiment. Results of this simulation for three different energies are shown in Table 5.5. As mentioned above, for each energy, scans were made with four different levels of photon statistics, achieved by utilising Aluminium filters of varying thickness in combination with variable exposure time (Table 5.6).

*CT reconstruction procedure*

X-TRACT (Gureyev et al. (2011)) and STP (Brun et al. (2015)) software were

**Table 5.5:** Values of the $R_{abs,r}$ calculated using MC simulations for the phantom shown in figure 5.10 for three energies used in the experiment.

| | Photon Energy ($keV$) | | |
|---|---|---|---|
| | 32 $keV$ | 35 $keV$ | 38 $keV$ |
| $R_{abs,r}$ | 0.455 | 0.404 | 0.358 |

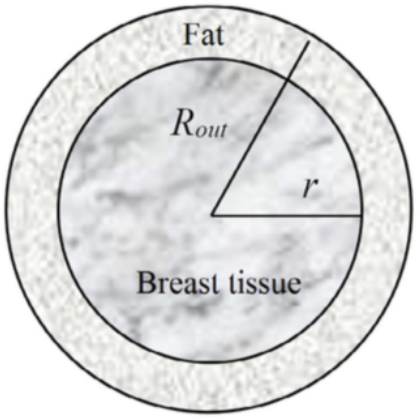


**Figure 5.10:** A schematic diagram of the numerical phantom used for mean glandular dose calculations (Nesterets et al., 2015).

used for CT data processing and analysis which included data pre-processing and CT reconstruction. The pre-processing of projection images contained the following steps:

1. dark current correction, consisting of subtraction of mean dark current image (collected with no x-ray illumination) from the datasets and from the flat-field images in order to remove the detector dark current contribution,

2. flat-field correction, using images collected with the x-ray illumination but without the sample to correct for uneven illumination,

3. optional phase retrieval, using the TIE-Hom algorithm (Paganin et al. (2002))

4. ring removal filter for reducing ring artefacts caused by imperfect detector pixel elements (Boin and Haibel (2006)).

The TIE-Hom algorithm was optionally applied to the projection data sets, in order to optimally exploit the phase information, with different values of $\delta/\beta$ ratio. Here the $\beta$ value, which constitutes the imaginary part of the complex refractive index $n = 1 - \delta + i\beta$, is related to the absorption, while the $\delta$ value, is related to the phase shift. The application of the TIE-Hom algorithm, as seen in previous

**Table 5.6:** Values of the mean glandular absorbed doses for breast tissue sample calculated by using the cylindrical numerical phantom shown in figure 5.10 (with the outer radius $R_{out} = 5\ cm$ and the inner radius r = 4.5 $cm$). Only the data corresponding to scans with the Hamamatsu detector is given here, as the scans collected with the Dalsa detector have not been used in the radiological assessment in the present study.

| | | Mean Glandular Absorbed Dose ($mGy$) | | |
|---|---|---|---|---|
| | | $R_2(m)$ | | |
| E ($keV$) | Photon statistics | 0.16 | 1.85 | 9.31 |
| 32 | High | 114.51 | 150.13 | 277.33 |
| | Medium | 14.63 | 19.08 | 34.67 |
| | Low | 7.32 | 9.22 | 17.18 |
| | Very Low | 4.13 | 4.64 | 8.43 |
| 35 | High | 86.87 | 101.39 | 183.6 |
| | Medium | 10.79 | 13.15 | 26.1 |
| | Low | 5.58 | 6.51 | 11.44 |
| | Very Low | 2.81 | 3.43 | 8.22 |
| 38 | High | 82.98 | 100.4 | 18;779.88 |
| | Medium | 10.41 | 12.55 | 23 |
| | Low | 4.87 | 7.57 | 9.89 |
| | Very Low | 2.29 | 3.77 | 5.32 |

chapters, is particularly useful for imaging objects consisting of components with similar x-ray attenuation properties. For each energy, two different values of $\delta/\beta$ were used. The first value was close to the theoretical value (TS-imaging website) of the relative $\delta/\beta$ value for glandular tissue in adipose tissue ($\delta/\beta$ = 870, 978, 1083 for 32, 35 and 38 $keV$ respectively), while the second was equal one was equal to the half of the first value. This latter value of $\delta/\beta$ was included into the study to test the hypothesis that such "partially phase retrieved" image can be approximated

by a mixture of the raw phase-contrast image, which typically has sharp edges, and the phase-retrieved image, which typically has better grey-scale differentiation for soft tissues, can potentially deliver an optimal combination of the two desirable properties (edge sharpness and soft tissue differentiation). Normalised projections were converted to sinograms after pre-processing, and each sinogram was used to reconstruct the (dimensionless) distribution of the imaginary part of the complex refractive index, $\beta(x, y, z_0) = (\lambda/4\pi)\mu(x, y, z_0)$, within a single transverse slice of the sample ($\lambda$ is the x-ray wavelength and $\mu$ is the linear attenuation coefficient). In this study, several different CT reconstruction algorithms were used, but since some of them have been already object of the optimisation described in the previous section, the results obtained with only two algorithms are included in the present paragraph: iterative filtered back-projection (iFBP), which is available in X-TRACT software, and simultaneous iterative reconstruction technique (SIRT), which is available in STP software.

*Radiological assessment*

The radiological assessment was conducted on the basis of PB-CT x-ray images with acceptable radiation doses obtained during the experiment. Thirteen imaging specialists (seven radiologists and six diagnostic radiographers), each with over five years? experience in assessing radiologic images, participated in the assessment. In the current stage of the evaluation, 81 images obtained with the Hamamatsu detector and different experimental parameters (distances and energies) were assessed. All images were reconstructed using two algorithms, iFBP and SIRT (the latter using 400 and 1000 iterations), following the application of the TIE-Hom phase retrieval algorithm with two different values of $\delta/\beta$ ratio (depending on the energy) and also without phase-retrieval algorithm. For each of the reconstructions, only one half of the collected projections (i.e. 1000) were used in order to reduce the effective dose to an acceptable level (around 4 $mGy$). The imaging specialists were asked to assess 6 image attributes within the 5 regions of interest (ROIs) outlined in the image (figure 5.9), in comparison with the same ROIs in the selected reference

image (obtained at $R_2 = 0.16\ m$ and E = 32 $keV$, without phase retrieval), which corresponds to standard CT. The reference image was obtained using the SIRT algorithm (with 1000 iterations), because it gave us the best results for the images without phase contrast. The following attributes of the images were rated: soft tissue contrast (degree of differentiation of the densities of various soft tissue regions), edge sharpness (clarity of definition of edges and outlines of structures), soft tissue interfaces (clarity of visualisation of interfaces between different soft tissue elements), spiculations (sharpness of reproduction of spiculations), artefacts (distractiveness of image mottle and other artefacts) and image noise (distractiveness of noise in the image). Each attribute was rated using a five-point scoring scale. The meaning of the rating scores was as follows: the fulfilment of the corresponding criteria in the new image was clearly better than (+2); slightly better than (+1); equal to (0); slightly worse than (-1); and clearly worse than (-2) the fulfilment of that criteria in the reference image. For each image the mean values of all attributes were calculated. All images were assessed using primary reporting workstations with 5 megapixel monitors, which were calibrated to the grayscale standard display function. Ambient lighting did not exceed 40 $lux$.

### 5.4.2 Results and discussion

The results of the radiological image assessment have confirmed that the propagation (sample-to-detector) distance was the most important variable of the experiment. The highest values in radiological scoring were consistently achieved for images obtained at the longest propagation distance. Additionally, images obtained at 32 $keV$ received better scores on average compared to the other energies. Images, for which the TIE-Hom algorithm was applied, received higher scores than images reconstructed without phase retrieval. To objectively assess the images used in the radiological assessment, the values of three "no-reference" indices, including the signal-to-noise ratio (SNR), the spatial resolution ($\Delta r$) and the intrinsic quality index $Q_s$ ((Gureyev et al. (2014a,b))) were calculated using X-TRACT software. For each image, two values for each of the above indices were obtained, using the

same size area (128 × 128 pixels), one inside and one outside the lesion. Within these areas, we calculated, using X-TRACT software, the mean of the pixel intensity values and its standard deviation. The SNR was then evaluated as the ratio of the mean to the standard deviation. The spatial resolution was calculated from the power spectrum of image noise (which was calculated from the power spectrum of image noise (which was de ned as the difference between the value of intensity in a given pixel and the mean intensity value within the area). Assuming that the incident photon flux within the selected small uniformly illuminated area was spatially stationary, ergodic and had Poisson statistics, it was possible to find the width of the system PSF by measuring the effective width of the power spectrum of the image noise. Indeed, while the power spectrum of incident white noise was uniform, the convolution with the detector PSF, phase retrieval and the CT reconstruction led to multiplication of the power spectrum by the square of the corresponding modulation transfer function (MTF). Therefore, by calculating noise power spectrum within the selected uniformly illuminated area of an image, we could determine the width of the MTF, and then calculate the width of the PSF assuming a certain general functional form of the PSF (Gaussian PSF is assumed in X-TRACT). The spatial resolution of the imaging system (including all the post-processing operations) was equated with the width of that PSF, referred back to the object plane (note that the x-ray source size had relatively minor contribution to the resolution in the used imaging configurations). After calculating both the SNR and the spatial resolution, their ratio was calculated, $SNR/\Delta r$, which, by definition, coincides with the product of the intrinsic quality characteristic $Q_s$ and the square root of the incident photon fluence (Gureyev et al. (2014b)). This product is reported as $Q'_s$ below. As the incident photon fluence was almost the same for all the images compared below, the multiplication of the intrinsic imaging quality by the square root of the fluence did not affect the comparison of the relative intrinsic quality of the images. The values of the indices obtained for iFBP and SIRT (1000 iterations) algorithms are presented in Table 5.7. Additionally, the results for the spatial resolution and SNR are shown in figures 5.11 and 5.12. The

solid lines correspond to linear fits to the data corresponding to images obtained with full phase retrieval, dashed lines correspond to images with half phase retrieval and dot-dashed lines correspond to images without the phase retrieval. Due to the large amount of the data, only results obtained inside the main lesion are presented.

**Table 5.7:** The values of no-reference objective indices for images reconstructed with iFBP and SIRT (1000 iterations) algorithms, calculated inside the lesion with full phase retrieval (phr), half phase retrieval (0.5 phr) and no phase retrieval (none).

| | | | | iFBP | | | SIRT 1000 | | |
|---|---|---|---|---|---|---|---|---|---|
| Rank of $R'\lambda$ | $R_2$ $(m)$ | E $(keV)$ | Phase retrieval | Spatial resolution $(\mu m)$ | SNR | $Q'_s \cdot 10^{-2}$ $(\mu m^{-1})$ | Spatial resolution $(\mu m)$ | SNR | $Q'_s \cdot 10^{-2}$ $(\mu m^{-1})$ |
| 1 | 0.16 | 38 | phr | 227 | 5.53 | 2.43 | 245 | 7.09 | 2.89 |
| | | | 0.5 phr | 218 | 6.53 | 3.00 | 227 | 7.15 | 3.14 |
| | | | None | 218 | 5.11 | 2.34 | 221 | 6.89 | 3.11 |
| 2 | 0.16 | 35 | phr | 224 | 5.72 | 2.55 | 245 | 7.98 | 3.26 |
| | | | 0.5 phr | 221 | 6.53 | 2.96 | 241 | 7.67 | 3.19 |
| | | | None | 217 | 5.10 | 2.35 | 235 | 7.16 | 3.04 |
| 3 | 0.16 | 32 | phr | 225 | 5.56 | 2.47 | 228 | 7.34 | 3.21 |
| | | | 0.5 phr | 221 | 6.19 | 2.79 | 224 | 7.32 | 3.27 |
| | | | None | 217 | 5.14 | 2.37 | 220 | 6.29 | 2.87 |
| 4 | 1.85 | 38 | phr | 233 | 11.81 | 5.06 | 259 | 13.12 | 5.07 |
| | | | 0.5 phr | 223 | 12.08 | 5.41 | 245 | 11.48 | 4.68 |
| | | | None | 192 | 6.80 | 3.55 | 211 | 8.43 | 3.99 |
| 5 | 1.85 | 35 | phr | 227 | 9.46 | 4.17 | 252 | 11.33 | 4.50 |
| | | | 0.5 phr | 220 | 8.47 | 3.85 | 238 | 11.02 | 4.62 |
| | | | None | 188 | 5.39 | 2.87 | 208 | 6.96 | 3.35 |
| 6 | 1.85 | 32 | phr | 233 | 9.30 | 3.99 | 248 | 11.78 | 4.74 |
| | | | 0.5 phr | 225 | 4.95 | 2.20 | 237 | 10.64 | 4.50 |
| | | | None | 192 | 6.25 | 3.26 | 208 | 7.86 | 3.78 |
| 7 | 9.31 | 38 | phr | 146 | 10.94 | 7.49 | 218 | 14.00 | 6.42 |
| | | | 0.5 phr | 142 | 7.98 | 5.62 | 217 | 10.65 | 4.91 |
| | | | None | 105 | 1.78 | 1.70 | 173 | 4.22 | 2.44 |
| 8 | 9.31 | 35 | phr | 139 | 13.51 | 9.74 | 249 | 14.81 | 5.94 |
| | | | 0.5 phr | 140 | 9.75 | 6.98 | 223 | 12.30 | 5.52 |
| | | | None | 99 | 2.74 | 2.76 | 171 | 5.12 | 2.99 |
| 9 | 9.31 | 32 | phr | 144 | 13.58 | 9.41 | 232 | 15.77 | 6.81 |
| | | | 0.5 phr | 140 | 10.69 | 7.65 | 220 | 12.48 | 5.68 |
| | | | None | 108 | 2.86 | 2.65 | 171 | 5.05 | 2.96 |

Additionally, the degree of correlation between the results from the radiological assessment and calculated objective indices was analysed. Figure 5.13 reports the values of the quality index $Q_s$ compared with the radiological score, for the images reconstructed with the TIE-Hom algorithm. For the purpose of comparison with the

radiological scores, the values of the $Q_s$ were divided by a fixed constant and shifted by another constant in order to account for the difference in the scaling, between the original scale of $Q_s$ values (0 to + $\infty$) and the (*a priori* unrelated) scale of the average radiological scores (-2 to 2). Only results for the SIRT reconstructions (with 1000 iterations) are presented in figures 5.11, 5.12 and 5.13 to avoid clutter. The trends for iFBP reconstructions were very similar.

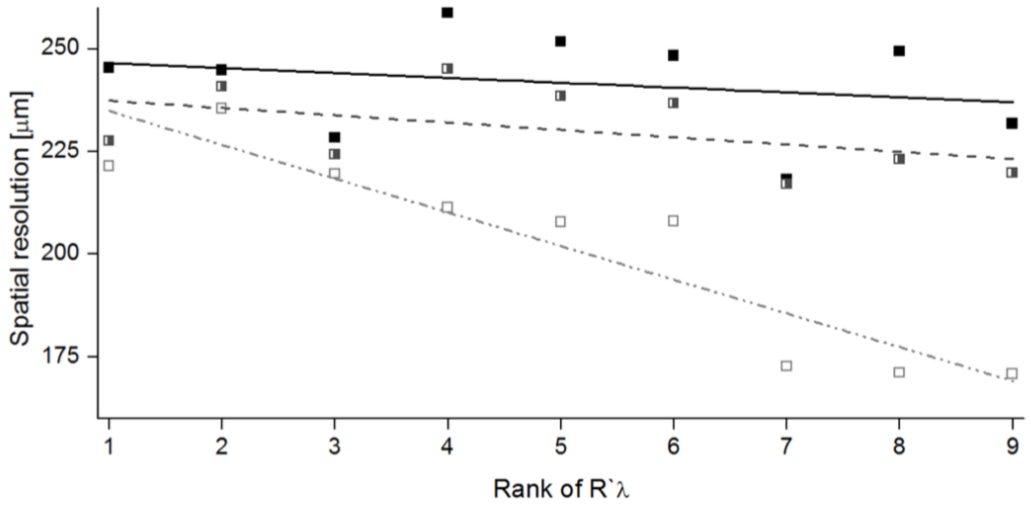


**Figure 5.11:** The values of spatial resolution measured inside the lesion for images reconstructed with SIRT (1000 iterations) algorithm with none, half (0.5 phr) and full (phr) phase retrieval.

Mammography and ultrasound examination of the breast prior to the operation, which were performed as part of a standard diagnostic procedure, are shown in figure 5.14. The mammography examination showed an oval-shaped opacity with maximum diameter of 26 *mm* (figures 5.14a and b). The change visible in mammography was classified as R5 (according to breast imaging reporting and data system (BI-RADS) (Sickles and D'Orsi (2014)) indicating a high probability of breast cancer. The ultrasound examination (Hooley et al. (2013)) revealed a solid, inhomogeneous lesion, with maximum diameter of 23 *mm* (figure 5.14c). The result of this examination was classified as U5 which also means a high probability of breast cancer.

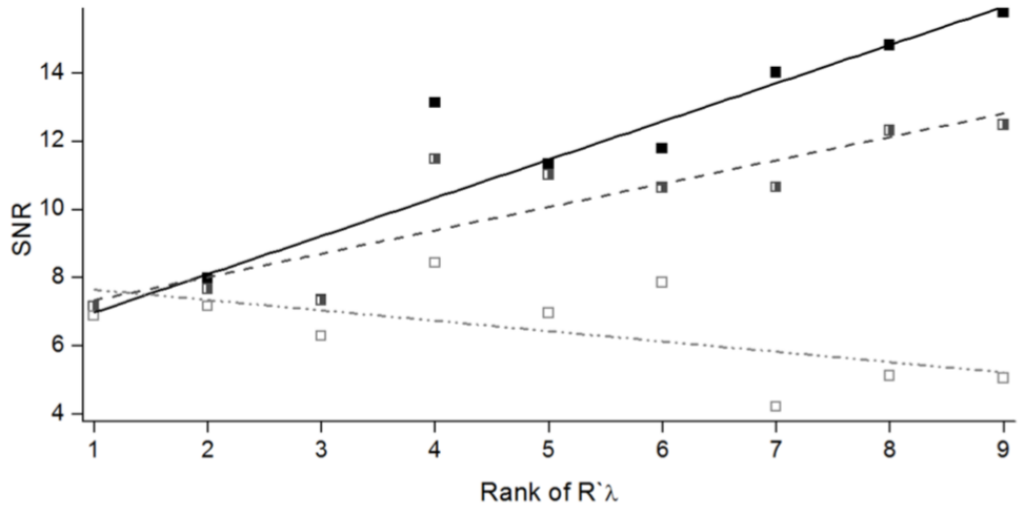


**Figure 5.12:** The values of SNR measured inside the lesion for images reconstructed with SIRT (1000 iterations) algorithm with none, half (0.5 phr) and full (phr) phase retrieval.

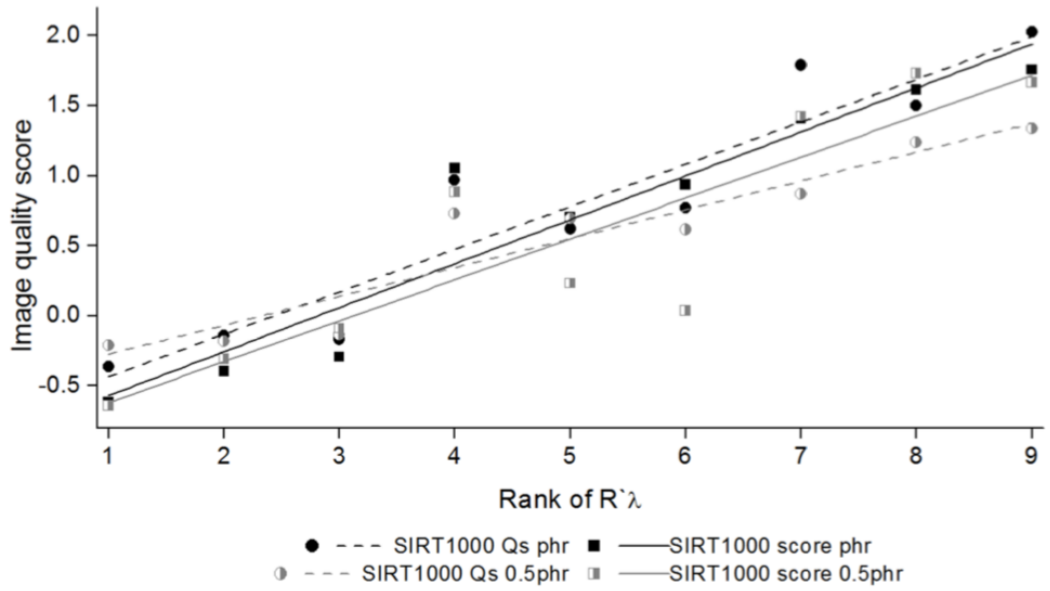


**Figure 5.13:** Correlation between the mean radiological score and the intrinsic quality characteristic ($Q_s$) for images obtained with SIRT (1000 iterations) algorithm with half (0.5 phr) and full (phr) phase retrieval.

Histological examination of the sample is a gold standard for a reliable diagnosis of cancer and gives the final determination of the type of the cancer. For histological examination, the sample was cut into several parts suited for the histology preparation. For some of these histological images, the corresponding x-ray PB-CT images

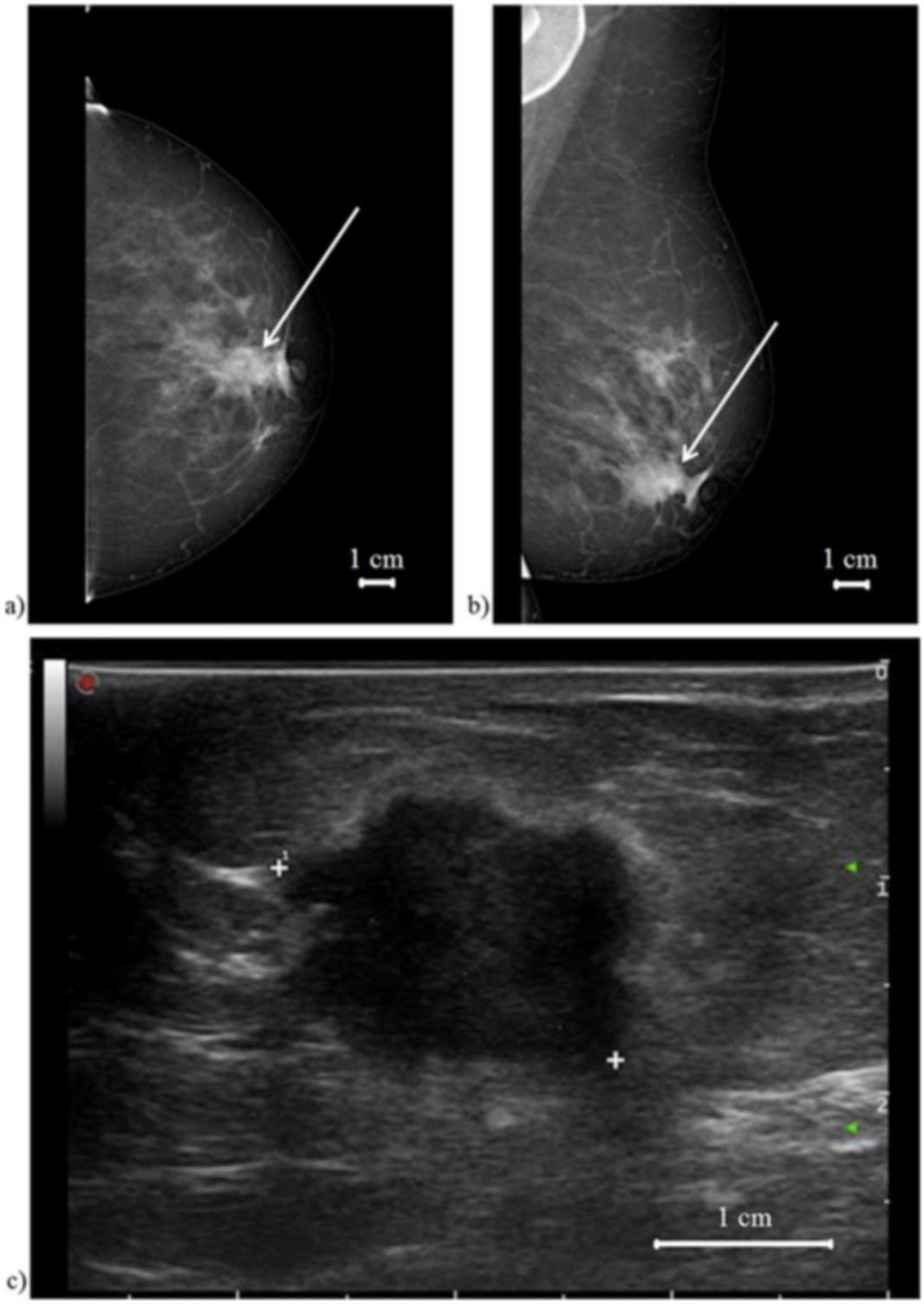


**Figure 5.14:** Mammographic and ultrasound images of the breast prior to mastectomy. (a) Digital mammography - the cranio-caudal view (CC) image; (b) Digital mammography - the mediolateral oblique view (MLO) image; (c) result of ultrasonography examination.

were identified. Comparison of three such images, which contained particularly interesting areas of the tumour and other lesions, are shown in figure 5.15 - 5.17. These images include histological sections as well as PB-CT images obtained with high and low radiation dose. The x-ray images are presented in the inverted grey-scale contrast in order to alleviate the comparison with the histological images. The high-dose images, shown in figures 5.15 - 5.17, were obtained at 9.31 $m$ propagation distance and 38 $keV$ energy using the Dalsa detector and were reconstructed using the FBP algorithm following the TIE-Hom phase retrieval with $\delta/\beta = 1083$. The low-dose images were collected with the Hamamatsu detector at 32 $keV$ energy and 9.31 $m$ distance and were reconstructed with iFBP algorithm following the TIE-Hom phase retrieval with $\delta/\beta = 870$. Both high- and low-dose images (figure 5.15) show clearly visible boundaries of the large lesion.

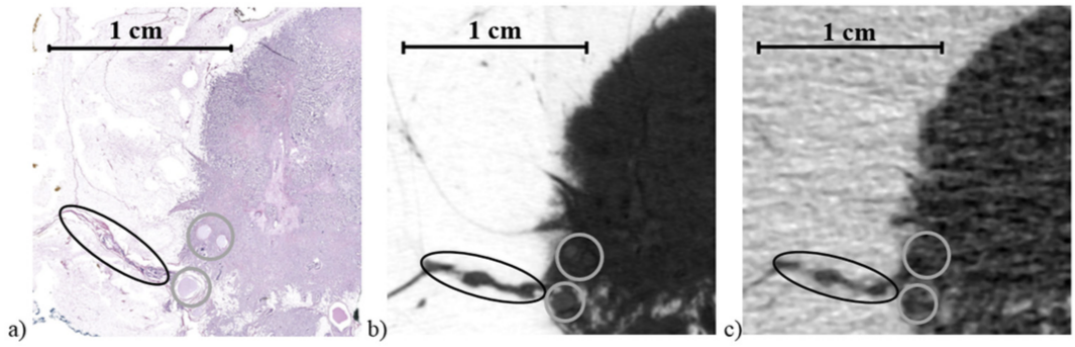


**Figure 5.15:** Images of the first part of the breast tissue sample. (a) Low-resolution histological section of the specimen. (b) High-quality phase contrast image obtained during the experiment with the dose of 1 $Gy$. (c) The best image according to radiological assessment with 4 $mGy$ dose. Black ovals show fibrous stromal septa containing cribriform pattern ductal carcinoma *in situ*; grey ovals highlight benign cysts.

The sharpness of these boundaries, more visible in figure 5.15b, is one of the features important for tumour diagnosis. Internal structures of the lesion in histological section are qualitatively comparable to the grey scale variation in the high-dose image. Additionally, some of the spiculations are clearly visible. Furthermore, one of the spicules, marked by the oval in figure 5.15 was occupied by intraductal cribriform carcinoma. In the histological section, well-defined cystic lesions, which constitute fluid- filled sacs, are presented. In high-dose x-ray image,

the cysts appear as darker (lighter, in the inverted contrast) areas with well-marked boundaries. The noise present in the low-dose image disrupts the image and makes the cysts indistinguishable.

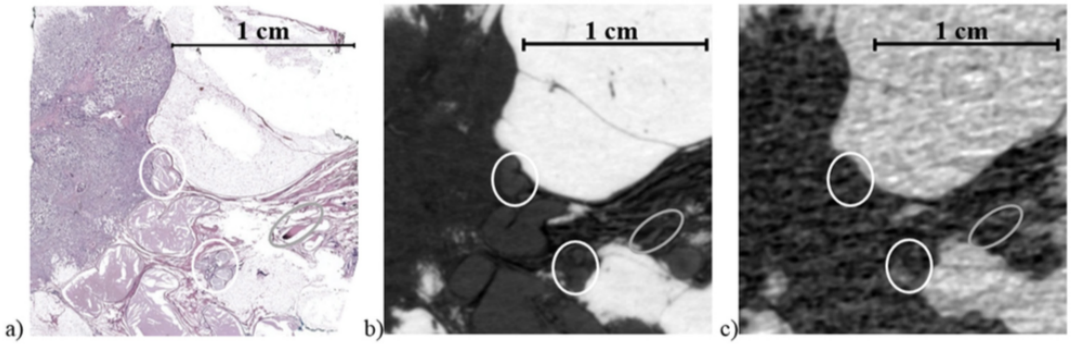


**Figure 5.16:** Images of the second part of the breast tissue sample. (a) Histological section of the specimen. (b) The best phase contrast image obtained during the experiment with 1 $Gy$ dose. (c) The best image according to radiological assessment with 4 $mGy$ dose.

The next area of the breast tissue sample shown in figure 5.16 contains the second part of the tumour, so previous comments about the margins of the lesion and the internal grey scale variation also apply. Apart from that, several large cysts with very clearly marked contours are visible in the high-dose image. Unfortunately, insufficient density difference in the low-dose image does not allow one to distinguish between the mass of the tumour and the cysts. Furthermore, blood vessels, clearly visible in the histological image, are not distinguishable in the low-dose x-ray image. The last block of the specimen (figure 5.17) contains several spiculations clearly visible in both the high and the low-dose x-ray images. Clear tissue differentiation is visible in both the histological image and the high-dose x-ray image. The most important features of this part of the sample are the suspicious areas of sclerosing adenosis. Unfortunately, these changes are not distinguishable in the x-ray images. Additionally, intraductal cribriform carcinoma area is visible in this part of the breast specimen.

Analysis of the data contained in Table 5.7 and in figures 5.11 - 5.13 shows that, for images reconstructed with TIE-Hom algorithm, SNR, intrinsic image quality, $Q_s$,

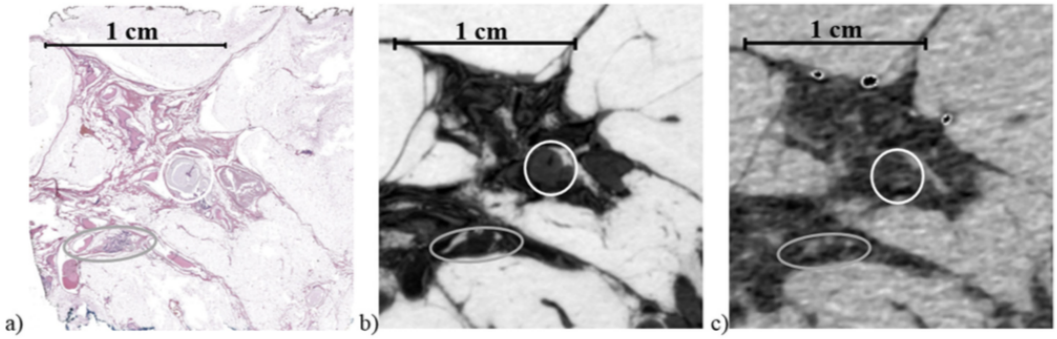


**Figure 5.17:** Images of the third part of the breast tissue sample. (a) Histological section of the specimen. (b) The best phase-contrast image obtained during the experiment with 1 $Gy$ dose. (c) The best image according to radiological assessment with 4 $mGy$ dose. White ovals contain micropapillary pattern ductal carcinoma *in situ*, grey ovals contain areas of sclerosing adenosis.

and the average radiological scores were all increasing according to the rank of the 'phase-contrast parameter' ($R'\lambda$), while the spatial resolution remained relatively constant. In particular, the obtained radiological scores were consistently higher for the images collected with higher values of the phase-contrast parameter, in comparison with the reference image (which corresponded to the highest-quality reconstruction obtained without the phase contrast) at the same radiation dose. For larger sample-to-detector distances, the differences between the SNR value for the images with and without the application of the TIE-Hom phase retrieval algorithm became larger (up to 5 fold for $R_2 = 9.31\ m$). The same trend was observed in the case of the intrinsic imaging quality, where the best results were achieved for the highest rank of $R'\lambda$. Comparison of the objective indices for images collected at the same propagation distance, clearly showed the advantage of using the TIE-Hom algorithm compared to images reconstructed without phase retrieval, except for the lowest sample- to-detector distance where no obvious trend was found (the latter result was expected, as the degree of phase contrast in the projections collected at the shortest propagation distance was quite small). Moreover, at a fixed propagation distance, the best results were achieved in the present study for the lowest photon energy used, E = 32 $keV$. These results are in a good agreement with the previous theoretical and experimental results of x-ray phase contrast imaging (Keyriläinen

et al. (2011); Coan et al. (2013); Bravin et al. (2013); Gureyev et al. (2014a,b)). The validity of the representation by the obtained PB-CT images of some important morphological aspects of the breast tissue sample were confirmed by means of direct comparison with histological images (figures 5.15 - 5.17). Important features which define the lesions (sharpness of tumour boundaries or visibility of spiculations) could be clearly seen in both high and low- dose images. Some fine details inside the lesion, such as cystic lesions or ducts were visible only in high-dose x-ray images. Unfortunately, because of the excessive dose, these high-dose images can be obtained only for excised samples, and not for live patients. The present study was based on the analysis of a single tissue sample. However, it can be stated with confidence, based on other experiments and simulation studies using similar imaging techniques which involved many breast tissue samples with different types of tumours (

## 5.5 Objective quality indexes

The aim of this third approach was to quantitatively analyse different factors affecting image quality in x-ray phase- contrast breast tomography. The experiments were performed at the SYRMEP beamline of the Elettra light source utilising propagation-based phase-contrast. A specially designed polycarbonate phantom filled with different reference materials and breast tissues specimens was scanned varying: sample-to-detector distance, x-ray energy, reconstruction algorithm and delivered mean glandular dose. The image quality of the reconstructed images was quantitatively assessed measuring the variance of noise, Contrast-to-Noise ratio (CNR), edge sharpness and additional indices that incorporate the delivered dose. The influence of each factor was systematically evaluated, while the others were kept constant. We show that best results are obtained if phase-contrast is used effectively by applying larger propagation distances and phase retrieval algorithms. The application of phase retrieval greatly enhances CNR but generates edge blurring that increases with increasing $\delta/\beta$ ratio. In addition, we show that, if optimised acquisition parameters are used, it is possible to achieve a good

image quality at very low radiation doses, which will enable clinical application of phase-contrast breast CT.

### 5.5.1 Materials and methods

*Data acquisition*

To address image quality a polycarbonate phantom (Fig. 5.18) with a diameter of 8 $cm$ containing 7 holes was used. Four holes were filled with formalin 10% (5.18-1), paraffin (5.18-2), glycerol (5.18-3) and $EtOH$ (5.18-4) and three additional holes with human breast tissue specimens fixed in formalin (5.18-5-6-7). The phantom was imaged at three different energies: 32, 35 and 38 $keV$, in in-line (propagation-based, PB) mode using four different levels of photon statistics (i.e. four different radiation doses), this was achieved through the use of $Al$ filters of varying thicknesses (5.25, 8 and 12 $cm$), keeping constant the exposure time. The CT scans were collected at three different sample-to-detector distances: R = 0.16, 1.85 and 9.31 $m$. Each scan contained 2000 projections collected with 0.18°angular step over 360°.The scans were performed using a Hamamatsu CMOS Flat Panel Sensor C9252DK-14 (pixel size 100 $\mu m$).

*CT reconstruction procedure*

The followed reconstruction procedure is quite similar to the one used in the previous described study, however, for the sake of completeness, it is here reported. For data pre-processing, phase retrieval and reconstruction the software "SYRMEP tomo project" STP (Brun et al. (2015)) was used. The pre-processing of projection images contained the following steps:

1. dark current correction of projections and of the flat-field images,
2. flat-field correction to correct for inhomogeneities in the illumination,
3. optional application of phase retrieval using the Homogeneous Transport of Intensity equation (TIE-Hom) algorithm (Paganin et al., 2002),

4. Rivers ring artifact removal (`http://www.mcs.anl.gov/research/projects/X-ray-cmt/rivers/tutorial.html`)

5. image reconstruction using different algorithms: standard Filtered Back Projection (FBP), Simultaneous Iterative Reconstruction Technique (SIRT) (van der Sluis and van der Vorst (1990)), Simultaneous Algebraic Reconstruction Technique (SART) (Gordon et al. (1970)), Conjugate Gradient Least Square method (CGLS) (van der Sluis and van der Vorst (1990)), and Minimum Residual Filtered Back Projection method (MR-FBP) (Pelt and Batenburg (2014)).

Single distance phase retrieval algorithm such as the used TIE-Hom need as a-priori information the so called $\delta/\beta$ ratio, whereas $\beta$ denotes the absorption and $\delta$ the phase shift in the complex refractive index. As in the previous study, two different values of $\delta/\beta$ ratio have been used. The first was close to the theoretical value of glandular tissue in adipose tissue ($\delta/\beta = 870, 978, 1083$ for 32, 35 and 38 $keV$ respectively). The second was set to half of the first one to consider a "partially phase retrieved" image, representing a mixture of the raw phase-contrast image, and the phase-retrieved image, that has proven to provide images that are appreciated by human observers. (Baran et al. (2017); Paganin et al. (2002) TS-imaging website).

*Quantitative assessment*

The presented analysis is divided into four different sections, each analysing the influence of a single parameter on the quality of the reconstructed images. The considered aspects are:

- sample-to-detector distance
- energy of the incident x-ray beam
- reconstruction algorithm
- radiation dose

For each section, i.e. each combination of acquisition and reconstruction parameters, image quality was quantitatively assessed evaluating different image characteristics such as contrast, noise and edge sharpness. Contrast-to-Noise ratio as defined in eq. 5.2. Edge sharpness was evaluated by fitting a sigmoid function in profiles of the interface between adipose and fibrous tissue (Mohammadi et al. (2014)), calculating the derivative of this function (a Gaussian) and measuring the full width at half maximum value (FWHM) (Fig. 5.18). Both metrics (CNR and edge sharpness) were calculated five times in five different positions. To further validate the obtained results, with a feature independent method, a power spectra analysis of all details containing tissue in figure 5.18 was carried out. This method was proven to be feature independent and the results were in good agreement with the previous ones. Details of this latter analysis can be found in the next section.

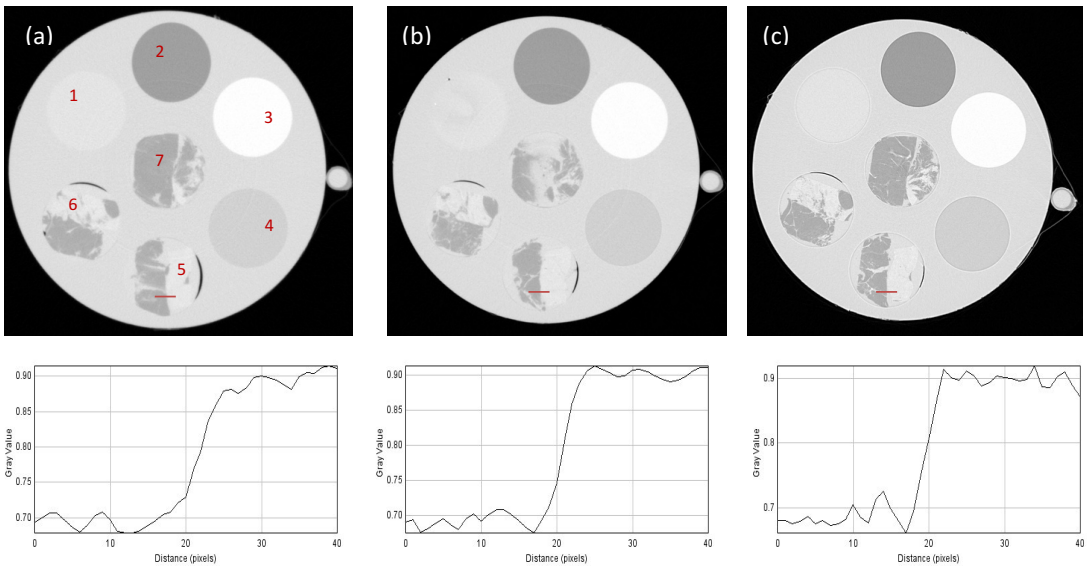


**Figure 5.18:** Reconstructed axial CT slices of the polycarbonate phantom acquired at 38 $keV$ and the sample-to-detector distance of 0.16 $m$ (a), 1.85 $m$ (b), 9.31 $m$ (c) and related line profiles (along the line shown in red) across the boundary between the adipose and fibrous tissues. Phase-contrast effect starts to be visible in the 1.85 $m$ distance image and becomes prominent in the 9.31 $m$ one.

In addition to incorporate the dose level, a figure of merit (FoM), corresponding to the CNR normalised by the x-ray dose ($D_{abs}$ and, hence, by the photon flux) was computed.

$$FoM = \frac{CNR}{\sqrt{D_{abs}}} \tag{5.4}$$

### 5.5.2 Results and discussion

The described objective image quality metrics assess separate features of the images, and therefore need to be evaluated in parallel to give an overall representation of the image quality. How these parameters, edge sharpness and noise in particular, are balanced is dependent on the selected scanning protocol and the image reconstruction procedure. Concerning the resolution, there are three contributions to it in the reconstructed CT volume: 1) intrinsic resolution of the imaging system quantified by the effective source size and detector resolution in the object plane, 2) TIE-Hom phase retrieval which acts as a low-pass filter, in individual projections, and 3) CT reconstruction algorithm. It is the non-linearity of the reconstruction algorithm that introduces the dependence of the resolution on the variance of noise (namely, noise is suppressed more strongly at the edges having greatest contrast). Starting from this assumption and following the approach described in (Verdun et al. (2015)), where a correlation between noise characteristics and FWHM is discussed, an empirical analysis of the relationship between noise and edge quality was carried out for each experimental condition and for each considered reconstruction algorithm. Several values of FWHM were ob- tained by phase retrieving data using increasing $\delta/\beta$ ratio (increasing this ratio in TIE-Hom phase retrieval increases the image smoothness, thus increasing the FWHM). These FWHM values were plotted as a function of the corresponding level of noise and the power of the fitting curve ($n$) was recorded. The strongest variability of this relationship was found, as expected, when comparing different reconstruction algorithm as they use different filters to perform the reconstruction (e.g. strong smoothing or strong edge enhancing filter). In particular, it was found that the empirical relationship between FWHM and noise was accurately fitted using the power function $\sigma \sim 1/(FWHM)^n$, with the value

of $n$ varying between 1.4 and 2.5 for different reconstruction algorithms. Based on the described approach, an image quality index was defined as:

$$IQ = \frac{FoM}{FWHM^n} \tag{5.5}$$

where $n$ corresponds to the power found for each reconstruction algorithm. Results were compared with the power spectra analysis and it was found a good agreement between the two methods. Since $IQ$ is independent by the chosen $\delta/\beta$ ratio, this type of image quality can be applied in various applications in addition to phase-contrast imaging in breast tissue described here. As previously mentioned, the work is divided in four sections, the first and the second one of these, aim to find the optimum value of sample-to-detector distance and energy, that maximise the image quality (in terms of $IQ$). Once the optimal distance and energy are established, the third section aims to understand which reconstruction algorithm gives the best results, achieving the best compromise between contrast-to-noise level and edge quality (spatial resolution expressed as FWHM). The purpose of the last section is to evaluate the relationship between image quality and decreasing levels of the radiation dose. As in the previous tests, line profiles at interfaces of adipose and fibrous tissue were considered, focusing on the evaluation of the variations in the slope in correlation with decreasing levels of photon statistics (i.e. decreasing levels of the dose). It has been proven, that the optimisation of the experimental and reconstruction parameters gives the same results independently by the order in which it is was conducted. "Idealised" conditions have also been considered, meaning the potential use of an evacuated pipe to transfer the transmitted x-ray beam from the sample to the detector. This would avoid additional x-ray attenuation in air and therefore reduces the dose level (considering the same image quality). To simulate this condition, $IQ$ for data sets acquired at 1.85 and 9.31 $m$ are calculated using the radiation dose corresponding to the dose measured at the detector position considering just the geometrical setup and omitting the attenuation due to the air in the path between sample and detector.

**Table 5.8:** Values of CNR and FWHM for FBP reconstructed data acquired at R = 0.16, 1.85 and 9.31 $m$ distance at 38 $keV$ with and without phase retrieval. In order to compare the FWHM images were resized according to the cone angle of the setup of 7 $mrad$.

| | no phr | | $\delta/\beta = 542$ | | $\delta/\beta = 1083$ | |
|---|---|---|---|---|---|---|
| | CNR | FWHM [pixel] | CNR | FWHM [pixel] | CNR | FWHM [pixel] |
| **R = 0.16** $m$ | 15.89 ± 0.22 | 4.42 ± 0.45 | 16.84 ± 0.26 | 4.48 ± 0.45 | 17.61 ± 0.29 | 4.53 ± 0.45 |
| **R = 1.85** $m$ | 6.45 ± 0.18 | 4.25 ± 0.52 | 25.42 ± 0.45 | 4.55 ± 0.45 | 29.91 ± 0.55 | 4.81 ± 0.41 |
| **R = 9.31** $m$ | 11.19 ± 0.04 | 1.79 ± 0.35 | 32.47 ± 0.11 | 2.98 ± 0.26 | 43.49 ± 0.22 | 3.67 ± 0.24 |

*A. Sample-to-detector distance*

Three datasets acquired with an energy of 38 $keV$ and at a sample-to-detector distance R = 0.16, 1.85 and 9.31 $m$ were studied. Table 5.8 shows the results for reconstructions obtained with classical FBP algorithm, without and with phase retrieval using the two different values of $\delta/\beta$ ratio. This ratio, at nominal and half value affects both CNR and FWHM depending on the distance: at larger distances both the increment of contrast-to-noise ratio and the blurring effect increases for higher $\delta/\beta$ ratio. As the imaging setup has a cone angle of 7 $mrad$, the images collected at R = 1.85 and R = 9.31 $m$ were de-magnified to match the size of the one obtained at R = 0.16 $m$. The CNR was measured in the original data sets.

In order to evaluate both CNR and FWHW together whilst accounting for delivered dose, the relationship displayed in eq. 5.5 was calculated (see Fig. 5.19), where $n = 1.9$ is the parameter found for FBP algorithm at 38 $keV$. Thus, in the following we consider a higher IQ equal to higher image quality. In addition, also the curves under assumed ideal conditions (i.e. x-ray beam transported in vacuum from the sample to the detector to avoid air attenuation) are shown. As all curves start from about the same value it can be concluded that phase retrieval has almost no effect on acquisition in quasi- contact regime dominated by absorption based contrast. If no phase retrieval is used (purple curves), image quality remains approximately constant for between 0.16 $m$ and 1.85 $m$ and then increases.

That means the low CNR for the 9.31 $m$ images is over-compensated by a higher edge quality. Phase retrieved data with both half and nominal $\delta/\beta$ ratio shows a

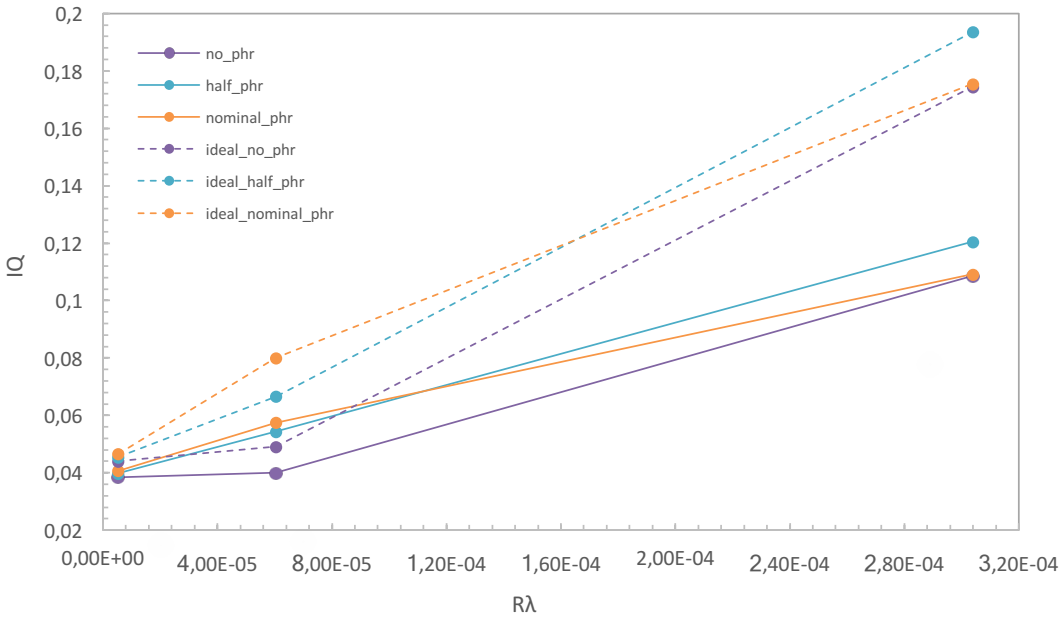


**Figure 5.19:** $IQ = FoM/FWHM^n$ trend with growing $R\lambda$ for images processed with and without phase retrieval. Both real (solid lines) and ideal case (dashed lines) are shown. Note that, only $R$ (the sample-to-detector distance) is varying while $\lambda$, so the energy was kept constant ($\lambda$ is defined as $hc/E$). The parameter $n$ is derived from the analysis of the relationship between noise and FWHM, the value is the one related for 38 $keV$ and FBP reconstruction method ($n = 1.9$).

gain in image quality monotonically increasing with sample- to-detector distance. At 1.85 $m$ the highest quality is reached at the nominal $\delta/\beta$ ratio. In contrast, at 9.31 $m$ phase retrieved images with half the nominal $\delta/\beta$ value show a higher image quality. In an ideal case (with no x-ray absorption in air between the sample and the detector), there is a gain in quality of about 20% for images acquired at 1.85 $m$ and 60% for images acquired at 9.31 $m$, indicating the importance of eliminating x-ray absorption in air for long sample-to-detector distances.

*B. Energy*

In this section, reconstructions of data sets obtained at R = 9.31 $m$ using three different energies (32, 35 and 38 $keV$) are evaluated. Table 5.9 shows results for images reconstructed with and without phase retrieval. The value of CNR (lower for 32 $keV$ images) could be seen as an anomalous behaviour since a lower energy should give rise to a higher contrast level due to the higher x-ray absorption.

Nevertheless, it has to be underlined that CNR is a metric that involves also a measure of the noise, so since it was found that 32 $keV$ images were affected by a very high noise level, this trend could be considered as coherent. In all cases, we observed a loss in edge sharpness if phase retrieval was applied. This loss as well as the CNR, increases with increasing value of $\delta/\beta$. In Fig. 5.20 all curves display approximately the same trend.

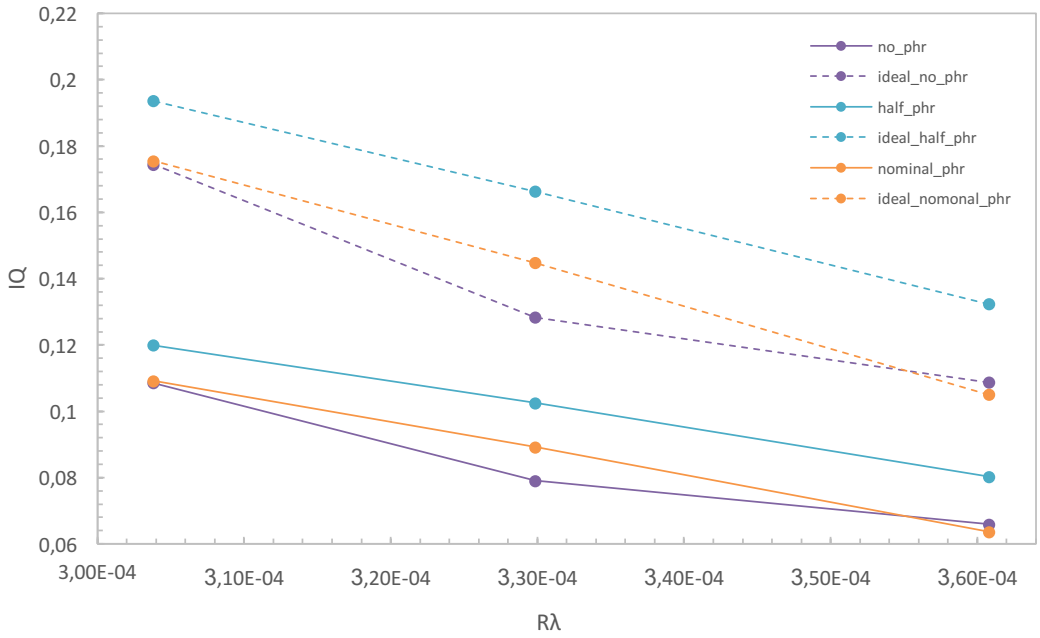


**Figure 5.20:** Evaluation of $IQ$ in dependency of increasing $R\lambda$. The $n$ parameter is the one found for FBP, i.e. 1.9 for all energies. Curves are related to images reconstructed starting from dataset acquired at 32, 35 and 38 $keV$. In this case $\lambda$ is the changing parameter while $R$ was kept constant.

They show a higher $IQ$ at higher energy and decrease towards lower energy. For all energies, the quality reaches its maximum (i.e. the best compromise between dose, CNR and edge sharpness) using the half of the nominal value of $\delta/\beta$. The difference between real and ideal case is constant for all energies, in ideal conditions there is a gain between 60 and 65%.

*C. Reconstruction method* In this section, different reconstruction algorithms are evaluated. Table 5.10 shows CNR and FWHM for reconstructions obtained without phase retrieval and with phase retrieval using two different levels of $\delta/\beta$. It can be

**Table 5.9:** Values of CNR and FWHM for images acquired at 9.31 $m$ distance and 32, 35 and 38 $keV$ and reconstructed with FBP algorithm. Same indices are calculated for reconstructions obtained with and without phase retrieval. As the $\delta/\beta$ ratio is energy dependent, the nominal value is 1083, 978 and 870 for 38, 35 and 32 $keV$ respectively.

| | no phr | | Half $\delta/\beta$ | | Nominal $\delta/\beta$ | |
|---|---|---|---|---|---|---|
| | CNR | FWHM [pixel] | CNR | FWHM [pixel] | CNR | FWHM [pixel] |
| **E = 32** $keV$ | 7.52 ± 0.03 | 1.76 ± 0.44 | 21.86 ± 0.13 | 2.77 ± 0.31 | 29.56 ± 0.17 | 3.41 ± 0.31 |
| **E = 35** $keV$ | 10.78 ± 0.06 | 2.05 ± 0.43 | 29.6 ± 0.29 | 3.05 ± 0.53 | 37.48 ± 0.17 | 3.73 ± 0.53 |
| **E = 38** $keV$ | 11.18 ± 0.04 | 1.79 ± 0.35 | 32.47 ± 0.11 | 2.98 ± 0.26 | 43.49 ± 0.22 | 3.67 ± 0.24 |

**Table 5.10:** Values of CNR and FWHM for images acquired with an energy of 38 $keV$ and at a sample-to-detector distance of 9.31 $m$ reconstructed with five different algorithms.

| | no phr | | $\delta/\beta$ = 542 | | $\delta/\beta$= 1083 | |
|---|---|---|---|---|---|---|
| | CNR | FWHM [pixel] | CNR | FWHM [pixel] | CNR | FWHM [pixel] |
| **SIRT** | 16.16 ± 0.08 | 2.17 ± 0.25 | 39.17 ± 0.12 | 3.14 ± 0.21 | 50.21 ± 0.31 | 3.79 ± 0.24 |
| **MR-FBP** | 10.1 ± 0.05 | 1.44 ± 0.42 | 29.65 ± 0.08 | 2.6 ± 0.29 | 41.22 ± 0.41 | 3.33 ± 0.3 |
| **FBP** | 11.19 ± 0.04 | 1.79 ± 0.35 | 32.46 ± 0.11 | 2.98 ± 0.26 | 43.49 ± 0.22 | 3.67 ± 0.24 |
| **SART** | 7.83 ± 0.05 | 1.59 ± 0.31 | 19.77 ± 0.11 | 2.74 ± 0.14 | 25.55 ± 0.32 | 3.5 ± 0.25 |
| **CGLS** | 27.91 ± 0.06 | 3.63 ± 0.17 | 46.8 ± 0.12 | 4.65 ± 0.24 | 53.6 ± 0.44 | 5.27 ± 0.26 |

seen that the application of the CGLS algorithm leads to the highest CNR but at the same time to the lowest edge quality. Varying $\delta/\beta$ ratios affect CNR and FWHM similar in all algorithms. Despite that, when considering the overall image quality (Fig. 5.21), i.e. the best compromise between contrast to noise ratio and edge quality, a series of difference has been observed. In Fig. 5.21 all algorithms except CGLS show similar high $IQ$ values, maximal if half of the nominal $\delta/\beta$ ratio is applied. The already strong blurring observed in CGLS reconstructed images yields to low $IQ$ values that in contrast to the other algorithm decrease if phase retrieval is applied.

MR-FBP and SIRT (both with half phase retrieval applied) are the algorithms that results in the highest $IQ$. The considered algorithms use different processing filters therefore the relationship between noise and FWHM is non-linear and shows strong differences, as seen by the differences in the calculated n values (from 1.4 for SART to 2.5 for CGLS).

*D. Dose*

Based on previous results, in which a sample-to-detector distance of R = 9.31

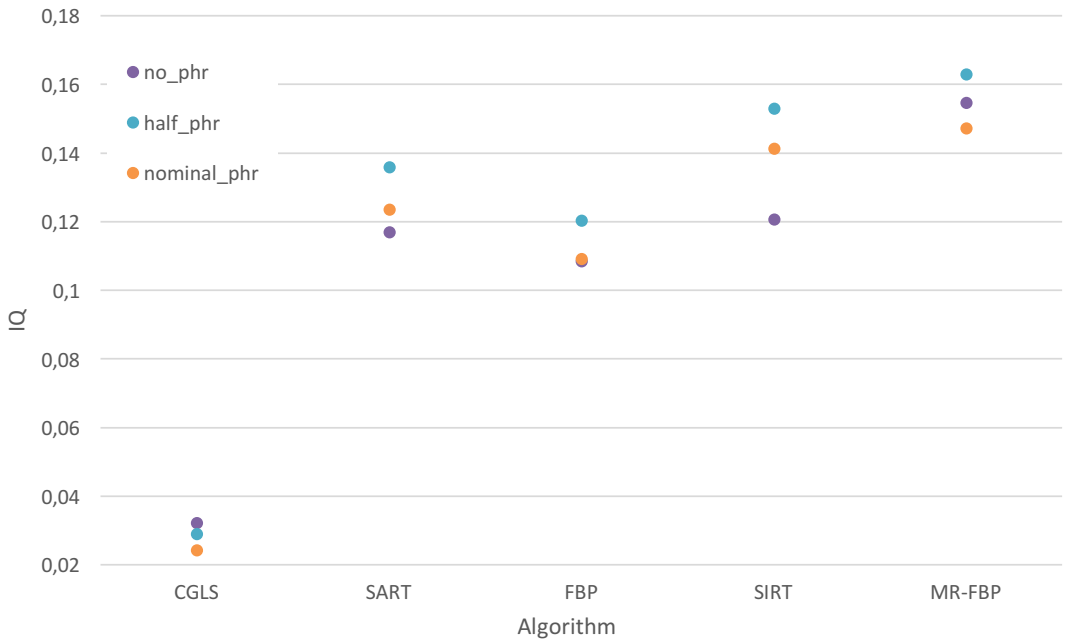


**Figure 5.21:** *IQ* value for dataset acquired at 9.31 *m*, at the energy of 38 *keV* and reconstructed with different reconstruction methods. The n parameter values are: 2.5 for CGLS, 1.4 for SART, 1.9 for FBP and 1.7 for SIRT and MR-FBP. The dose level is considered just to keep the same order of magnitude of *IQ* as previous cases, but clearly it is constant for all reconstructions.

*m* and an energy of 35 *keV* was found optimal, in this chapter the influence of decreasing dose levels onto image quality under that condition is evaluated. Fig. 5.22 displays line profiles for the interface between adipose and fibrous tissue. Despite the increasing noise level while lowering the x-ray dose, no apparent changes in the shape of the edge profiles can be found, indicating that, in our case, dose does not affect the edge quality. Table 5.11 reports CNR and FoM values for the different level of photon statistics for real and ideal case.

Due to the increasing noise level, the CNR is lower for lower doses. Phase retrieved data show the highest values for both CNR and FoM. Furthermore, it can be also noticed that for *medium*, *low* and *very low* statistics the figure of merit keeps, as expected, approximately the same value, this is because image quality decreases with lower dose, but the FoM is normalised by the square root of the dose, so at very low statistics it is still possible to produce images with an acceptable quality. This is not maintained for the high dose images because the dose is too

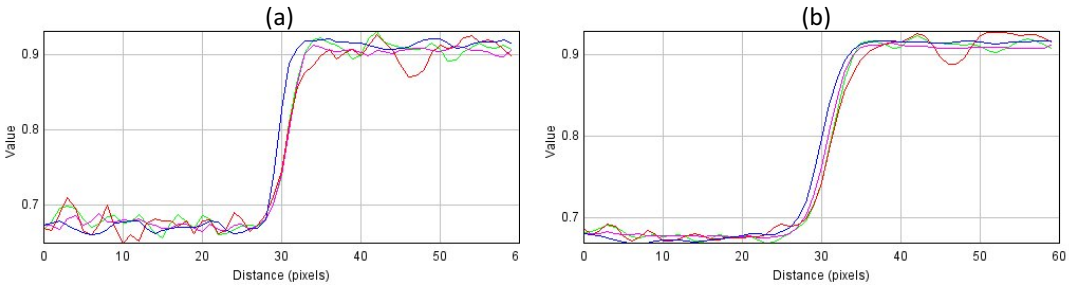


**Figure 5.22:** Line profiles across the boundary between adipose and fibrous tissue for images reconstructed without phase retrieval process (a) and with phase retrieval using the nominal value of $\delta/\beta$ (b). Each profile corresponds to a different photon statistics. Blue, pink, green and red curves correspond to high, medium, low and very low statistics respectively.

**Table 5.11:** Values of CNR and FoM for images acquired at 35 $keV$ with different photon statistics for real and ideal case for 9.31 $m$ distance and classical FBP reconstruction method. Same indices are calculated for reconstructions obtained with and without phase retrieval. To further decrease doses, for medium, low and very low dataset, only 1000 projections were used for reconstruction (over 180°).

| | | | no phr | | $\delta/\beta = 489$ | | $\delta/\beta$= 978 | |
|---|---|---|---|---|---|---|---|---|
| | DOSE [mGy] | IDEAL DOSE [mGy] | CNR | FoM | CNR | FoM | CNR | FoM |
| **HIGH** | 1246.85 | 473.74 | 10.79 ± 0.06 | 0.31 | 29.59 ± 0.29 | 0.93 | 37.48 ± 0.17 | 1.22 |
| **MEDIUM** | 27.12 | 10.3 | 3.61 ± 0.03 | 0.78 | 10.22 ± 0.12 | 2.48 | 14.45 ± 0.2 | 3.48 |
| **LOW** | 13.28 | 5.05 | 2.7 ± 0.03 | 0.7 | 7.49 ± 0.11 | 2.32 | 10.16 ± 0.12 | 3.3 |
| **VERY LOW** | 5.71 | 2.17 | 1.22 ± 0.03 | 0.67 | 4.57 ± 0.09 | 2.34 | 6.32 ± 0.12 | 3.21 |

high to further improve the CNR. In addition, the difference between real and ideal case is constantly around 62% for all doses.

### 5.5.3 Power spectra analysis

The content of an image can be understood as a weighted sum of spatial harmonical components (waves). The 2D Fourier transform calculates the values of the corresponding weights at different spatial frequencies. The power spectrum is proportional to the square of the absolute value of the 2D Fourier transform normalised by the size of the analysed image and thus it represents the intensity of a certain frequency within the image. Images with steeper edges will contain higher intensities in the frequency band that describes the edge. Random noise dominates at high frequency variations within the image. Therefore, the intensity in the cut-off

region of the spatial frequencies is related to the noise level of the image. Overall, images with a higher sharpness (meaning sharper edges) and a lower noise level should demonstrate in comparison with images of lower quality, higher power in the medium to high frequency band and lower power at the cut-off frequency. In order, to analyse the data independently from the orientation of the edges within the images we present the radial averaged power spectra. The analysis was made selecting three different areas of the image containing an edge between adipose and fibrous tissue and one area of the same size in the background (made of polycarbonate) used as a measure of pure noise. The selected areas are shown in fig. 5.23.

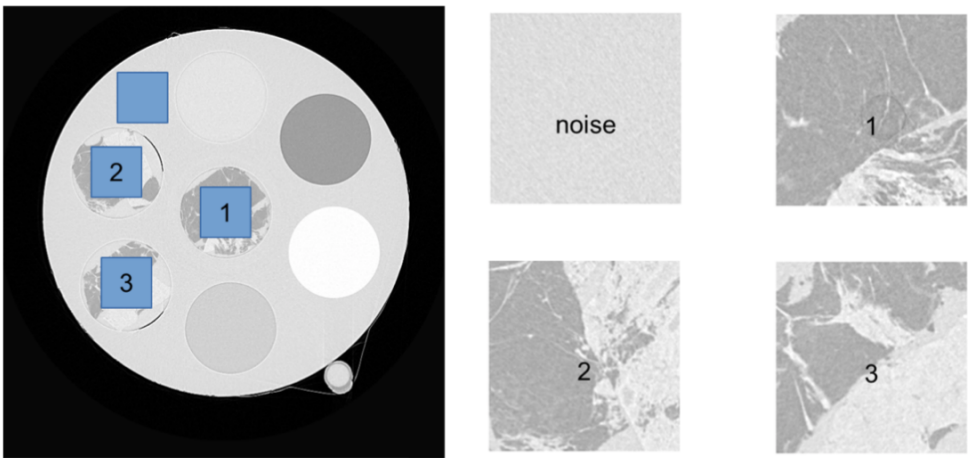


**Figure 5.23:** Polycarbonate phantom of 8 *cm* diameter containing 7 holes filled with different materials (i.e. paraffin, formalin 10%, glycerol and $EtOH$) and breast tissues. The highlighted areas are the ones used for the power spectra measurements.

The measurements were done on images reconstructed with five algorithms (FBP, SIRT, SART, MR- FBP and CGLS) and with an increasing level of phase retrieval filter (i.e. no phase retrieval applied, phase retrieval applied with the half, the nominal and the double of the nominal $\delta/\beta$ ratio). Results are shown in the following figures. The more the curves keep high intensities at middle and high frequencies, the sharper is the image. Considering this, the MR-FBP algorithm is the one that produces the sharpest images, then SART, FBP, SIRT and CGLS. Noise curves have different shapes, meaning the algorithms have a different noise structure. CGLS has the lowest level of noise while SART has the highest one.

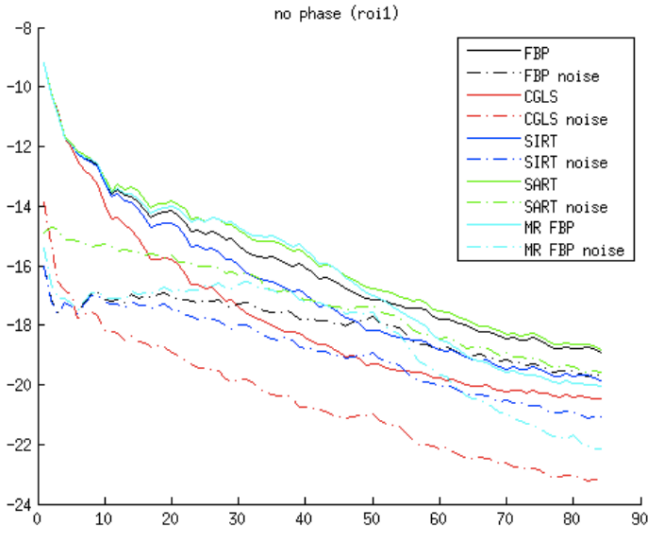


**Figure 5.24:** Comparison between different reconstruction algorithms. Solid lines represent the power spectra of the tissue detail (signal + noise) while the dashed lines are related to the pure noise measured on the polycarbonate matrix.

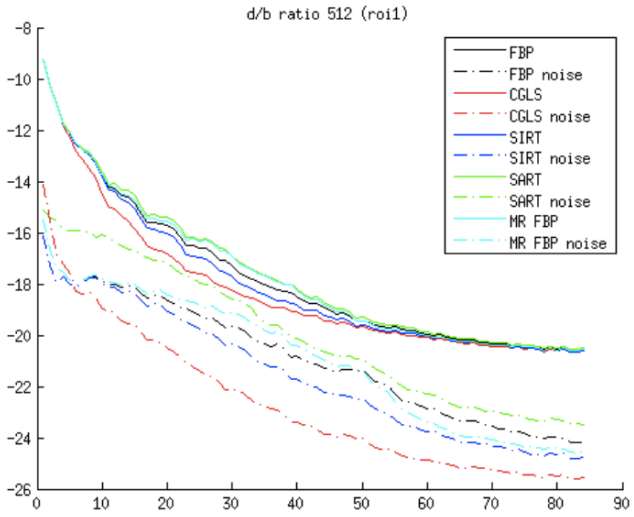


**Figure 5.25:** Comparison between different reconstruction algorithms. All images are processed with phase retrieval filter using the half of the nominal $\delta/\beta$ ratio. Solid lines represent the power spectra of the tissue detail (signal + noise) while the dashed lines are related to the pure noise measured on the polycarbonate matrix.

SIRT and FBP have similar behaviour, MR-FBP keeps a high level of noise in a central frequency band and then decreases at higher frequencies.To find the relationship between noise and sharpness we calculated and plotted the integral of the curves of the pure noise versus the integral of the curves related to the signal

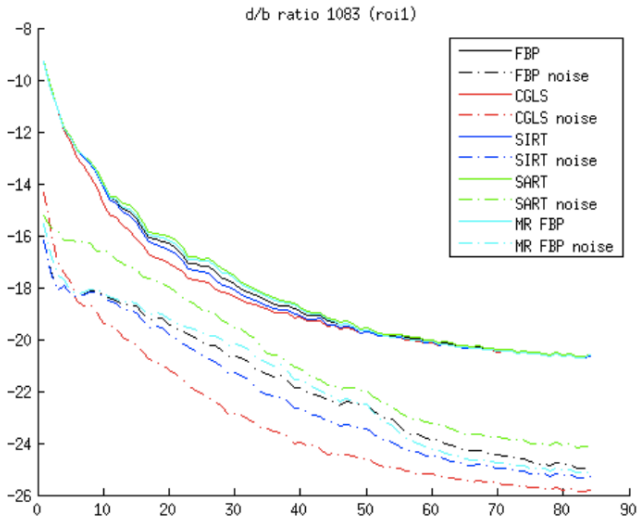


**Figure 5.26:** Comparison between different reconstruction algorithms. All images are processed with phase retrieval filter using the nominal $\delta/\beta$ ratio for adipose and fibrous tissue. Solid lines represent the power spectra of the tissue detail (signal + noise) while the dashed lines are related to the pure noise measured on the polycarbonate matrix.

**Table 5.12:** Power of the fitted curve obtained with the power spectra method and with the FWHM vs noise method. This latter is the one used in the study.

| | Power Spectra method | FWHM vs Noise method |
|---|---|---|
| FBP | 1.85 | 1.88 |
| MR-FBP | 1.80 | 1.74 |
| SART | 1.48 | 1.43 |
| CGLS | 2.04 | 2.50 |
| SIRT | 1.80 | 1.75 |

plus noise. As done for the FWHM and the variance of the noise, we fitted the points with a power function and recorded the power of the fitting curve. It has to be noticed that with this second method it is not possible to focus on one precise edge (i.e. the one between fat and fibrous tissue) and this explains the difference of the n power between the two methods. Results are shown in Table 5.12.

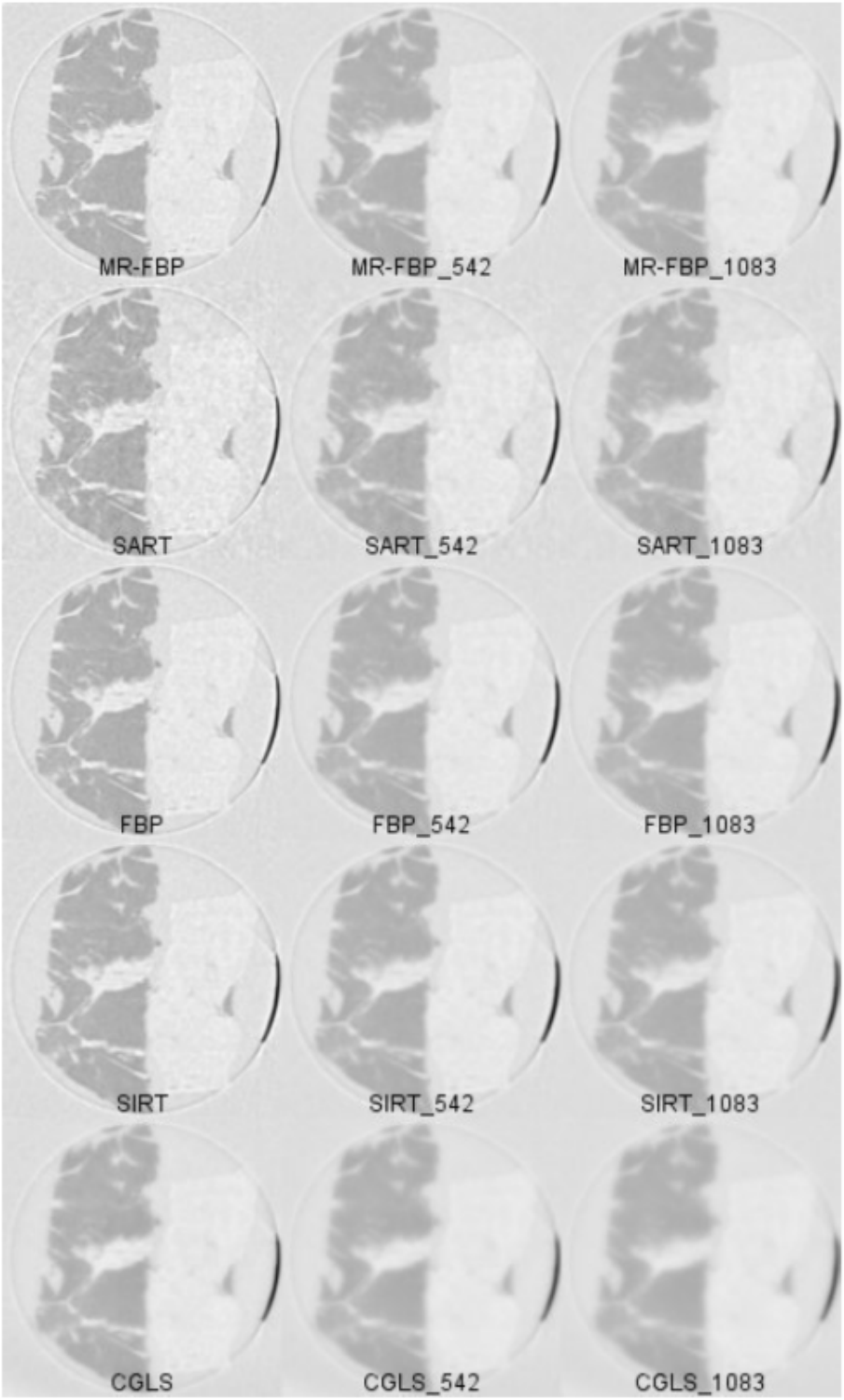


**Figure 5.27:** Details reconstructed with different algorithms and processed with increasing level of phase retrieval. Top to bottom images with decreasing level of sharpness, left to right images processed without, with half and with nominal value of $\delta/\beta$ ratio.

# References

Baran, P., Pacile, S., Nesterets, Y., Mayo, S., Dullin, C., Dreossi, D., Arfelli, F., Thompson, D., Lockie, D., McCormack, M., Taba, S., Brun, F., Pinamonti, M., Nickson, C., Hall, C., Dimmock, M., Zanconati, F., Cholewa, M., Quiney, H., Brennan, P., Tromba, G., Gureyev, T., 2017. Optimization of propagation-based x-ray phase-contrast tomography for breast cancer imaging. Physics in Medicine and Biology 62, 2315–2332. doi:10.1088/1361-6560/aa5d3d.

Boin, M., Haibel, A., 2006. Compensation of ring artefacts in synchrotron tomographic images. Opt. Express, OE 14, 12071–12075. URL: https://www.osapublishing.org/abstract.cfm?uri=oe-14-25-12071, doi:10.1364/OE.14.012071.

Bravin, A., Coan, P., Suortti, P., 2013. X-ray phase-contrast imaging: From pre-clinical applications towards clinics. Physics in Medicine and Biology 58, R1–R35. doi:10.1088/0031-9155/58/1/R1.

Brun, F., Accardo, A., Kourousias, G., Dreossi, D., Pugliese, R., 2013. Effective implementation of ring artifacts removal filters for synchrotron radiation microtomographic images, in: 2013 8th International Symposium on Image and Signal Processing and Analysis (ISPA), pp. 672–676. doi:10.1109/ISPA.2013.6703823.

Brun, F., Pacilè, S., Accardo, A., Kourousias, G., Dreossi, D., Mancini, L., Tromba, G., Pugliese, R., 2015. Enhanced and Flexible Software Tools for X-ray Computed Tomography at the Italian Synchrotron Radiation Facility Elettra. Fundamenta Informaticae 141, 233–243. URL: http://content.iospress.com/articles/fundamenta-informaticae/fi1273, doi:10.3233/FI-2015-1273.

Coan, P., Bravin, A., Tromba, G., 2013. Phase-contrast x-ray imaging of the breast: recent developments towards clinics. J. Phys. D: Appl. Phys. 46, 494007. URL: http://stacks.iop.org/0022-3727/46/i=49/a=494007, doi:10.1088/0022-3727/46/49/494007.

Damera-Venkata, N., Kite, T.D., Geisler, W.S., Evans, B.L., Bovik, A.C., 2000. Image quality assessment based on a degradation model. IEEE Transactions on Image Processing 9, 636–650. doi:10.1109/83.841940.

Dance, D.R., 1990. Monte-Carlo calculation of conversion factors for the estimation of mean glandular breast dose. Phys. Med. Biol. 35, 1211. URL: http://stacks.iop.org/0031-9155/35/i=9/a=002, doi:10.1088/0031-9155/35/9/002.

Geisler, S., Banks, M., 1995. Visual performance, in: Bass, M. (Ed.), Handbook of Optics. McGraw-Hill. Google-Books-ID: _tQZnQEACAAJ.

Gordon, R., Bender, R., Herman, G.T., 1970. Algebraic reconstruction techniques (ART) for three-dimensional electron microscopy and x-ray photography. J. Theor. Biol. 29, 471–481.

Gureyev, T., Mohammadi, S., Nesterets, Y., Dullin, C., Tromba, G., 2013. Accuracy and precision of reconstruction of complex refractive index in near-field single-distance propagation-based phase-contrast tomography. Journal of Applied Physics 114. doi:10.1063/1.4824491.

Gureyev, T.E., Mayo, S.C., Nesterets, Y.I., Mohammadi, S., Lockie, D., Menk, R.H., Arfelli, F., Pavlov, K.M., Kitchen, M.J., F Zanconati, Dullin, C., Tromba, G., 2014a. Investigation of the imaging quality of synchrotron-based phase-contrast mammographic tomography. J. Phys. D: Appl. Phys. 47, 365401. URL: http://stacks.iop.org/0022-3727/47/i=36/a=365401, doi:10.1088/0022-3727/47/36/365401.

Gureyev, T.E., Nesterets, Y., Ternovski, D., Thompson, D., Wilkins, S.W., Stevenson, A.W., Sakellariou, A., Taylor, J.A., 2011. Toolbox for advanced x-ray image processing, p. 81410B. URL: http://adsabs.harvard.edu/abs/2011SPIE.8141E.150G, doi:10.1117/12.893252.

Gureyev, T.E., Nesterets, Y.I., de Hoog, F., Schmalz, G., Mayo, S.C., Mohammadi, S., Tromba, G., 2014b. Duality between noise and spatial resolution in linear systems. Opt Express 22, 9087–9094.

Hammerstein, G.R., Miller, D.W., White, D.R., Masterson, M.E., Woodard, H.Q., Laughlin, J.S., 1979. Absorbed radiation dose in mammography. Radiology 130, 485–491. URL: http://europepmc.org/abstract/med/760167.

Hooley, R.J., Scoutt, L.M., Philpotts, L.E., 2013. Breast Ultrasonography: State of the Art. Radiology 268, 642–659. URL: http://pubs.rsna.org/doi/abs/10.1148/radiol.13121606, doi:10.1148/radiol.13121606.

Johns, P.C., Yaffe, M.J., 1985. Theoretical optimization of dual-energy x-ray imaging with application to mammography. Med. Phys. 12, 289–296. URL: http://onlinelibrary.wiley.com/doi/10.1118/1.595766/abstract, doi:10.1118/1.595766.

Kak, A., Slaney, M., 2001. Principles of Computerized Tomographic Imaging. Classics in Applied Mathematics, Society for Industrial and Applied Mathematics. URL: http://epubs.siam.org/doi/book/10.1137/1.9780898719277. dOI: 10.1137/1.9780898719277.

Keyriläinen, J., Fernández, M., Bravin, A., Karjalainen-Lindsberg, M.L., Leidenius, M., von Smitten, K., Tenhunen, M., Kangasmäki, A., Sipilä, P., Nemoz, C., Virkkunen, P., Suortti, P., 2011. Comparison of in vitro breast cancer visibility in analyser-based computed tomography with histopathology, mammography, computed tomography and magnetic resonance imaging. J Synchrotron Radiat 18, 689–696. doi:10.1107/S090904951102810X.

Longo, R., Arfelli, F., Bellazzini, R., Bottigli, U., Brez, A., Brun, F., Brunetti, A., Delogu, P., Di Lillo, F., Dreossi, D., Fanti, V., Fedon, C., Golosio, B., Lanconelli, N., Mettivier, G., Minuti, M., Oliva, P., Pinchera, M., Rigon, L., Russo, P., Sarno, A., Spandre, G., Tromba, G., Zanconati, F., 2016. Towards breast tomography

with synchrotron radiation at Elettra: first images. Physics in Medicine and Biology 61, 1634–1649. doi:10.1088/0031-9155/61/4/1634.

Miao, J., Förster, F., Levi, O., 2005. Equally sloped tomography with oversampling reconstruction. Phys. Rev. B 72, 052103. URL: https://link.aps.org/doi/10.1103/PhysRevB.72.052103, doi:10.1103/PhysRevB.72.052103.

Mohammadi, S., Larsson, E., Alves, F., Dal Monego, S., Biffi, S., Garrovo, C., Lorenzon, A., Tromba, G., Dullin, C., 2014. Quantitative evaluation of a single-distance phase-retrieval method applied on in-line phase-contrast images of a mouse lung. J Synchrotron Rad, J Synchrotron Radiat 21, 784–789. URL: http://scripts.iucr.org/cgi-bin/paper?mo5080, doi:10.1107/S1600577514009333.

Myers, G.R., Thomas, C.D.L., Paganin, D.M., Gureyev, T.E., Clement, J.G., 2010. A general few-projection method for tomographic reconstruction of samples consisting of several distinct materials. Appl. Phys. Lett. 96, 021105. URL: http://aip.scitation.org/doi/abs/10.1063/1.3279150, doi:10.1063/1.3279150.

Nesterets, Y.I., Gureyev, T.E., 2014. Noise propagation in x-ray phase-contrast imaging and computed tomography. J. Phys. D: Appl. Phys. 47, 105402. URL: http://stacks.iop.org/0022-3727/47/i=10/a=105402, doi:10.1088/0022-3727/47/10/105402.

Nesterets, Y.I., Gureyev, T.E., Mayo, S.C., Stevenson, A.W., Thompson, D., Brown, J.M.C., Kitchen, M.J., Pavlov, K.M., Lockie, D., Brun, F., Tromba, G., 2015. A feasibility study of X-ray phase-contrast mammographic tomography at the Imaging and Medical beamline of the Australian Synchrotron. J Synchrotron Radiat 22, 1509–1523. doi:10.1107/S160057751501766X.

Paganin, D., Mayo, S.C., Gureyev, T.E., Miller, P.R., Wilkins, S.W., 2002. Simultaneous phase and amplitude extraction from a single defocused image of a homogeneous object. J Microsc 206, 33–40.

Pelt, D.M., Batenburg, K.J., 2014. Improving Filtered Backprojection Reconstruction by Data-Dependent Filtering. IEEE Transactions on Image Processing 23, 4750–4762. doi:10.1109/TIP.2014.2341971.

Protection, Measurements, 2004. National Council on Radiation Protection and Measurements - an overview | ScienceDirect Topics. URL: http://www.sciencedirect.com/topics/medicine-and-dentistry/national-council-on-radiation-protection-and-measurements.

Sickles, E.A., D'Orsi, C.J., 2014. How Should Screening Breast US Be Audited? The BI-RADS Perspective. Radiology 272, 316–320. URL: http://pubs.rsna.org/doi/full/10.1148/radiol.14140634, doi:10.1148/radiol.14140634.

van der Sluis, A., van der Vorst, H.A., 1990. SIRT- and CG-type methods for the iterative solution of sparse linear least-squares problems. Linear Algebra and its Applications 130, 257–303. URL: http://www.sciencedirect.com/science/article/pii/002437959090215X, doi:10.1016/0024-3795(90)90215-X.

Smith, S.M., Brady, J.M., 1997. SUSAN—A New Approach to Low Level Image Processing. International Journal of Computer Vision 23, 45–78. URL: https://link.springer.com/article/10.1023/A:1007963824710, doi:10.1023/A:1007963824710.

Tang, J., Nett, B.E., Chen, G.H., 2009. Performance comparison between total variation (TV)-based compressed sensing and statistical iterative reconstruction algorithms. Phys. Med. Biol. 54, 5781. URL: http://stacks.iop.org/0031-9155/54/i=19/a=008, doi:10.1088/0031-9155/54/19/008.

Verdun, F.R., Racine, D., Ott, J.G., Tapiovaara, M.J., Toroi, P., Bochud, F.O., Veldkamp, W.J.H., Schegerer, A., Bouwman, R.W., Giron, I.H., Marshall, N.W., Edyvean, S., 2015. Image quality in CT: From physical measurements to model observers. Physica Medica: European Journal of Medical Physics 31, 823–843. URL: http://www.physicamedica.com/article/S1120-1797(15)00329-4/abstract, doi:10.1016/j.ejmp.2015.08.007.

Wang, Z., Bovik, A.C., 2002. A universal image quality index. IEEE Signal Processing Letters 9, 81–84. URL: http://adsabs.harvard.edu/abs/2002ISPL...9...81W, doi:10.1109/97.995823.

Wang, Z., Bovik, A.C., Sheikh, H.R., Simoncelli, E.P., 2004. Image quality assessment: from error visibility to structural similarity. IEEE Transactions on Image Processing 13, 600–612. doi:10.1109/TIP.2003.819861.

# 6

# Application on Breast cancer diagnosis: importance of 3D visualisation and comparison with absorption-based CT

## Contents

## 6.1 *Introduction*

Early detection, which is associated with an increased survival rate, is the primary method of containing deaths of breast cancer. Although the reference standard for early detection of breast cancer is mammography, the limits of this test are well documented. As underlined in Chapter 1, despite the advantage of its excellent spatial resolution, in conventional mammography the 2D projection images can overlap normal tissue, soft tissue masses, and calcifications affecting the detection and visualisation of cancer. The poor contrast between healthy and cancerous tissue, and the need to discriminate minute and subtle details require an imaging platform that has adequate spatial and contrast resolution for visualisation and differentiation of abnormalities. Furthermore, breast density and tissue distribution vary among women, adding complexity to the interpretation, particularly for women with dense breasts. A tomographic approach can provide a three-dimensional visualisation of the breast, helping the depiction of the 3D morphology and distribution of the lesions. This could lead to an improvement in screening sensitivity, as it would allow the detection of both smaller lesions and cancers not apparent by conventional mammography, and in screening specificity as well, as it would allow a better visualisation of the margin of a mass or its asymmetry leading to a more specific characterisation of the lesions and reduction in false-positive recalls. In this chapter an example of improvements in lesion detection accuracy of phase-contrast breast-CT with respect to digital mammography and a comparison between clinical breast-CT system and phase-contrast synchrotron based breast-CT, will be given.

## 6.2 Benefits of CT modality on breast cancer diagnosis

X-ray computed tomography has been proposed and evaluated multiple times as a potentially alternative method for breast imaging. The scope of this section is to analyse the information content of phase-contrast breast CT images in comparison to digital mammography, in order to highlight the benefits that this technique could bring in the diagnostic process.

### 6.2.1 Samples description and acquisition parameters

An entire fresh sample coming from a full mastectomy of a 60 years old woman, directly delivered from a local operating centre, has been used for this study. The excised specimen contained an invasive papillary carcinoma with focal skin invasion, composed of multiple nodules through the scar tissue (hereafter referred to as *Right Breast*). The experiment was conducted at the Imaging and Medical beamline (IMBL) of the Australian Synchrotron (Melbourne), which characteristics have been detailed in Chapter 3. CT scans were collected, in propagation-based imaging mode (PB-CT), at three different sample-to-detector distances; 0.3, 2 and 5.71 $m$ using two monochromatic x-ray energies: 32 and 38 $keV$. These conditions were selected purposefully to allow examination of interaction effects of different phase contrast imaging parameters. For each scan in this study, the number of CT projections was 1800, the angular range was 180 degrees and the exposure time was 0.05 seconds per projection. The dose delivered to the samples was about 4 $mGy$. The detector was a Hamamatsu CMOS flat panel sensor C9252DK-14, which contains a $CsI$ scintillator deposited directly on two-dimensional photodiode array. The detector was used in the partial scan mode with a pixel size of 100 $\mu m \times 100$ $\mu m$. For CT data processing and analysis X-TRACT (Gureyev et al. (2011)) software was used, which included data pre-processing, phase retrieval and CT reconstruction. The pre-processing of projection images contains dark-current and flat-field correction and ring removal filter. The phase retrieval was based on the TIE-Hom algorithm (Paganin et al. (2002)), which was applied to the projections, to exploit the phase

information, with a value of $\delta/\beta$ ratio close to the theoretical value of the relative $\delta/\beta$ value for glandular tissue in adipose tissue ( TS-imaging website). The used CT reconstruction algorithm, was the iterative filtered back- projection (iFBP). This choice was based on the results of our previous publication (Baran et al. (2017)). The diagnosis accuracy based on the obtained CT reconstructed images and 3D rendering was then compared with three major conventional imaging methods performed before the surgical mastectomy.

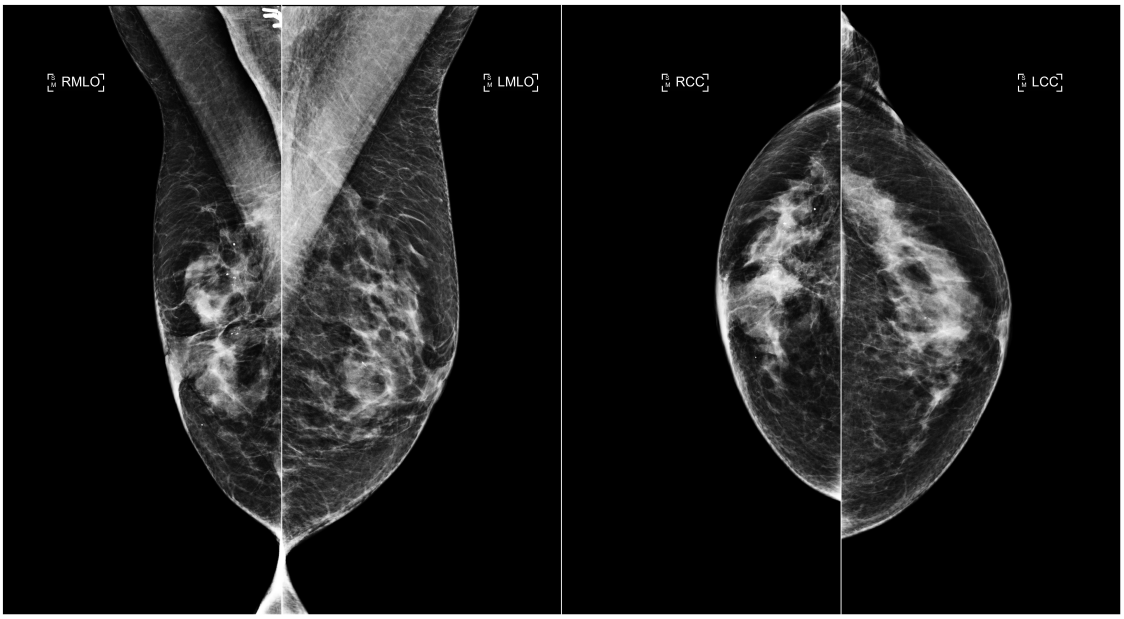


**Figure 6.1:** Digital mammography images acquired before the surgical mastectomy. On the left the medio-lateral oblique view, on the right the cranio-caudal view.

### 6.2.2 Results and discussion

It is worth mentioning that phase-contrast PB-CT imaging of fresh full mastectomy samples was a world-first result. To point out the advantages that the phase-contrast breast CT could bring to the diagnostic process it is necessary to start from the diagnosis made on the mammography, tomosynthesis and ultrasound examination and then, highlight the differences. The mammography examination (Fig. 6.1) of the patient shows an asymmetry of the glandular tissue between the two breasts, a condition that is often caused by the lobular carcinoma. The glandular tissue of the *Right Breast* has an architectural distortion and involves

micro-calcifications, moreover, the images are compatible with a skin invasion, as the portion of the skin near the nipple is thicker and denser than the rest. However, it is not possible to characterise the margins of an eventual mass. On the contrary, on the tomosynthesis image (Fig. 6.2), opacities are clearly spiculated allowing to identify the malignant nature of the lesion. From the ultrasound examination,

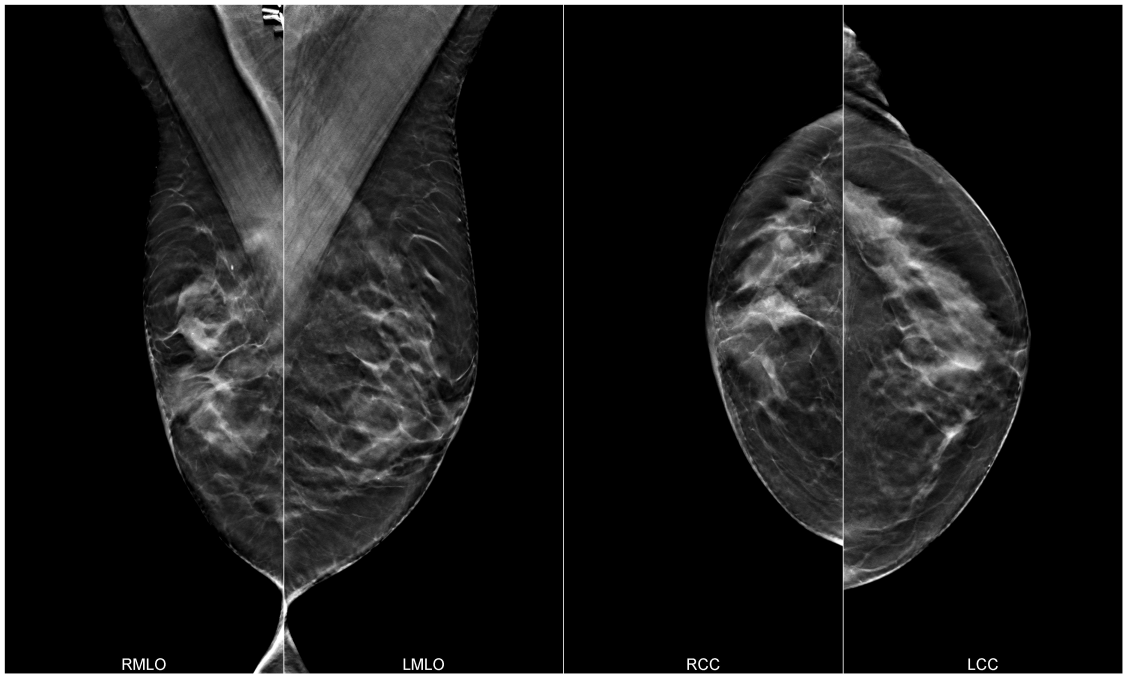


**Figure 6.2:** Tomosynthesis images. On the left side, the medio-lateral view of both breasts, on the left the cranio-caudal one.

multiple lesions are visible: a suspicious solid lesion 6 *cm* far from the nipple, a hypoechoic lesion in the upper quadrants with a diameter of 1.82 *cm* containing calcifications at 3 *cm* far from the nipple (Fig. 6.3), and neoplastic tissue with calcifications inside the ducts in the retroareolar region. This clinical picture is compatible with a multicentric tumour with in situ component and lymph nodes. The reconstructed 3D images obtained from the SR CT scans can be visualised in three orthogonal planes: transverse, sagittal, and coronal (Fig. 6.4) and in 3D rendering (Fig. 6.5). The transverse and sagittal breast-CT views correspond to the mammographic cranio-caudal and mediolateral views. On the CT images a lesion causing a retraction of the tissue is visible. Its dimensions are measurable and its malignant character is clearly assessable. In contrast with the mammography,


**Figure 6.3:** Ultrasound examination of Right Breast. The oval delimited by white markers is the hypoechoic lesion including microcalcification (brighter spots).

where it is not easy to understand which part is malignant or healthy, here the parenchymal distortion and the spiculations are clear. In addition, the skin invasion, that on the mammography and tomosynthesis is just suspected, here is clearly noticeable from the solid tissue expanding toward the areola (sagittal view of the sample on fig. 6.4). This study demonstrates that 3D diagnostic imaging, in particular, phase-contrast breast-CT, can be performed at clinical- compatible doses producing imaging with a significantly higher diagnostic value than the conventional methods. Furthermore, this case study is useful to conclude that, when dealing with a spiculated lesion, 2D mammography is sufficient to detect the suspicious anomalous condition, on tomosynthesis one is able to see all the spiculation in the different plans and CT offers an advantage in the lesion morphology characterisation (dimensions, borders, distribution ...). Another major advantage of the tomographic modality is the possibility to obtain a 3D rendering of the entire examined volume.

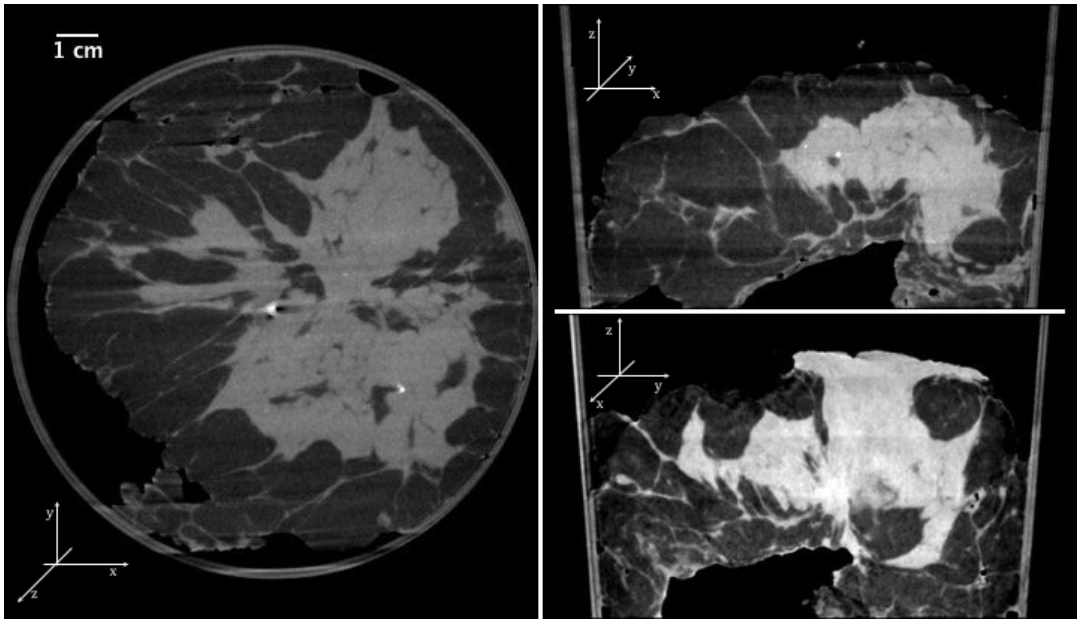


**Figure 6.4:** Tomographic reconstruction of Right Breast. On the left the conventional view (plane parallel to the x-ray beam). On the right the two related orthogonal views, above the transverse plane and below the sagittal one. The dataset is the one acquired at 5.71 $m$ and 38 $keV$, using the classical FBP reconstruction method and pre-processing data with the TIE-Hom phase retrieval algorithm.

The presented renderings were obtained using Avizo software, a proprietary software package for 3D data analysis produced by Thermo Scientific$^{TM}$. Figure 6.5 shows a depiction of the *Right Breast* based on the different density values: the green part is the less dense part and it is associated with the adipose tissue; yellow and red parts are the densest ones and are associated with skin (on the top of the sample), fibrous tissue and cancerous tissue. In addition to CT visualisation, the 3D rendering, thanks to its depth perception, allows a global analysis of the mass with a better characterisation of shape, margins, extent of the spiculations, etc. This could provide a strong rationale for assessing tumour features, for example, throughout the course of chemotherapy, or, give a precise position map in case of a multifocal lesion in pre-surgical planning.

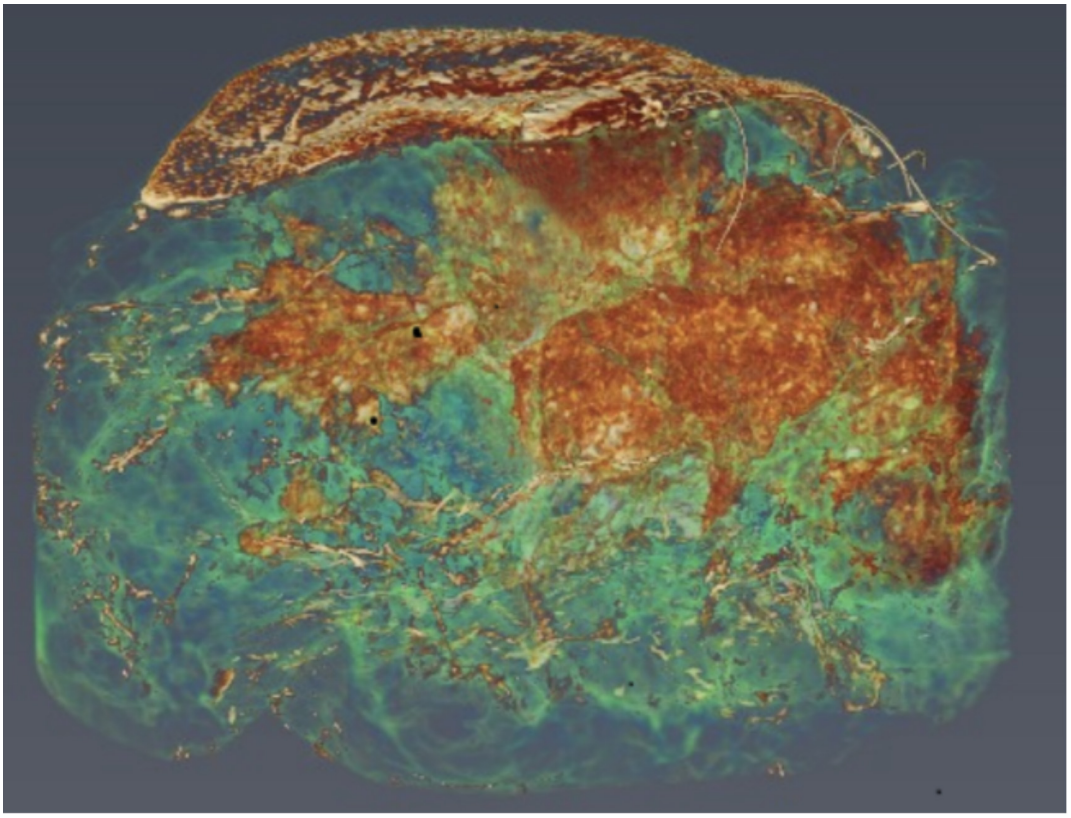

**Figure 6.5:** 3D rendering of the Right Breast obtained with Avizo software (false colours).

## 6.3 Radiological comparison between phase-contrast CT and absorption based CT for breast imaging

The previous paragraph was meant to underline the benefits that a tomographic technique and, consequently, a 3D visualisation could bring to the diagnostic process of breast cancer. All shown images, as described, have been obtained with synchrotron radiation phase-contrast breast CT technique, which optimisation is the main goal of this thesis. However, it has to be remarked that, in recent years, the cone-beam breast-CT (CBBCT) dedicated system, has undergone a great development in the acquisition of true breast 3D images (O'Connell et al. (2010); Han et al. (2016); Wienbeck et al. (2017); Uhlig et al. (2017)). To investigate ability to detect and characterise breast lesions of both techniques (clinical breast-CT system and phase-contrast synchrotron-based breast-CT), and to evaluate their

diagnostic performances, a radiological comparison on images of same samples has been carried out.

### 6.3.1 Materials and methods

12 breast tissue specimens including different types of breast cancer ranking from invasive ductal carcinoma, intraductal papillary carcinoma, ductal carcinoma in situ, as well as such benign abnormalities as phyllodes tumour and fibrosis, have been imaged with both a Koning Breast-CT scanner at Göttingen University (Germany) and with synchrotron propagation based CT (PB-CT) at the SYRMEP beamline of Elettra Synchrotron source (Italy) (see Table 6.1 for samples details).

**Table 6.1:** Mastectomy samples description.

| *Sample* | *Location* | *Description* |
|---|---|---|
| P14852 | right | invasive ductal carcinoma (IDC) |
| P19085 | left | intraductal papillary *in situ* (Tis) |
| P14416 | left | invasive ductal carcinoma (IDC) |
| P26447 | right | invasive ductal carcinoma (IDC) |
| P24178 | right | fibrous |
| P23813 | left | invasive ductal carcinoma (IDC) with external papillary carcinoma |
| P23540 | left | not malignant |
| P19009 | left | invasive ductal carcinoma with DCIS |
| P13970 | left | invasive ductal carcinoma (IDC) |
| P18197 | right | DCIS |
| P19430 | left | DCIS |
| P19489 | right | benign Phyllodes tumour |

All samples were formalin fixed and stored under-vacuum in plastic bags. For the absorption based images a Koning Breast CT (KBCT) System (model CBCT 1000) was used (Koning website). The system includes a horizontal CT scanner, a patient table assembly, x-ray/data acquisition components mounted on a rotating assembly, a reconstruction engine and 3D visualization/temporary DICOM storage package. The data acquisition is achieved by use of a flat panel detector, an x-ray tube, a 480 VAC high frequency generator, a frame grabber card and a PC workstation. The acquisition parameters are shown in table 6.2, for the purposes of this work

only images acquired with the lowest value of radiation dose have been considered. The system and its working principle are shown in Fig. 6.6a and 6.6b.

**Table 6.2:** Acquisition parameters for Köning breast CT images.

| $kV$p | $mA$ | $mAs$ | $mGy$ | Pixel size ($mm$) |
|---|---|---|---|---|
| 49 | 50 | 120 | 5.85 | 0.273 |
| 49 | 100 | 240 | 11.7 | 0.273 |
| 49 | 200 | 480 | 23.41 | 0.273 |

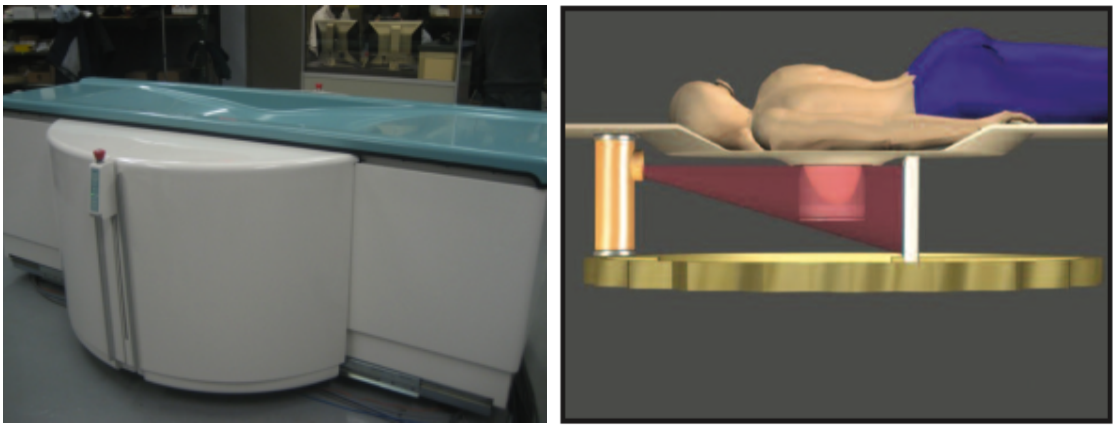

**Figure 6.6:** Koning breast CT system (model CBCT 1000) (on the left), principle of the system (on the right).

For the acquisitions performed at SYRMEP, based on previous optimisations works, a sample-to-detector distance of 9 $m$ was chosen. The energy has been selected between 32, 35 and 38 $keV$ depending on the dimension of the samples. For all scans, the number of CT projections was 1800, over an angular range of 180°and the total exposure time was 40 seconds. In order to test the feasibility of using the PB-CT as screening examination, different levels of radiation dose have been used. The highest one was the one delivered by the Koning system (allowing a comparison between the two techniques at a fixed level of dose), the second and the third one were one half and one quarter of the first one, respectively (allowing the diagnostic performance test of PB-CT). The detector used was a XCounter photon counting with $CdTe$-CMOS technology and a pixel size of 100 $\mu m$. The

diagnostic content of the obtained images was evaluated and analysed by a group of expert radiologists. For each sample the radiologists were asked to comment about features and details important for the diagnosis of the images obtained with both technique, and underline pros and cons of them. In a second phase, they were asked to look at the PB-CT images obtained with lower level of dose, and assess if it is still possible to do an accurate diagnosis on them.

### 6.3.2 Results and discussion

For the sake of brevity, the discussion of two of the analysed sample is reported in the following. The first case is sample P19085, it includes an intraductal papillary tumour *in situ* . Figures 6.7a and 6.7b show the Koning and the SR image respectively. One of the most important noticeable aspects that differentiate the two images is the character of the margins. On the Koning image, they are quite blurry and it is not understandable if the lesion is infiltrating or not. On the SR image, since the borders of the lesion are sharper, it is possible to say that on the right part they are regular and there is no signs of infiltration, on the left part there is some poly-lobed area that could be compatible with an expansive growth.

Moreover, inside the lesion there is a fatty component that is clearly distinguishable on the SR image and completely flat (not detected) in the Koning one (yellow circle on Fig. 6.7). As a general comment, since the diagnostic process is most of all based on the morphologic assessment of the structures, the SR phase-contrast image, allowing the visibility of margins, lobes and spiculations, is, for sure, more reliable. The second case is P19009 including an invasive ductal carcinoma with *in situ* component. Figures 6.8a and 6.8b display the absorption based and the phase-contrast based CT, respectively. Again, the overall morphology of the lesion is better visualised on the SR image. Margins are better defined, the shape of the micro-calcifications is clearly detectable (brighter spots inside the tissue), and the higher contrast resolution allows a density differentiation. Due to the nature of this particular cancer type, on the Koning image it is still possible to assess the

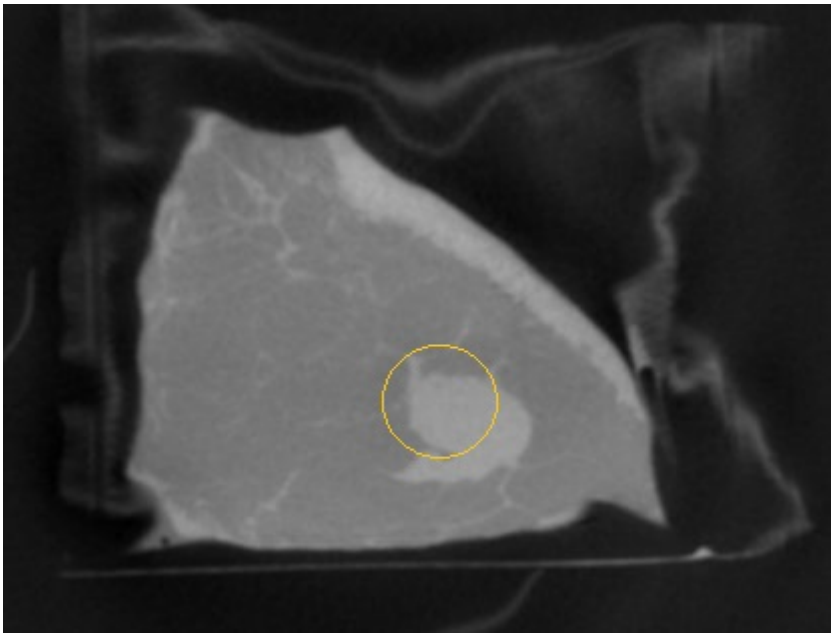

(a)

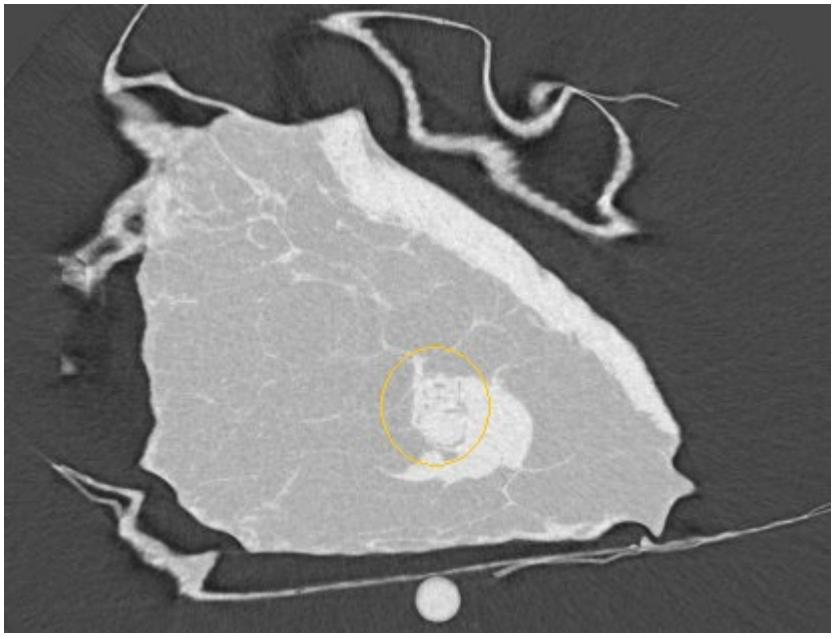

(b)

**Figure 6.7:** Sample P19085. Excised breast sample from an 80 years old woman, including an *in situ* intraductal papillary carcinoma. a) image obtained with the Koning dedicated breast-CT system. b) image obtained with PB-CT technique

malignant character of the lesion (as the edges are very jugged), however, due to the higher general sharpness, the diagnosis is more accurate on the SR image.

After this step, where images obtained at the same delivered radiation dose

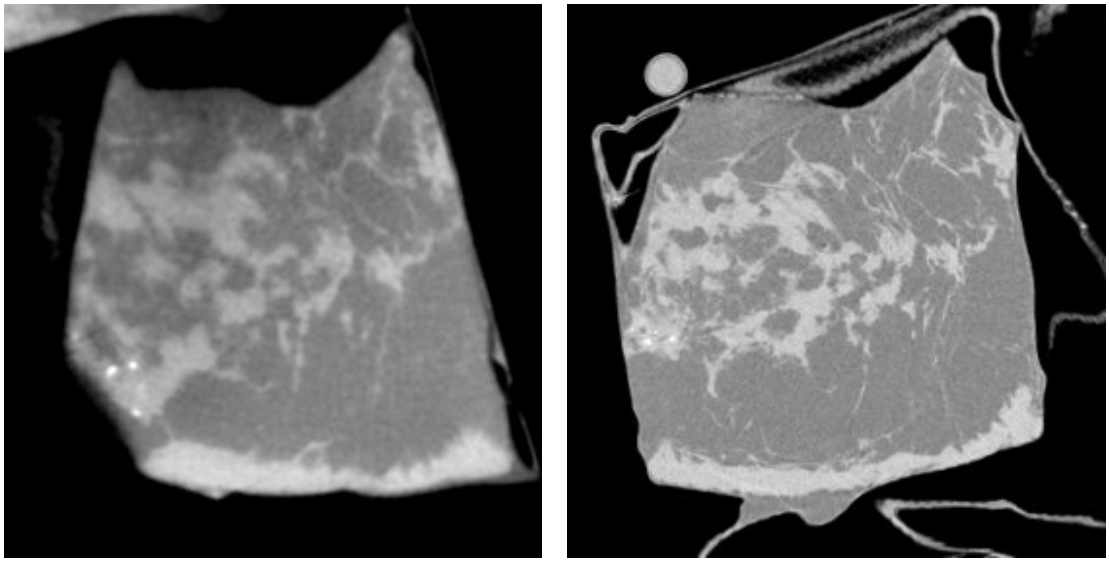

(a) (b)

**Figure 6.8:** Sample P19009. Excised breast sample from a 62 years old woman, including an invasive ductal carcinoma with DCIS. a) image obtained with the Köning dedicated breast-CT system. b) image obtained with PB-CT technique

were compared, a second comparison was carried out. Focusing just on the SR images, radiologists were asked if, delivering the half of the previous dose, it is possible to appreciate the same peculiarities of the images and make the same diagnostic conclusions. In most of the cases, and in particular in both cases reported above, results indicate that PB-CT can achieve a better image quality of the Koning breast-CT system whereby delivering a considerably lower level of mean glandular dose. Figure 6.9 shows a close-up of the first sample (P19085) including the area of the tumour. The low dose image is more noisy and loses the details definition inside the lesion, despite that, it is still possible to do the diagnosis with the same accuracy of the previous image.

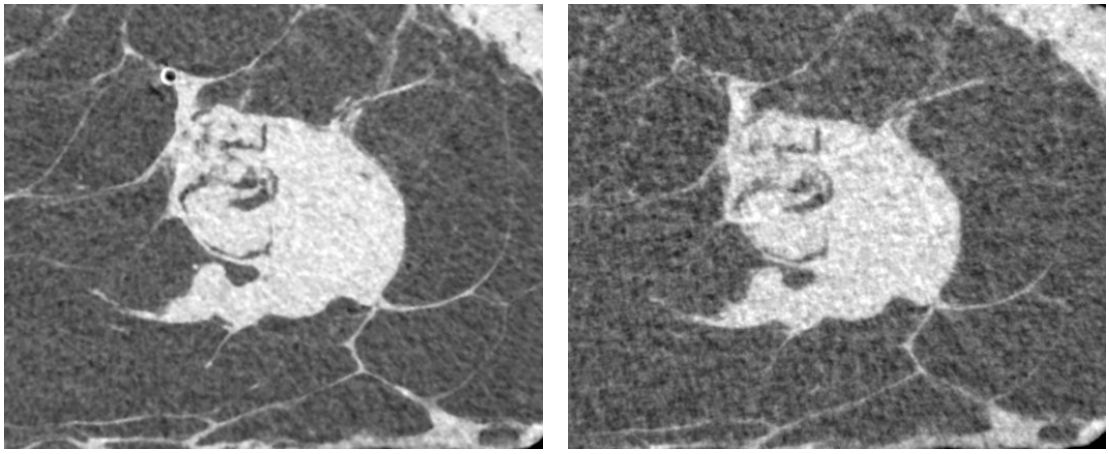

(a) (b)

**Figure 6.9:** Close-up of sample P19085. a) image obtained delivering a dose of 5 $mGy$, b) image obtained with a dose of 2.5 $mGy$.

# References

Baran, P., Pacile, S., Nesterets, Y., Mayo, S., Dullin, C., Dreossi, D., Arfelli, F., Thompson, D., Lockie, D., McCormack, M., Taba, S., Brun, F., Pinamonti, M., Nickson, C., Hall, C., Dimmock, M., Zanconati, F., Cholewa, M., Quiney, H., Brennan, P., Tromba, G., Gureyev, T., 2017. Optimization of propagation-based x-ray phase-contrast tomography for breast cancer imaging. Physics in Medicine and Biology 62, 2315–2332. doi:10.1088/1361-6560/aa5d3d.

Gureyev, T.E., Nesterets, Y., Ternovski, D., Thompson, D., Wilkins, S.W., Stevenson, A.W., Sakellariou, A., Taylor, J.A., 2011. Toolbox for advanced x-ray image processing, p. 81410B. URL: http://adsabs.harvard.edu/abs/2011SPIE.8141E.150G, doi:10.1117/12.893252.

Han, M., Park, S., Baek, J., 2016. Effect of anatomical noise on the detectability of cone beam CT images with different slice direction, slice thickness, and volume glandular fraction. Opt Express 24, 18843–18859.

O'Connell, A., Conover, D.L., Zhang, Y., Seifert, P., Logan-Young, W., Lin, C.F.L., Sahler, L., Ning, R., 2010. Cone-Beam CT for Breast Imaging: Radiation Dose, Breast Coverage, and Image Quality. American Journal of Roentgenology 195, 496–509. URL: http://www.ajronline.org/doi/full/10.2214/AJR.08.1017, doi:10.2214/AJR.08.1017.

Paganin, D., Mayo, S.C., Gureyev, T.E., Miller, P.R., Wilkins, S.W., 2002. Simultaneous phase and amplitude extraction from a single defocused image of a homogeneous object. J Microsc 206, 33–40.

Uhlig, J., Fischer, U., von Fintel, E., Stahnke, V., Perske, C., Lotz, J., Wienbeck, S., 2017. Contrast Enhancement on Cone-Beam Breast-CT for Discrimination of Breast Cancer Immunohistochemical Subtypes. Transl Oncol 10, 904–910. URL: https://www.ncbi.nlm.nih.gov/pmc/articles/PMC5614638/, doi:10.1016/j.tranon.2017.08.010.

Wienbeck, S., Lotz, J., Fischer, U., 2017. Review of clinical studies and first clinical experiences with a commercially available cone-beam breast CT in Europe. Clin Imaging 42, 50–59. doi:10.1016/j.clinimag.2016.11.011.

# 7

# Application on Breast cancer diagnosis: three-dimensional virtual histology

## Contents

## 7.1 *Introduction*

A new, interesting challenge for phase-contrast x-ray micro-CT is represented by the possibility to exploit it as an alternative method for intraoperative histological examination for breast specimens to confirm excision of image-detected breast lesions and provide information regarding diagnosis and classification, prognostication (e.g. tumour grade, lymphovascular invasion) and subsequent treatment pathways (e.g. margin assessment and hormone receptor status). The basic advantage of using micro-CT relies on the ability to produce, in a non-destructive way, a 3D visualisation of the specimen that can be virtually sectioned in any angle or plane. Data can be also segmented to isolate individual structures, allowing them to be analysed separately from the surrounding tissue but still maintaining their *in situ* configuration. To date, there has been limited use of micro-CT for imaging tumour specimens, and only a few small studies have used micro-CT to evaluate the structure of excised breast tissue (Tang et al. (2013); Gufler et al. (2011b,a); Gromoll and Salmon (2008); Nishide et al. (2004); Keyriläinen et al. (2008); Willekens et al. (2014)), some of them are strictly related to micro-calcification imaging, due to the significant impact on the assessment of the malignancy risk. The study described in this chapter was meant to evaluate the potential usefulness of this method as a supporting tool for histological examination in breast cancer diagnosis, by comparing images obtained with PB-CT and classical histological images. All the images were analysed in detail by specialist histologist, in terms of the visibility of the important features for breast cancer diagnosis.

## 7.2 Phase-contrast 3D imaging as possible method to improve histological examination

The aim of this study was to evaluate the potential usefulness of 3D phase-contrast micro-computed-tomography (micro-CT) imaging at high spatial resolutions as an adjunct to conventional histological microscopy. Results of a recent experiment at the SYRMEP beamline of Elettra Synchrotron using propagation-based phase-contrast micro-tomography method are presented. In this study, x-ray images of multiple breast tissue specimens, 2 to 3 $mm$ in diameter, obtained with 1.2 $\mu m$ pixel size, were analysed and compared with corresponding histological images. Together with the results, the prospects for practical use of this method are discussed in the following paragraphs.

### 7.2.1 Materials and methods

*Samples description*

32 breast tissue specimens, prepared by the pathology department of the Cattinara academic hospital of Trieste, have been considered for x-ray phase-contrast CT scans and histopathological examination. All samples were taken from macroscopic regions of interest within the specimen and prepared for standard histology process. After scanning the samples using PB-CT, routine haematoxylin and eosin stained (H&E) sections were made from these specimens, and microscopic areas of interest identified. Two-millimetre core biopsies were then taken of the paraffin embedded tissue blocks in these areas of interest. Cores were cut using a standard microtome into serial 3-5 $\mu m$ thickness sections, taken at 40-50 $\mu m$ stepwise levels, until tissue was exhausted. Sections were mounted on glass slides and underwent routine staining with haematoxylin and eosin. At the end, the sections were digitalised at 20x optical zoom. Detailed diagnostic information about each core biopsy sample prepared for the experiment are presented in Table 7.1.

*Experimental setup*

The x-ray phase-contrast CT scans were performed at the SYRMEP beamline at

**Table 7.1:** Histological findings on breast tissue specimens

| *Sample* | *Description* |
|---|---|
| 10753 D | Medullary |
| 1075 B | Ductal G2 |
| 10754 G | *in situ* lobular carcinoma |
| 10778 A | Ductal G1 |
| 10805 C | Apocrine G2 |
| 10834 E | Ductal G3 (solid) |
| 10945 G | Lobular G2 |
| 10971 C | Micro papillary |
| 11047 F | Ductal G3 |
| 11069 B | *in situ* carcinoma |
| 11069 F | Invasive carcinoma |
| 11094 E | Ductal G2 with skin |
| 11110 M | Triple negative ductal G3 |
| 11131 | Fat necrosis |
| 11261 E | Lobular G2 |
| 11487 D | Mucinous |
| 11607 C | Sclerosing adenosis |
| 11624 D | *in situ* carcinoma |
| 11624 E | Healthy tissue |
| 11624 H | Healthy tissue |
| 11735 D | Lobular G2 |
| 11735 F | Lobular G2 |
| 11752 F | Lobular G2 |
| 11776 E | Ductal G2 |
| 11884 A | Papilloma |
| 11895 G | Papillary |
| 11935 B | Lobular + benign |
| 11935 C | Papilloma |
| 12101 M | Squamous cell carcinoma |
| 12159 A | *in situ* cribriform carcinoma |
| 12321 B | Phylloid tumour |
| 12322 G | *in situ* carcinoma |

the Elettra synchrotron, Trieste, Italy. All samples were scanned using the 2 GeV storage ring mode and a white (polychromatic, filtered with 1 $mm$ of $Si$ and 0.4 $mm$ of $Al$) x-ray beam. The detector used, was an air-cooled, 16 $bit$, SCMOS camera (Hamamatsu C11440-22C) with a $2048 \times 2048$ pixel chip coupled with a high numerical aperture optic that allows a variable pixel size, nominally between 0.9 - 5.2 $\mu m$. Samples were imaged at a sample-to-detector distance of 10 $cm$ using polychromatic x-ray with the mean energy of 17 $keV$ in the propagation-based mode. For each sample, the scan with 1.2 $\mu m$ pixel size, containing 1800 projections was collected with 0.1° angular step over 180°.

*CT reconstruction procedure*

CT data pre-processing and reconstruction were performed using STP software (Brun et al. (2015)). Firstly, the projections collected during the experiment were pre-processed using dark current and flat-field corrections and a ring removal filter. In order to exploit the phase shift information, the algorithm based on the Homogeneous Transport of Intensity equation (TIE-Hom) (Paganin et al. (2002)) was applied to the projections prior to tomographic reconstruction using filtered back projection.

*Images alignement*

In order to obtain CT slices corresponding to the histological slices the volumetric CT data were imported into Drishti, an open-source scientific visualisation software designed by Ajay Limaye at the National Computational Infrastructure's VizLab of Canberra, Australia. (Limaye (2012)). This enabled oblique angled CT slices that most closely matched the histological slices. The match was made by adjusting the oblique slice in Drishti until features across the whole CT slice matched corresponding features in the histological slice as closely as possible. Because the histological slices typically experience distortion on mounting to a slide, an affine registration step was required to fully match the distorted histological data and the

corresponding oblique slice extracted from the volume CT data. This step was done using affine registration tool TrackEM2 in Fiji (ImageJ) (Schindelin et al. (2012)).

### 7.2.2 Results and discussion

Histology slides stained with haematoxylin and eosin were used as a reference for a comparative assessment with phase-contrast micro-CT slices. The use of histology images was important for identification of anatomical landmarks and structures, architectural patterns and tissue types in corresponding micro-CT images. For all scanned samples, a good match between micro-CT and histology slices was found. However, in this thesis, the results for two most representative samples are shown. Figures 7.1 and 7.5 show the comparison between the histological and phase-contrast x-ray CT images for an *in situ* carcinoma cribriform type and a mucinous one, respectively.

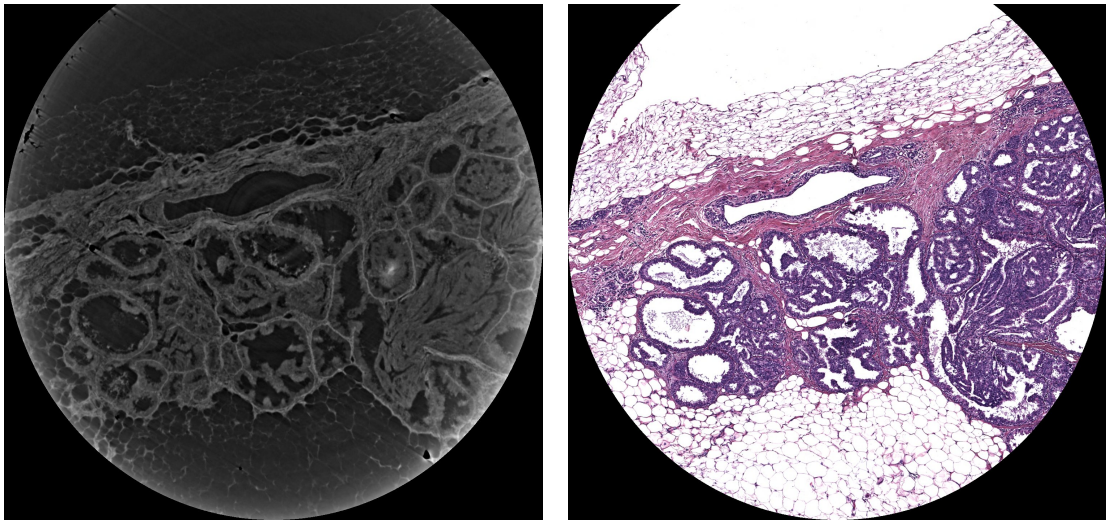

(a) (b)

**Figure 7.1:** Sample 12159 A containing an *in situ* cribriform carcinoma. a) micro-CT slice b) classical histological slice stained with haematoxylin and eosin.

A first, clearly noticeable aspect of the phase-contrast image is the differential density information between the internal epithelial and myoepithelial cells, given by the different grey levels. Additionally, the basement membrane, that immediately surrounds ducts, and the overlying stromal tissue appear well defined (brighter lines

in Fig. 7.1a) and allows a precise characterisation of the architectural structure (an image swipe tool to roll back and forth between the aligned images is available at Sample-12159).

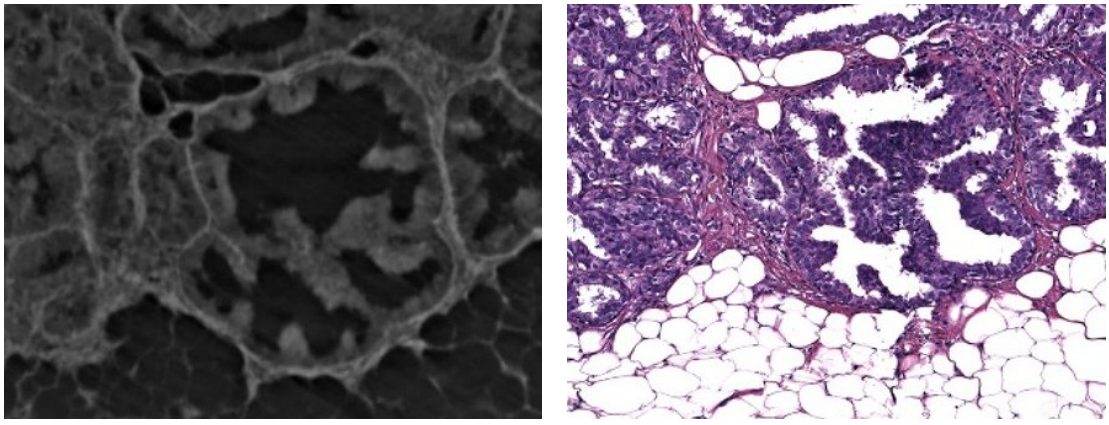

(a) (b)

**Figure 7.2:** Close-up of a duct. On the micro-CT image (a) the basement membrane appears as a defined white line, on the histological image (b) the membrane is still visible but its integrity is not assessable.

The analysis of the basement membrane is important to distinguish between the irregular and infiltrative character of the cancer and the *in situ* one: if the membrane is intact, the neoplastic growth stays within ducts, meaning that the carcinoma is *in situ*, otherwise, the discontinuity of the membrane determines an infiltration outside ducts. In the case reported in Fig. 7.2, from classical histological image (Fig. 7.2b), it is not easy to evaluate this feature, implying the need for a more specific examination to assess the membrane preservation (i.e. P63), in the micro-CT image (Fig. 7.2a), as expected, the connective tissue is clearly lying under the epithelium and it is possible to say that the carcinoma is *in situ*. Adipocytes layers are quite similar in both images, but some of them in the histology image appear as damaged by the cutting process (circular structures in the upper part of Fig. 7.1a and 7.1b). Likewise, the hyperplastic glandular epithelium protruding into the lumen is distinguishable with both methods (Fig. 7.3), but the presence of micro-calcification inside the duct (brighter spots visible in Fig. 7.3a) caused

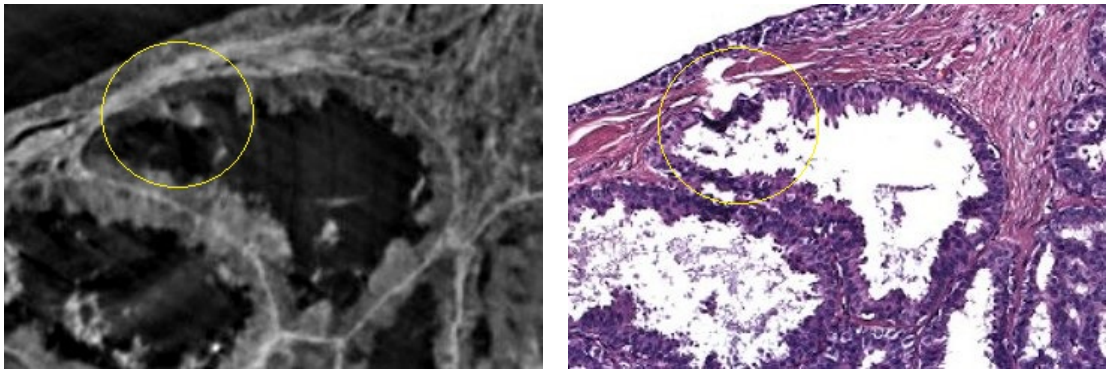

(a) (b)

**Figure 7.3:** Close-up of a duct including micro-calcifications (marked with a yellow circle). On micro-CT image (a) calcifications are well visible e characterised by a brighter grey level, on the histology image (b) they are completely lost due to the cutting process causing an hyperchromasia (dark purple zone inside the circle).

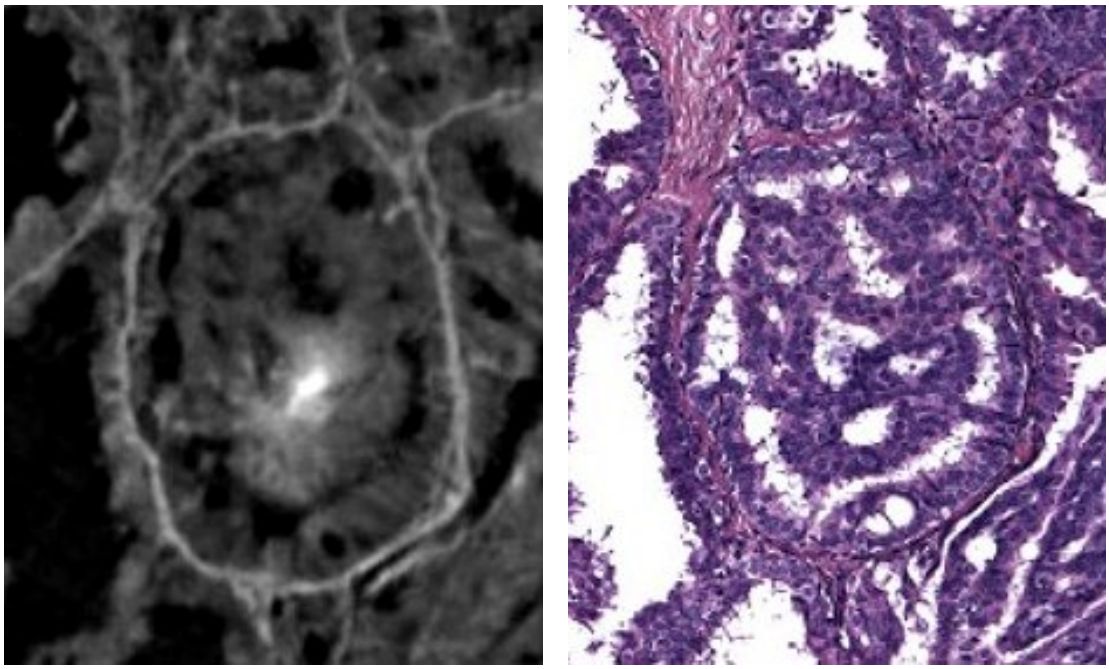

(a) (b)

**Figure 7.4:** Close-up of a duct with the typical cribriform features. Elements with fenestrated aspect appear as dark in micro-CT image (a) and as white in histological one (b).

a tissue deterioration (visible as a hyperchromasia in Fig. 7.3b) during the cut making impossible the evaluation of the micro-calcifications themselves.

Finally, in both images peculiarities of cribriform type are clearly appreciable,

i.e. ducts containing proliferating elements with fenestrated appearance (dark parts in Fig. 7.4a corresponding to white parts in Fig. 7.4b). The second reported sample contains a mucinous carcinoma (Fig. 7.5), as in the previous case a good correspondence of the principal features is clearly noticeable. In particular, there is a small duct including an erythrocyte clot visible as light grey in the micro-CT image (yellow circle in Fig. 7.5a) and red in the classical histology image (yellow circle in Fig. 7.5b). Mucinous carcinoma of the breast is a rare form of invasive ductal carcinoma.

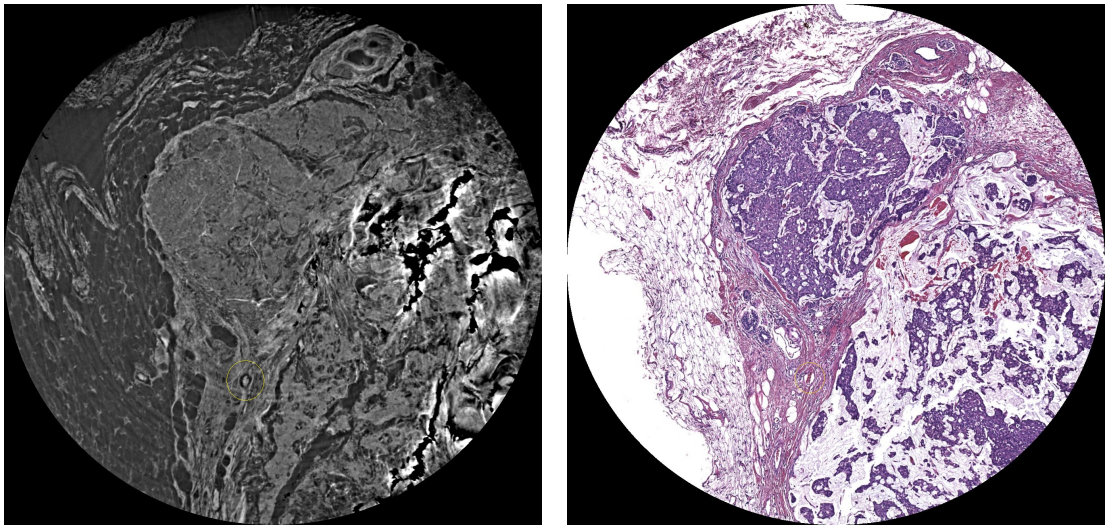

(a) (b)

**Figure 7.5:** Sample 11487 D including a mucinous breast carcinoma. a) micro-CT slice, b) classical histological slice stained with haematoxylin and eosin

In this type of cancer, the tumour is made up of abnormal cells that "float" in pools of mucin, a key ingredient in the slimy, slippery substance known as mucus. In micro-CT (Fig. 7.6a) the mucus is represented by a very light grey pattern, whit small darker island floating on it, on the histological image the mucus appears as a light pink web with dark purple island (Fig. 7.6b).

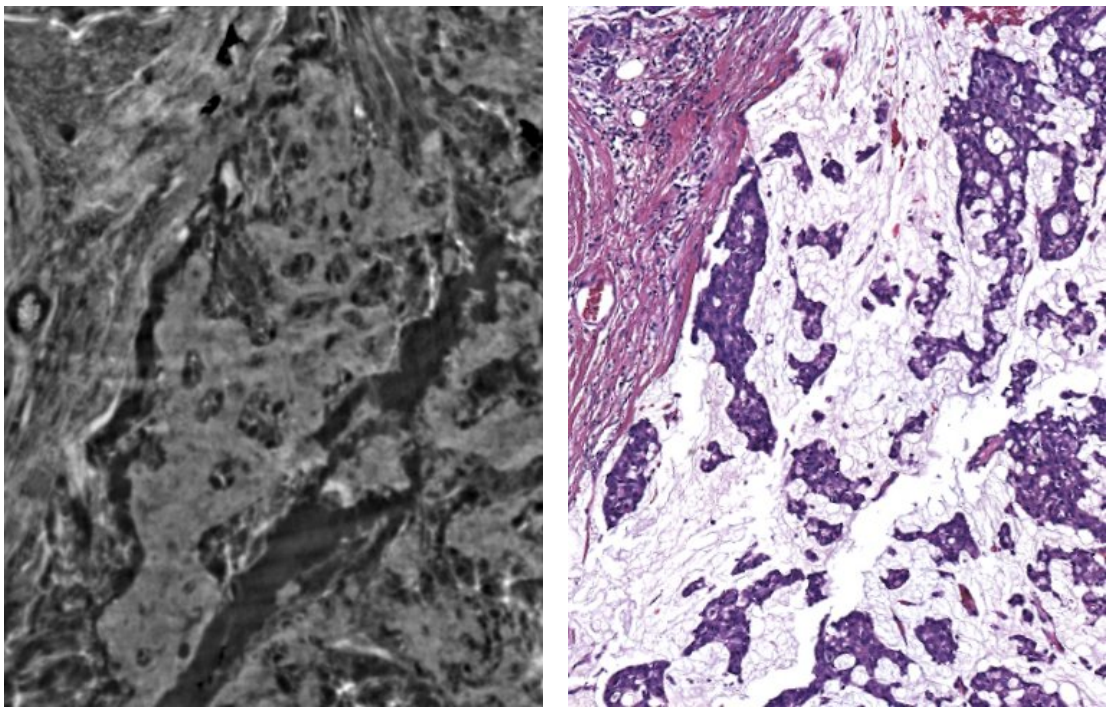

(a) (b)

**Figure 7.6:** Close-up of the area containing mucus. On micro-CT image (a) the mucus is the brightest part while in the histological image (b) is represented by a light pink pattern.

# References

Brun, F., Pacilè, S., Accardo, A., Kourousias, G., Dreossi, D., Mancini, L., Tromba, G., Pugliese, R., 2015. Enhanced and Flexible Software Tools for X-ray Computed Tomography at the Italian Synchrotron Radiation Facility Elettra. Fundamenta Informaticae 141, 233–243. URL: http://content.iospress.com/articles/fundamenta-informaticae/fi1273, doi:10.3233/FI-2015-1273.

Gromoll, B., Salmon, P., 2008. Microcomputed tomography (micro CT): a possibly useful technique in assessment of breast tumor specimens. Anal. Quant. Cytol. Histol. 30, 60–61.

Gufler, H., Franke, F.E., Wagner, S., Rau, W.S., 2011a. Fine Structure of Breast Tissue on Micro Computed Tomography: A Feasibility Study. Academic Radiology 18, 230–234. URL: http://www.sciencedirect.com/science/article/pii/S1076633210005738, doi:10.1016/j.acra.2010.10.006.

Gufler, H., Wagner, S., Franke, F.E., 2011b. The interior structure of breast microcalcifications assessed with micro computed tomography. Acta Radiol 52, 592–596. URL: https://doi.org/10.1258/ar.2011.100489, doi:10.1258/ar.2011.100489.

Keyriläinen, J., Fernández, M., Karjalainen-Lindsberg, M.L., Virkkunen, P., Leidenius, M., von Smitten, K., Sipilä, P., Fiedler, S., Suhonen, H., Suortti, P., Bravin, A., 2008. Toward High-Contrast Breast CT at Low Radiation Dose. Radiology 249, 321–327. URL: http://pubs.rsna.org/doi/abs/10.1148/radiol.2491072129, doi:10.1148/radiol.2491072129.

Limaye, A., 2012. Drishti: a volume exploration and presentation tool, International Society for Optics and Photonics. p. 85060X. URL: https://www.spiedigitallibrary.org/conference-proceedings-of-spie/8506/85060X/Drishti-a-volume-exploration-and-presentation-tool/10.1117/12.935640.short, doi:10.1117/12.935640.

Nishide, H., Kasuga, T., Miyachi, T., 2004. [Report on the 89th Scientific Assembly and Annual Meeting of the Radiological Society of North America–micro-focus x-ray CT imaging of breast specimens with microcalcifications]. Nihon Hoshasen Gijutsu Gakkai Zasshi 60, 1662–1663. URL: http://europepmc.org/abstract/med/15614212, doi:10.6009/jjrt.KJ00003560625.

Paganin, D., Mayo, S.C., Gureyev, T.E., Miller, P.R., Wilkins, S.W., 2002. Simultaneous phase and amplitude extraction from a single defocused image of a homogeneous object. J Microsc 206, 33–40.

Schindelin, J., Arganda-Carreras, I., Frise, E., Kaynig, V., Longair, M., Pietzsch, T., Preibisch, S., Rueden, C., Saalfeld, S., Schmid, B., Tinevez, J.Y., White, D.J., Hartenstein, V., Eliceiri, K., Tomancak, P., Cardona, A., 2012. Fiji: an open-source platform for biological-image analysis. Nat. Methods 9, 676–682. doi:10.1038/nmeth.2019.

Tang, R., Buckley, J.M., Fernandez, L., Coopey, S., Aftreth, O., Michaelson, J., Saksena, M., Lei, L., Specht, M., Gadd, M., Yagi, Y., Rafferty, E., Brachtel, E., Smith, B.L., 2013. Micro-computed tomography (Micro-CT): a novel approach for intraoperative breast cancer specimen imaging. Breast Cancer Res Treat 139, 311–316. URL: https://link.springer.com/article/10.1007/s10549-013-2554-6, doi:10.1007/s10549-013-2554-6.

Willekens, I., Van de Casteele, E., Buls, N., Temmermans, F., Jansen, B., Deklerck, R., de Mey, J., 2014. High-resolution 3d micro-CT imaging of breast microcalcifications: a preliminary analysis. BMC Cancer 14, 9. URL: https://doi.org/10.1186/1471-2407-14-9, doi:10.1186/1471-2407-14-9.

# 8 Conclusions

A twofold objective has guided this thesis work: on the one hand the optimisation of the experimental and processing parameters influencing the image quality on phase-contrast breast tomography and, on the other hand, the validation of the most suitable method to assess image quality in this domain. Original results have been obtained in both these two subjects (a part of them already published in international journals) and interesting aspects for future works have emerged. A third topic, concerning a new interesting application of phase-contrast high-resolution tomography, has been explored and treated in this thesis as well. The main conclusion drawn from this work is that the use of phase contrast and phase retrieval results in significant improvement in the quality of x-ray images of breast tissue with respect to purely absorption images. This has been demonstrated in the low-dose scans by evaluating several different quality indexes and considering the radiological assessment. Low-dose phase-contrast CT images can be obtained with a conventional flat-panel detector having relatively large pixels if large propagation distances are implemented. Overall, summarising the results of the optimisation, it is possible to conclude that the quality of the images obtained with PB-CT method increases when:

1. Large sample-to-detector distances are used (9 $m$)

2. Energies between 32 and 35 $keV$ are used (among the analysed range)

3. Iterative reconstruction algorithms are applied. Best results have been observed for iFBP, MR-FBP and SIRT.

4. The TIE-Hom phase retrieval approach is used with both nominal and half of the nominal value of the $\delta/\beta$

Concerning the best method to assess the image quality:

1. The (objective, no-reference) image quality parameters, $IQ$ and $Q_s$, appear to be in a good agreement with the average (subjective) radiological scores assigned to the images by experienced imaging specialists, particularly for the higher-quality images obtained with half and nominal value of phase retrieval.

2. In particular conditions (i.e. the possibility to define a reference image) some of the proposed full-reference indexes are suited for this kind of study.

This demonstrates that the human interpretation of x-ray images for cancer diagnosis can be linked with quantitative numerical image analysis and it is essential to translate the radiological requirements in terms of image quality, into technological improvements. Moreover the proposed assessment approaches could be used to investigate what "image quality" means, from a quantitative point of view, in other medical fields.

According to these results, the PB-CT method, shows significant promise for breast cancer imaging of live patients. The method is currently best suited for use at specialised synchrotron facilities, such as SYRMEP beamline at Elettra synchrotron, but can potentially be implemented in a clinical environment if sufficiently bright microfocus x-ray sources become available at a practical level. The technique has also been compared with the currently diffused dedicated breast-CT systems. Results indicate that PB-CT can achieve a higher level of image quality with respect to the Koning breast-CT system highlighting important aspects of the image that are fundamental for an accurate diagnosis. This confirms that, the PB-CT technique, could potentially be introduced as a large-scale screening examination

as it could keep a high level of image quality whereby delivering a considerably lower level of mean glandular dose.

A last important use of this technique has been studied: the virtual histology. Since precise geometric locations of ROIs can be derived from the CT data sets of the scanned embedded samples, it is possible to develop computer controlled cutting systems that mechanically achieve the virtually planned sectioning. This would enable the guidance of the cutting process to ROIs, which would render serial cutting unnecessary and would ensure that important structures are not missed. In addition, x-ray based virtual histology can be used to more easily derive geometric and volumetric anatomical measures as compared to classic histology. More importantly, it has been demonstrated that standard procedure introduces major non-uniform deformations within the tissue slices, which makes studies based on CT measures much more reliable. This result can be extended to other kind of specimens and clinical cases that utilise the histology technique. It is possible to conclude that virtual and classic histology complement each other with their respective unique information. For this reason, the introduction of CT-based virtual histology procedure, not only would enable the improvement of histological analysis, but also would offer the potential for automation and thus a dramatic reduction of the workload in clinical routine.

# List of the publications produced in the framework of this Thesis

- P. Baran, S. Mayo, M. McCormack, S. Pacilè, G. Tromba, C. Dullin, F. Zanconati, F. Arfelli, D. Dreossi, J. Fox, Z. Prodanovic, M. Cholewa, H. Quiney, M. Dimmock, Y. Nesterets, D. Thompson, P. Brennan and T. Gureyev "High-resolution X-ray phase-contrast 3D imaging of breast tissue specimens as a possible adjunct to histopathology" *submitted*

- T. Savi, A. Miotto, F. Petruzzellis, A.Losso; S. Pacilè, G. Tromba, S. Mayr, A. Nardini "Drought-induced embolism in stems of sunflower: a comparison of in vivo micro-CT observations and destructive hydraulic measurements". Plant Physiology and Biochemistry, Plant Physiol. Biochem. 2017; 120:24-29

- S. Pacilè, P. Baran, C. Dullin, Y. I. Nesterets, S. C. Mayo, D. Dreossi, D. Thompson, M. McCormack, C. Hall, M. Dimmock, F. Arfelli, F. Zanconati, A. Accardo, T. E. Gureyev and G. Tromba "Parameters affecting image quality in propagation-based phase-contrast breast CT" *submitted*

- S.T. Taba, P. Baran, S. Lewis, R. Heard, S. Pacilè, Y. Nesterets, S. Mayo, C. Dullin, D. Dreossi, F. Arfelli, D. Thompson, M. McCormack, M. Alakhras, F. Brun, M. Pinamonti, C. Nickson, C. Hall, F. Zanconati, D. Lockie, H. Quiney, G. Tromba, T. Gureyev, P. Brennan "Towards improving breast cancer imaging: radiological assessment of propagation-based phase-contrast CT technology" *submitted*

- S. Donato, S. Pacilè, F. Colombo, C. Garrovo, S. Dal Monego, P. Macor, G.Tromba, S.Biffi "Meniscal Ossicles as micro-CT Imaging Biomarker in a

Rodent Model of Antigen-Induced Arthritis: a Synchrotron-Based X-ray Pilot Study". Sci Rep. 2017; 7: 7544.

- P. Baran, S. Pacilè, Y. I. Nesterets, S. C. Mayo, C. Dullin, D. Dreossi, F. Arfelli, D. Thompson, D. Lockie, M. McCormack, S. T. Taba, F. Brun, M. Pinamonti, C. Nickson, C. Hall, M. Dimmock, F. Zanconati, M. Cholewa, H. Quiney, P. C. Brennan, G. Tromba, T. E. Gureyev "Optimization of in-line X-ray phase-contrast tomographic imaging for breast cancer screening". Phys. Med. Biol. 62, 2315?2332 (2017)

- A. Nardini, T. Savi, A. Losso, G. Petit, S. Pacilè, G. Tromba, S. Mayr, P. TrifilA. Lo Gullo, S. Salleo. "X-ray micro-tomography observations of xylem embolism in stems of Laurus nobilis L. are consistent with hydraulic measurements of percentage loss of conductance". New Phytol 213 (3), 1068-1075 (2016).

- G. Tromba, S. Pacilè, Y.I. Nesterets, F. Brun, C. Dullin, D. Dreossi, T.E. Gureyev, (2016). "Phase-contrast clinical breast CT: Optimization of imaging setups and reconstruction workflows". 13th International Workshop on Breast Imaging, IWDM 2016; Malmo; Sweden June 2016.

- S. Pacilè, S. Biffi, R. H. Menk, C. Garrovo, S. Dal Monego, F. Arfelli, L. Rigon, F. Colombo, P. Macor, A. Accardo, and G. Tromba, XIV Mediterranean Conference on Medical and Biological Engineering and Computing 2016: MEDICON 2016, March 31st-April 2nd 2016, Paphos, Cyprus (Springer International Publishing, Cham, 2016), chap. Alterations in Trabecular Bone m-Architecture and Cartilages in Rats with Antigen-Induced Arthritis (AIA) Resulting from Synchrotron-Based X-Ray Imaging Analysis, pp. 409-413.

- F. Brun, S. Pacilè, A. Accardo, L. Mancini, D. Dreossi, G. Tromba, G. Kourousias, and R. Pugliese, "Enhanced and flexible software tools for X-ray tomography experiments at the Italian synchrotron radiation facility Elettra", Fundamenta Informaticae 141(2-3):233-243 (2015).

- S. Pacilè, F. Brun, C. Dullin, Y.I. Nesterest, D. Dreossi, S.Mohammadi, M. Tonutti, F. Stacul, D. Lockie, F. Zanconati, A.Accardo, G. Tromba and T.E. Gureyev, "Clinical application of low-dose phase contrast breast CT: methods for the optimization of the reconstruction workflow", Biomed. Opt. Express 6, 3099-3112 (2015)